Analysis of historical polarisation data of Venus

And its application to exoplanets

Lisanne Rosalia Maria Hendriks

April 2020
Spaceflight, Space Exploration

Supervisor: Dr. D. M. Stam
External supervisor: Dr. L. Rossi

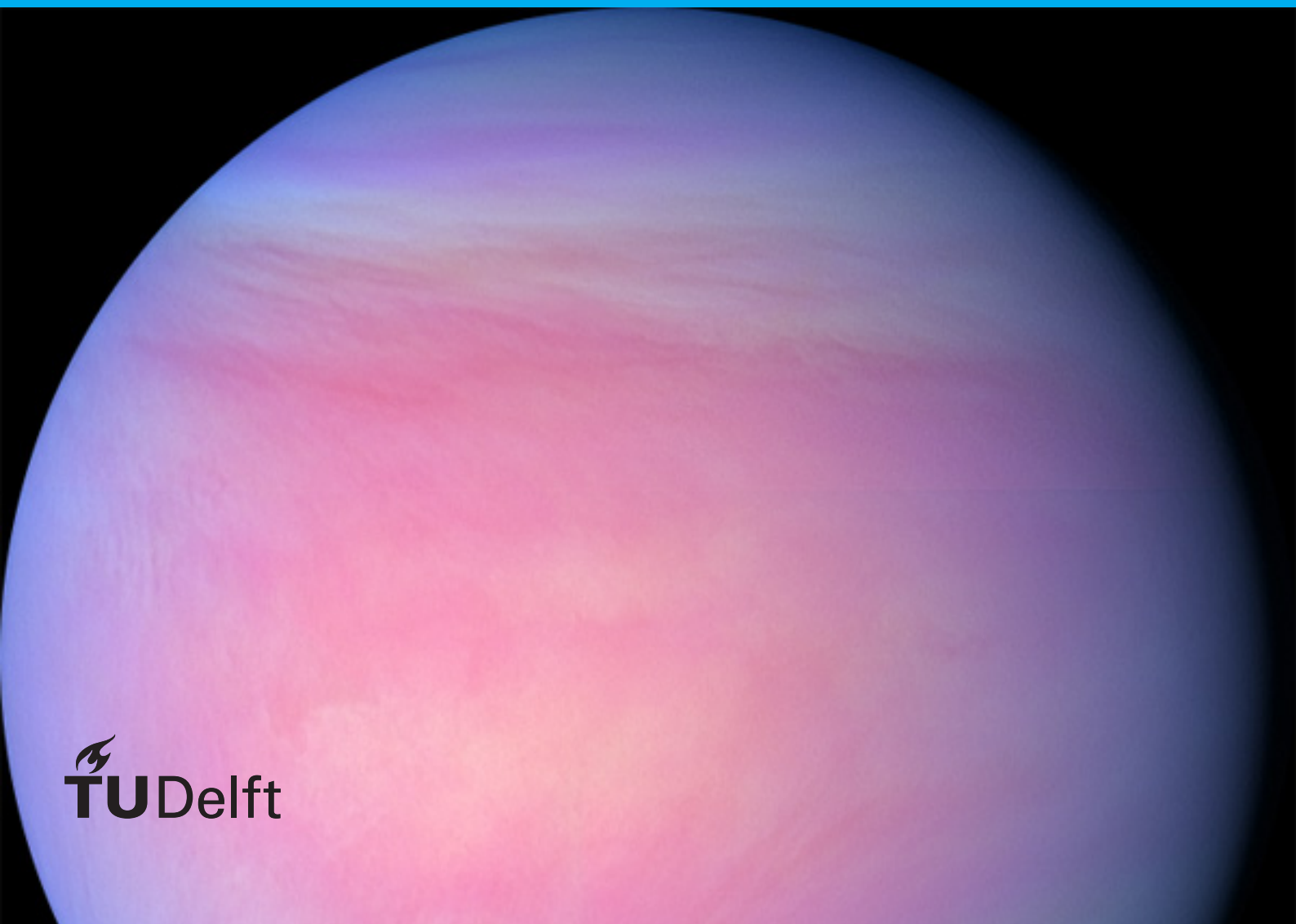

TU Delft

Analysis of historical polarisation data of Venus

And its application to exoplanets

by

Lisanne Rosalia Maria Hendriks

to obtain the degree of Master of Science
at the Delft University of Technology
to be defended publicly on 24 April 2020.

Student number: 4320395

Thesis committee:	Dr. D. M. Stam,	TU Delft, supervisor
	Dr. L. Rossi,	LATMOS, external-supervisor
	Prof. dr. L. L. A. Vermeersen,	TU Delft
	Dr. A. Menicucci,	TU Delft

An electronic version of this thesis is available at http://repository.tudelft.nl/.

Source of picture on cover: [10]

TU Delft

Preface

My student life has almost come to an end with finishing this report. It has been a crazy ride: from Maritime Technology to, eventually, polarization of the Venus atmosphere. When coming to Delft in 2013, I never thought that my thesis report would be titled: *Analysis of historical polarisation data of Venus*. Before we continue with this thesis work, I would like to take this opportunity to thank the people who have made this possible.

First of all I want to thank my supervisor Dr. Daphne Stam for all the patience and effort she put in supervising me. She really guided me through the thesis process with her scientific knowledge and enthusiasm during our weekly meetings. I also want to thank her for the interesting lectures she gave in planetary sciences which pushed me into finding a thesis topic in this field.

I want to thank Dr. Loïc Rossi for his external supervision from French. He came up with the research idea on which my thesis is based, so without his help, no report would have laid in your hands today. He also really helped me with getting to know PyMieDAP.

I also want to thank the other members of the thesis committee, Prof. dr. L. L. A. Vermeersen and Dr. A. Menicucci, for taking the time to read my report and attending my presentation and defence.

Finally, I wish to thank my family and friends for all their support. In particular my parents and sister for their emotional support, they were always there when I needed them. I also want to thank my boyfriend for his patience in listening to my thesis ideas.

Lisanne Rosalia Maria Hendriks
Delft, March 2020

Abstract

Aims: Analysing historical disk-integrated polarisation data of Venus with the help of numerical simulations to learn about the time variability in cloud and haze properties, the position of the UV-absorber and the polar cap regions.
Method: With numerical simulations, polarization curves will be calculated for specific input conditions. We compare numerically computed polarization curves to the historical polarization data to derive the microphysical properties of Venus's cloud and haze particles. For the numerical simulations we use PyMieDAP (Python Mie Doubling-Adding Program). This is a Python module around FORTRAN routines to perform the radiative transfer computations.
Results: From our research we obtain values for the imaginary part of the refractive index of the cloud particles of the order 10^{-4}. It is most likely that the absorber is mainly located at the equator or in patchy clouds covering 80% of the planet. It is found that in the presence of precise disk-integrated polarization data, it is possible to detect variations in the polar region for: optical thickness of the haze and cloud, effective radius of the cloud and haze particles, the refractive index of the cloud particles and the cloud top pressure. For Venus we found that it is likely that there exist larger particles at higher altitudes at the Venus poles. Unfortunately, it is very hard to say something about the long term variations on the planet. The historical data is not suitable for a detailed time variability analysis. This is due to the fact that the data is not nicely spread over the time. For the Venus case, it can be roughly stated that: the polarization was higher in 1975/1976 than in 1965/1968; the polarization was also higher in 1968/1970 than 1965/1968 but not higher than in 1976; there was a decrease in the polarization of the ultraviolet region in the years 1964/1965.
Conclusions: Future observations should be made in a broad range of wavelengths, at as many phase angles as possible and in time frames similar to the orbital period of the (exo)planet. Since Venus can be observed as if it were an exoplanet (broad range of observable phase angles and disk-integrated data), we applied this research to exoplanets as well. We concluded with the help of the Venus data and simple models that it is possible to obtain cloud properties, such as the refractive index and the optical thickness of the cloud, of exoplanets using polarization observations. It was found that those properties are harder to distinguish using flux measurements since the geometric albedo and the distance to the planet are unknown.

Nomenclature

Abbreviations

CoRoT	Convection, Rotation and planetary Transits
OCPP	Orbiter Cloud Photopolarimeter
OCR	Optical Character Recognition
PLATO	PLAnetary Transits and Oscillations of stars
PyMieDAP	Python Mie Doubling-Adding Program
ssc	subsolar cloud
ssh	subsolar haze
TESS	Transiting Exoplanet Survey Satellite
UV	Ultraviolet

Greek symbols

α	phase angle [°]
Θ	scattering angle [°]
λ	wavelength [μm]
ρ	depolarization factor
σ_a	scattering cross section [$\mu m^2\ molecule^{-1}$]
σ^m	molecular extinction cross-section [$\mu m^2\ molecule^{-1}$]
σ_c	extent of subsolar cloud [°]
τ	opticall thickness

Other

b^m	extinction optical thickness
CO_2	carbon dioxide
F	total flux
g	acceleration of gravity [m s^{-2}]
H_2O	water
H_2SO_4	sulfuric acid
m	mass per mole [atomic mass units]
N	column number density [$molecule\ \mu m^{-2}$]
N_a	constant of Avogadro
n_i	imaginary part of the refractive index
n_r	real part of the refractive index
P	degree of polarization [%]
p	pressure [bars]
Q	lineairly polarized flux
r_{eff}	effective radius [μm]
U	lineairly polarized flux [W m^{-2} m^{-1}]
V	circularly polarized flux [W m^{-2} m^{-1}]
v_{eff}	effective variance [W m^{-2} m^{-1}]

Contents

1 Introduction

In this report historical polarisation data of Venus will be analysed. To do this, use is made of disk-integrated polarization data covering the periods 1922-1924, 1950, 1953, 1959-1969 and 1975-1979. This chapter will first give a short description of the problem, followed by the research objective and an overview of the structure of the report.

1.1. Problem description

Venus is the planet that is closest to Earth and is comparable in size and mass, but Venus evolved completely different [6]. The Venus atmosphere, which is mostly composed of carbon dioxide (CO_2) gas (96% - 97%) with traces of nitrogen (3.5%), has a surface pressure ($\sim 90 bar$) and a surface temperature ($\sim 737 K$) much higher than Earth [8]. Venus spins in opposite direction compared to most planets: it spins in retrograde direction. Thereby, Venus spins much slower than Earth: it takes Venus 243 Earth days to complete one rotation around its own axis. The time Venus takes to orbit the Sun (a Venus year) is shorter, namely 225 Earth days [6]. At first sight Venus looks like a homogeneous sphere covered in stable clouds but when looking longer, one can observe a very active cloud cover: the clouds rotate fast and show remarkable patterns. The reason for the dynamic clouds is not yet known: Venus's axial tilt is only 3 degrees [6] so Venus does not really experience seasons. There are indications for active vulcanism on Venus which could influence the cloud composition. In the 1960's, there was a lot of scientific interest in Venus, the USSR alone already sent out 18 probes towards Venus in the period 1960-1970. In order to learn something about the atmosphere, intensity and polarization measurements were done, first from the Earth's surface en later from space. Those measurements show small variations which might be due to measurement errors but they can also be due to changes in the clouds and/or hazes. The Venus Express mission has significantly extended our knowledge on the Venus atmosphere. This leads to the purpose of this research: the (re)analyses of the historical polarization data of Venus. This analysis can lead to better insight in the early cloud top altitude and haze thickness of Venus.

Our research not only aims to give new information about Venus itself but will also be applied to exoplanets. Venus is suitabel for this since we analysed disk-integrated data: exoplanet observations will also be disk-integrated. And for Venus and exoplanets it is possible to observe in different phase angles. Due to missions such as Kepler and CoRoT (Convection, Rotation, and planetary Transits) which detected exoplanets with the transit method, the existence of thousands of exoplanets has been confirmed. With current missions such as TESS (the Transiting Exoplanet Survey Satellite) and future missions such as PLATO (PLAnetary Transits and Oscillations of stars), this number will only increase. With the rising interest in exoplanets, the next step in exoplanet research is investigating the composition of the atmospheres of these planets. One way to characterize the exoplanet is with

the help of polarization [11]. Nowadays there aren't many telescopes that measure polarization but the LUVOIR concept telescope will have the Pollux instrument which can measure circular and linear polarization in the ultraviolet spectral region [7]. The results of the (re)analysis of the historical data will be interesting for polarization research on exoplanets because they can serve as a model: the variation measured on Venus can give us insight in what to expect for similar measurements of exoplanets.

1.2. Research objective

In order to perform the analysis of historical polarization data described above, some research questions and the research objective are formulated.

The research objective is to (re)analyse the old ground based polarization data of Venus by using the current knowledge of the Venus atmosphere and numerical simulations.

In order to fulfill this research objective, some questions need to be answered.

1. What polarization measurements of Venus were done in the past and what can we learn from them?
2. What can we say about the long term variations in the historical polarization measurements by combining them?
3. Is it possible to recognize the horizontal inhomogeneity in the historical ground based data?
4. How can we apply the outcomes to exoplanet research?

1.3. Report structure

To fulfill the research objective described before, the main results of the research are written in paper format. The used format is the *Astronomy & Astrophysics* (A & A) paper template. This paper can be found in Chapter 2 and is built up in the following way: it starts with discussing the definitions used for flux and polarization, then the historical data will be discussed and analysed, followed by a description of the method, the results, and the paper will be concluded with a discussion and finally the recommendations. Chapter 3 of this report gives a short review of the research questions and Chapter 4 contains the verification of the use of PyMieDAP.

2

Paper

In this chapter the paper, which contains the main content of the research, can be found.

manuscript no. output
April 10, 2020
©ESO 2020

Analysis of historical polarisation data of Venus

And its application to exoplanets

L.R.M. Hendriks

Delft University of Technology, Klyverweg 1, 2629 HS Delft, the Netherlands

April 10, 2020

ABSTRACT

Aims. Analysing historical disk-integrated polarisation data of Venus with the help of numerical simulations to learn about the time variability in cloud and haze properties, the position of the UV-absorber and the polar cap regions.

Methods. With numerical simulations, polarization curves will be calculated for specific input conditions. We compare numerically computed polarization curves to the historical polarization data to derive the microphysical properties of Venus's cloud and haze particles. For the numerical simulations we use PyMieDAP (Python Mie Doubling-Adding Program). This is a Python module around FORTRAN routines to perform the radiative transfer computations.

Results. From our research we obtain values for the imaginary part of the refractive index of the cloud particles of the order 10^{-4}. It is most likely that the absorber is mainly located at the equator or in patchy clouds covering 80% of the planet. It is found that in the presence of precise disk-integrated polarization data, it is possible to detect variations in the polar region for: optical thickness of the haze and cloud, effective radius of the cloud and haze particles, the refractive index of the cloud particles and the cloud top pressure. For Venus we found that it is likely that there exist larger particles at higher altitudes at the Venus poles. Unfortunately, it is very hard to say something about the long term variations on the planet. The historical data is not suitable for a detailed time variability analysis. This is due to the fact that the data is not nicely spread over the time. For the Venus case, it can be roughly stated that: the polarization was higher in 1975/1976 than in 1965/1968; the polarization was also higher in 1968/1970 than 1965/1968 but not higher than in 1976; there was a decrease in the polarization of the ultraviolet region in the years 1964/1965.

Conclusions. Future observations should be made in a broad range of wavelengths, at as many phase angles as possible and in time frames similar to the orbital period of the (exo)planet. Since Venus can be observed as if it were an exoplanet (broad range of observable phase angles and disk-integrated data), we applied this research to exoplanets as well. We concluded with the

help of the Venus data and simple models that it is possible to obtain cloud properties, such as the refractive index and the optical thickness of the cloud, of exoplanets using polarization observations. It was found that those properties are harder to distinguish using flux measurements since the geometric albedo and the distance to the planet are unknown.

Key words. Venus atmosphere, disk-integrated polarization, flux, PyMieDAP, exoplanets

1. Introduction

Venus is the planet that is closest to Earth and comparable in size and mass, but it evolved completely differently (NASA 2018). Venus, which atmosphere is mostly composed of carbon dioxide (CO_2) gas (96% - 97%) with traces of nitrogen (3.5%), has a surface pressure ($\sim 90bar$) and a surface temperature ($\sim 737K$) much higher than Earth (Pätzold et al. 2007). Venus spins in opposite direction compared to most planets: it spins in retrograde direction. Thereby, Venus spins much slower than Earth. It takes Venus 243 Earth days to complete one rotation around its own axis. The time Venus takes to orbit the Sun (a Venus year) is shorter, namely 225 Earth days (NASA 2018). At first sight, Venus looks like a homogeneous sphere covered in stable clouds but when looking longer, one can observe a very active cloud cover: the clouds rotate fast and show remarkable patterns. The origin of the cloud activity is still unknown; Venus's axial tilt is only 3 degrees (NASA 2018) so Venus does not really experience seasons. There are indications for active vulcanism on Venus, which can contribute to the cloud activity. The first indications of the composition of the Venus clouds came from ground based observations: polarimetric observations. Ground based polarimetric observations will be (re)analysed in this paper. With the analysis of the polarization data it might be possible to map some of the cloud changes that happened since the 1900's.

In this paper, historical polarization measurements of Venus will be investigated. These historical polarization measurements comprise the data reported in the papers published by Lyot (1929), Coffeen & Gehrels (1969), Dollfus & Coffeen (1970) and Gehrels et al. (1979). Venus can be observed in a broad phase angle range (such as most exoplanets). The phase angle is the angle between the observer (Earth), the observed planet (Venus) and the Sun. This is illustrated in Figure 1, the phase angle is indicated with α.

The cloud structure of Venus is very complex and consists of multiple layers: the lower cloud; the middle cloud; the upper cloud and the upper haze, all combined ranging from altitudes of 47.5 km to 90 km (Titov et al. 2018). By analysing Earth-based disk integrated polarization measurements, Hansen & Hovenier (1974) found particle properties that are still considered reliable today: a spherical particle shape, particle effective radius of $r_{eff} = 1.05\mu m \pm 0.1\mu m$, effective variance of $v_{eff} = 0.07 \pm 0.02$ and a pressure at the cloud tops of $50mb \pm 25mb$. They also obtained refractive indices (n_r) of the cloud particles in the $\lambda = 0.34\mu m$ to $\lambda = 0.99\mu m$ region. Based on this data, they characterized the particles as sulphuric acid solution particles. This composition was later confirmed by the Vega probes that sampled the atmosphere through aerosol collecting filters (Titov et al. 2018).

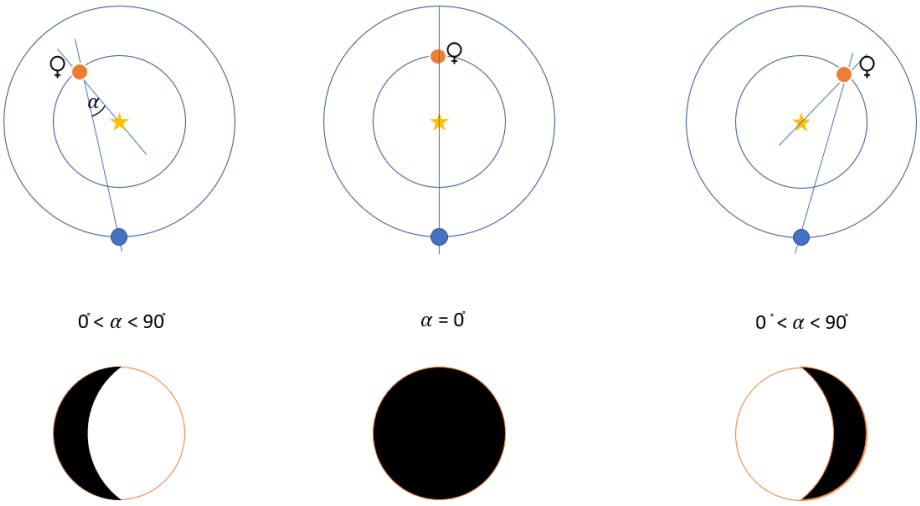

Fig. 1: *Top*:Representation of planet position for small phase angles, α. The yellow star represents the Sun, the Earth and Venus are represented by the blue and orange circles respectively. *Bottom*: Part of the planet that contributes to the polarization (white).

Hansen & Hovenier (1974) weren't able to distinguish the haze layer. But they already noted the possibility of the presence of different particle properties at the polar caps (here polar caps refer to the atmosphere on top and around the poles) since they observed that the influence of the polarization of the polar regions was small compared to the polarization of the disk as a whole. Some years later this was confirmed by Kawabata. Kawabata (1981) looked at polarization by planets with polar cap features; he numerically simulated polar caps that mapped different percentages of the planet's surface for the Venus case. He found that models with polar caps gave a better fit to the data, and he found that there should be a cloud structure transition at about 50° latitude. In that same period Kawabata et al. (1980) compared ground based measurements with OCPP (Orbiter Cloud Photopolarimeter) measurements from the Pioneer Venus orbiter. They saw that the data sets started to deviate for phase angles of 30° and larger for $\lambda = 0.935\mu m$. The OCPP observations showed less negative polarization curves than what you would expect for H_2SO_4 particles with effective radii of $1.05\mu m$ and less negative polarization curves than the ground based observation by Coffeen & Gehrels (1969); Dollfus & Coffeen (1970); Gehrels et al. (1979). This difference was explained by a layer of haze/submicron sized particles above the main cloud. Kawabata et al. (1980) obtained the following properties for the haze particles: $r_{eff} = 0.23 \pm 0.04\mu m$, $v_{eff} = 0.18 \pm 0.1$ and $n_r = 1.45 \pm 0.04$ (in the $0.365\mu m$ - $0.55\mu m$ range). This haze layer on top of the clouds was also observed by the polarization measurements by the Mariner 10 (Knollenberg et al. 1980).

In all the research described above the imaginary part of the refractive index of the cloud and haze particles was assumed to be zero. The imaginary part of the refractive index is used to describe the absorption. For sulphuric acid solutions this imaginary part of the refractive index is not equal to zero but it is very small: order of 10^{-8} for $\lambda = 0.340\mu m$ (Palmer & Williams 1975). Later research showed that it is likely that the imaginary part of the refractive index is larger than this 10^{-8} in the

ultraviolet spectral region (Pollack et al. 1980; Pérez-Hoyos et al. 2018; Marcq et al. 2020). This is called the UV absorber. Marcq et al. (2020) suggested that there might be more than one source for the UV absorption. Marcq et al. (2020) found values of 10^{-3} for the imaginary part of the refractive index for the so-called mode 2 particles (particles with effective radii of $1.05\mu m$ and a sulfuric acid concentration of 75% (Rossi 2016)) and values between 10^{-2}-10^{-1} for the imaginary part of the refractive index of the so-called mode 1 particles (particles with effective radii of $0.25\mu m$ that consist of sulfuric acid with various concentrations (Rossi 2016)). But the exact nature of the UV absorber(s) is still unknown. It is also still unknown if this UV absorber is variable over time such as other Venus cloud features.

In this paper, we present a (re)analysis of ground based polarimetry data using a sensitivity analysis of the most important atmospheric properties (refractive index of the cloud and haze particles, and the optical thickness of the clouds and hazes); an investigation to the possibility to detect time variable changes in the atmosphere of Venus; an analysis of the location of the UV absorber; an analysis of the effect of applying different polar models; and finally a comparison of polarization with flux measurements.

Our research not only aims to give new information about Venus itself but will also be applied to exoplanets. Venus is suitabel for this since we analysed disk-integrated data: exoplanet observations will also be disk-integrated. And for Venus and exoplanets it is possible to observe in different phase angles. Due to missions such as Kepler and CoRoT (Convection, Rotation, and planetary Transits) the existence of thousands of exoplanets has been confirmed. With current missions such as TESS (the Transiting Exoplanet Survey Satellite) and future missions such as PLATO (PLAnetary Transits and Oscillations of stars), this number will only increase. With the rising interest in exoplanets, the next step is investigating the composition of the atmospheres of these planets. One way to characterize the exoplanet is with the help of polarization (Wiktorowicz & Stam 2015). Nowadays there aren't many telescopes that measure polarization but the LUVOIR concept telescope will have the Pollux instrument which can measure circular and linear polarization in the ultraviolet spectral region (NASA 2019). Venus can be observed as if it were an exoplanet (disk-integrated and over multiple phase angles) to investigate the possibilities for missions containing polarimeters.

The paper is structured in the following way: Section 2 discusses the definitions used for flux and polarization, Sections 3 and 4 summarize and analyze the historical data. Section 5 discusses the method and software used for this research. The results are discussed in Section 6. Section 7 applies this work to exoplanets. Finally, Sections 8 and 9 contain the discussion and recommendations, respectively.

2. Definitions

Light is a transverse, electromagnetic wave. Natural light such as that of the Sun is unpolarized. This unpolarized light can, however, become polarized by scattering and reflection. Light can be

linearly polarized and/or circularly polarized. When light is linearly polarized the wave oscillates in a given plane. For circularly polarized light, the direction of oscillation of the electric field is not in one direction but it rotates in clockwise or counter-clockwise direction (Beeson & Mayer 2008). The total flux of a lightbeam can, in general, be written as (Hansen & Travis 1974):

$$\mathbf{F} = \mathbf{F_{unpol}} + \mathbf{F_{pol}} \tag{1}$$

The polarized part can be further separated into a linearly polarization part, $\mathbf{F_{lp}}$, and a circularly polarization part, $\mathbf{F_{cp}}$ (Hansen & Travis 1974).

$$\mathbf{F_{pol}} = (\mathbf{F_{lp}}^2 + \mathbf{F_{cp}}^2)^{1/2} \tag{2}$$

The light that is reflected by a planet can be represented by the following flux column vector (Stam 2008):

$$\mathbf{F} = \begin{bmatrix} F \\ Q \\ U \\ V \end{bmatrix} \tag{3}$$

with F the total flux, Q and U the linearly polarized fluxes and V the circularly polarized flux.

The degree of polarization is defined as (Stam 2008):

$$P = \frac{\sqrt{Q^2 + U^2 + V^2}}{F} \tag{4}$$

Assuming that the incoming sunlight or starlight is unpolarized and the planet is mirror-symmetric with respect to the scattering plane, U and V will be zero when integrated over the planetary disk. This scattering plane is the plane through the centers of the star, planet and observer (Stam et al. 2004). So in this case the plane through the centers of the Sun, Venus and Earth. The scattering plane will be used as the default reference plane for the local reflections and disk integrated reflected light. If U and V equal zero, we can use the following definition for the degree of polarization:

$$P = \frac{-Q}{F} \tag{5}$$

Meaning that P is positive for $Q < 0$, this indicates perpendicular polarization with respect to the reference plane. And P is negative for $Q > 0$, which means that the light is polarized parallel to the reference plane.

F and Q depend on the properties of the planet and the phase angle and they both are functions of the planetary radius (r), observer distance (d) and the stellar flux that arrives at the planet (πF_0) (Stam 2008). Equation 5 learns us that the degree of polarization is independent of radius, distance

and stellar flux since they cancel out due to the division. The independence of stellar flux is very convenient for the Venus data since it has been obtained over several years, meaning no correction is needed for the possible varying stellar flux and location of Venus. The independence on planetary radius and distance is a nice property of polarization when it comes to exoplanets. For interpreting polarization data we do not need to know the distance to the exoplanet or the radius of the exoplanet, which are, in the case of exoplanets, often unknown or determined with large uncertainties.

3. The historical data

In this section, the historical data that are used for this research will be described. All used data are Earth ground-based measurements taken over several years, covering a wide range of different phase angles. Almost the whole phase angle range from 0° to 180° is present in the measurements. It is not possible to measure exactly at phase angle 0° because there Venus is blocked by the Sun, see Figure 1. For $\alpha = 180°$ Venus stands right between the Sun and the Earth and therefore no by Venus reflected sunlight can be observed from Earth. The time frames for which data is available are: 1922-1924,1950,1953, 1959-1969 and 1975-1979. The used datasets will be described in this section.

The measurements were originally only available on paper in table form and were digitized by Dr. Loïc Rossi with the help of optical character recognition software (OCR). I checked this digitization and made corrections where necessary. These were small corrections where the OCR software for example "recognized" a 3 instead of a 8. In total, not more than 50 corrections were made on a total of 1419 datapoints and around 200 datapoints (from the original of ~1619) were removed since they were included twice. Therefore we assume that the error on the digitization of the data is very small.

3.1. Lyot (1929)

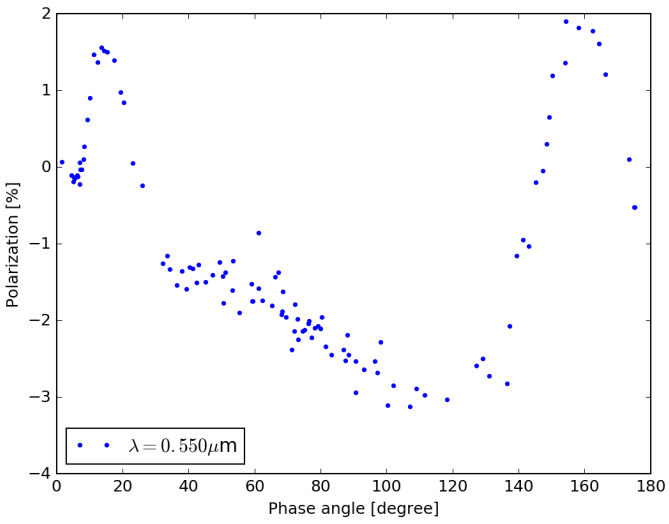

Fig. 2: Data set obtained by Lyot between 1922 and 1924.

Ninety years ago, Lyot (1929) wrote his PhD thesis on the polarization of light from planets, some terrestrial surface materials and water droplets. He also measured the disk-integrated polarization of Venus, the observations are shown in Figure 2. Lyot used the Angle of Vision which is nowadays known as the phase angle, α. He found that the polarization of Venus is very different from the polarization of the Moon, Mercury and Mars. Lyot (1929) noted that the average plane of polarization of Venus was either parallel or perpendicular to the plane of scattering (earlier defined as the reference plane). He found that the sign of the polarization of Venus changed four times: at α = 7°, 24°, 147° and 173°, see Figure 2. It is assumed that Lyot measured at wavelengths of 0.550μm (Dollfus & Coffeen 1970). The data by Lyot was obtained over a three year period: from May 1922 till July 1924. The mean deviation on this data is of the order of 0.01% in absolute polarization (Lyot 1929).

3.2. Coffeen-Gehrels (1969)

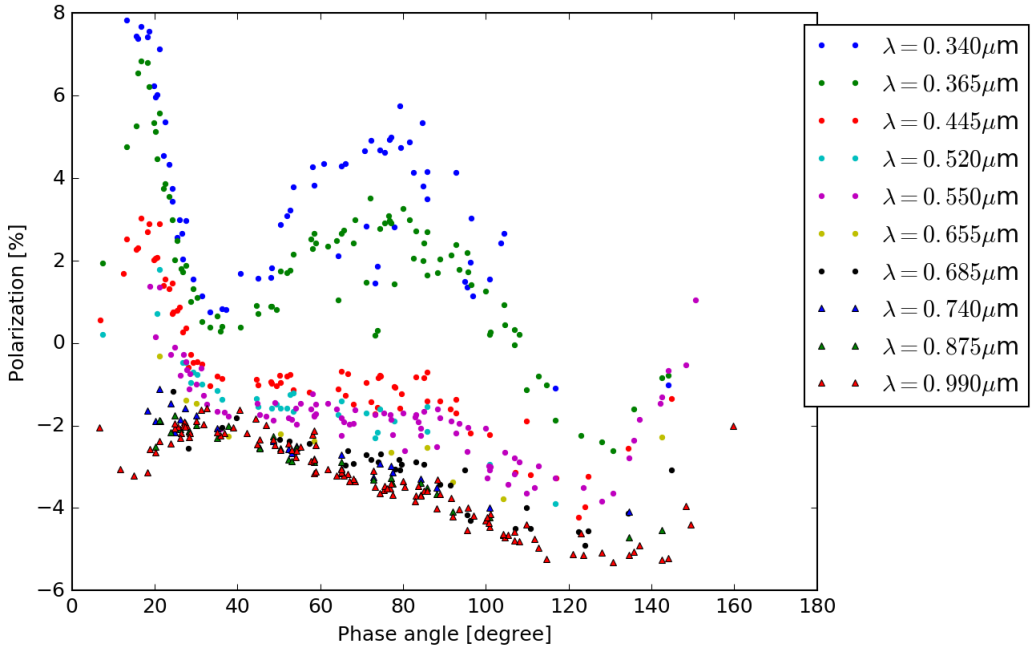

Fig. 3: Data set obtained by Coffeen and Gehrels between 1959 and 1968.

In the period between April 1959 and January 1968 measurements of the linear polarization of sunlight reflected by Venus were made by Coffeen & Gehrels (1969) and published in 1969. This was done in nine bandwidth filters: 0.340μm, 0.365μm, 0.445μm, 0.520μm, 0.550μm, 0.655μm, 0.685μm, 0.740μm, 0.875μm, 0.990μm, covering a phase angle range from 7° to 160°. The data is displayed in Figure 3. The probable error on the data varies from 0.0% polarization to 0.20% polarization. From the data, Coffeen & Gehrels (1969) could conclude that the position angle of disk polarization is either perpendicular or parallel to the plane of scattering. This was also observed by Lyot (1929). Since repeatability was observed over their almost 10 years observational period, Coffeen & Gehrels (1969) concluded that the light scattering mechanism on Venus must be rather stable. The polarization wavelength dependence was found to be generally monotonic: the

positive polarization increases with decreasing wavelength. At the longer wavelengths, the negative polarization is dominant. This is impossible for molecular scattering but it is characteristic for scattering by transparent particles (Coffeen & Gehrels 1969). Polarization diagrams show a peak in the polarization near 15° phase angle, this is called the 'rainbow', which is caused by reflection within transparent spheres. The fact that the polarization position angle was either parallel or perpendicular to the plane of scattering could be explained only with the assumptions that no particle alignment mechanisms exist in the atmosphere of Venus, and that brightness and polarization are symmetrical about the illumination equator (Coffeen & Gehrels 1969). Which means that the planet introduces no preferential direction, leaving only the incident and emergent rays to define the direction of polarization (assuming unpolarized incident radiation) (Coffeen & Gehrels 1969).

3.3. Dollfus-Coffeen (1970)

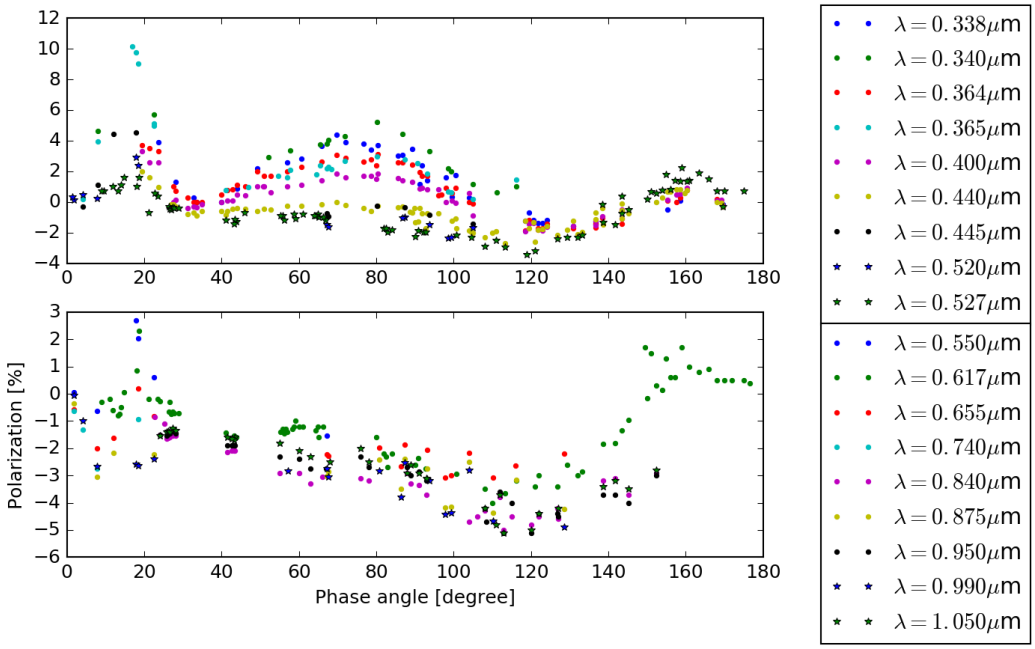

Fig. 4: Data set obtained by Dollfus and Coffeen between 1950 and 1970.

The paper by Dollfus & Coffeen (1970) compares two kinds of measurements: measurements made in France by Dollfus, Focas and Marin and measurements made in the US by Coffeen, Gehrels and Veverka. The US observations are the ones presented by Coffeen & Gehrels (1969), but the 1970 paper adds some new measurements from 1967 and January 1970. Dollfus & Coffeen (1970) found that the agreement of the independent measurements is generally better than ±0.3% polarization. Combining these observations, a period from September 1950 till January 1970 is covered in the wavelength region of $\lambda = 0.338\mu m$ to $\lambda = 0.990\mu m$. The observations cover the phase angle range from 1.5° to 176.5°. The data is displayed in Figure 4. For the French measurements, use was made of three different polarimeters: a photoelectric ultraviolet polarimeter, a visual fringe polarimeter and a photoelectric infrared polarimeter.

Interestingly, the polarization of the disk was very low from late 1964 through 1965 in the ultraviolet spectral range. No evidence was found for a systematic error; the basic instrumentation did not change during the observations. So the conclusion is that the global ultraviolet polarization was generally lowered for approximately 18 months (Dollfus & Coffeen 1970).

3.4. Gehrels (1979)

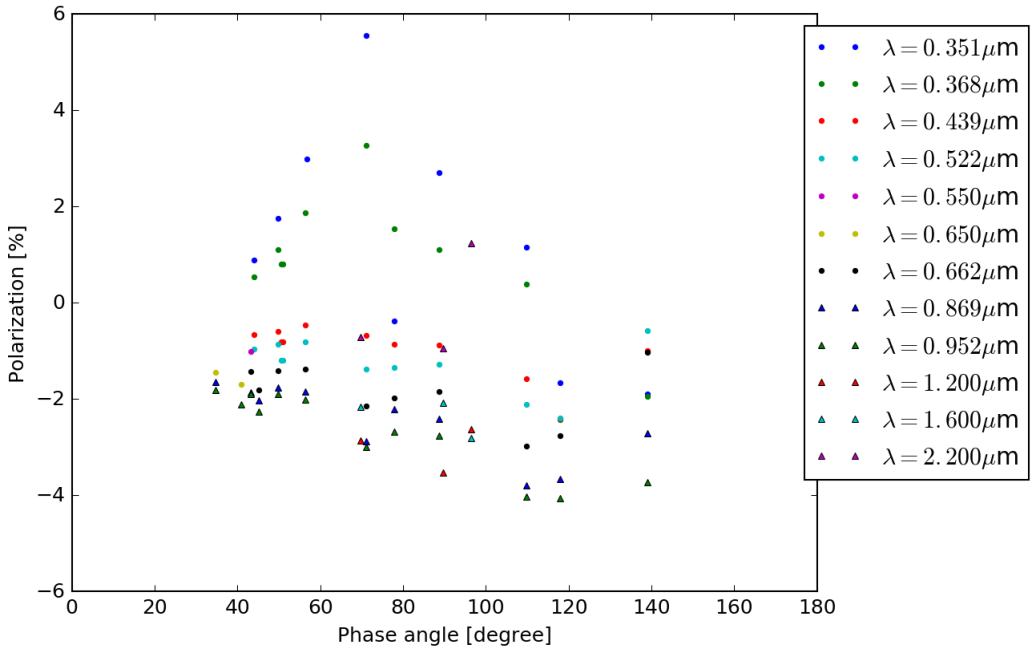

Fig. 5: Data set obtained by Gehrels between 1975 and 1977.

In the paper by Gehrels et al. (1979) four sets of linear polarization data on Venus are discussed. Two of the data sets only include small regional observations which are spread over the visible parts of Venus. Since this data is not disk-integrated, it will not be discussed here. With the Catalina 154-cm telescope and the MINIPOL polarimeter, the Venus disk was observed in the period February 1975 till February 1977. The used wavelengths were: 0.351μm, 0.368μm, 0.439μm, 0.522μm, 0.550μm, 0.650μm, 0.662μm, 0.869μm and 0.952μm. The error on the data is between 0.01% and 0.11% polarization. The fourth set of observations contains observations in the infrared but this data set is too small to take into consideration for this analysis: for each of the wavelengths (1.2μm, 1.6μm and 2.2μm), only three measurements are available.

Since the error is not known for every single measurement and the errors are relatively small (order of 0.01%-0.1%), the error bars for none of the datasets will be displayed in the figures.

4. Analysis of the historical data

The data described in the previous section has been combined and sorted by wavelength, this is listed in Table 1. Since set 1, 2, 4, 5, 8, 12, 13 and 14 will be discussed in more depth, they are

displayed in Figures 6, 7, 8, 9, 10, 11, 12 and 13. The assumption that the cloud particles are solutions of sulfuric acid gives a starting point for the spectral analysis. If the refractive indices for two (or three) wavelengths are the same, we have combined them. The assumed refractive indices are based on the values found by Hansen & Hovenier (1974) (see Figure 14 in Hansen & Hovenier (1974)) and the values published by Palmer & Williams (1975). As mentioned before, the infrared wavelengths are excluded from this research because there are only 3 observations per wavelength. The lack of observations is also the reason that $\lambda = 0.351\mu m$, $0.368\mu m$ and $0.662\mu m$ with respectively 9, 11 and 10 observations are excluded.

Set	Wavelength[μm]	Measurement set
1	0.338	Dollfus and Coffeen (1970), French
1	**0.340**	Coffeen and Gehrels (1969)
1	0.340	Dollfus and Coffeen (1970), US
2	0.364	Dollfus and Coffeen (1970), French
2	**0.365**	Coffeen and Gehrels (1969)
2	0.365	Dollfus and Coffeen (1970), US
3	**0.400**	Dollfus and Coffeen (1970), French
4	0.439	Gehrels (1979)
4	0.440	Dollfus and Coffeen (1970), French
4	**0.445**	Coffeen and Gehrels (1969)
4	0.445	Dollfus and Coffeen (1970), US
5	**0.520**	Coffeen and Gehrels (1969)
5	0.520	Dollfus and Coffeen (1970), US
5	0.522	Gehrels (1979)
6	**0.550**	Lyot (1929)
6	0.550	Coffeen and Gehrels (1969)
6	0.550	Dollfus and Coffeen (1970), US
6	0.550	Gehrels (1979)
7	**0.617**	Dollfus and Coffeen (1970), French
8	0.650	Gehrels (1979)
8	**0.655**	Coffeen and Gehrels (1969)
8	0.655	Dollfus and Coffeen (1970), US
9	**0.685**	Coffeen and Gehrels (1969)
10	**0.740**	Coffeen and Gehrels (1969)
10	0.740	Dollfus and Coffeen (1970), US
11	**0.840**	Dollfus and Coffeen (1970), French
12	0.869	Gehrels (1979)
12	**0.875**	Coffeen and Gehrels (1969)
12	0.875	Dollfus and Coffeen (1970), US
13	**0.950**	Dollfus and Coffeen (1970), French
13	0.952	Gehrels (1979)
14	**0.990**	Coffeen and Gehrels (1969)
14	0.990	Dollfus and Coffeen (1970), US

Table 1: Classification of the data sets and wavelengths. The bold wavelengths are the ones used in the numerical simulations. Some of the combinations are plotted in Figure 6 (set 1), 7 (set 2), 8 (set 4), 9 (set 5), 10 (set 8), 11 (set 12), 12 (set 13) and 13 (set 14).

4.1. Temporal variability

It is known that the Venus atmosphere shows temporal variability such as variations in the column number density of the haze, the unknown UV-absorber and the cloud properties (Titov et al. 2018). For this research use is made of polarization data of Venus of several years, so it is interesting to use the data to search for temporal variability.

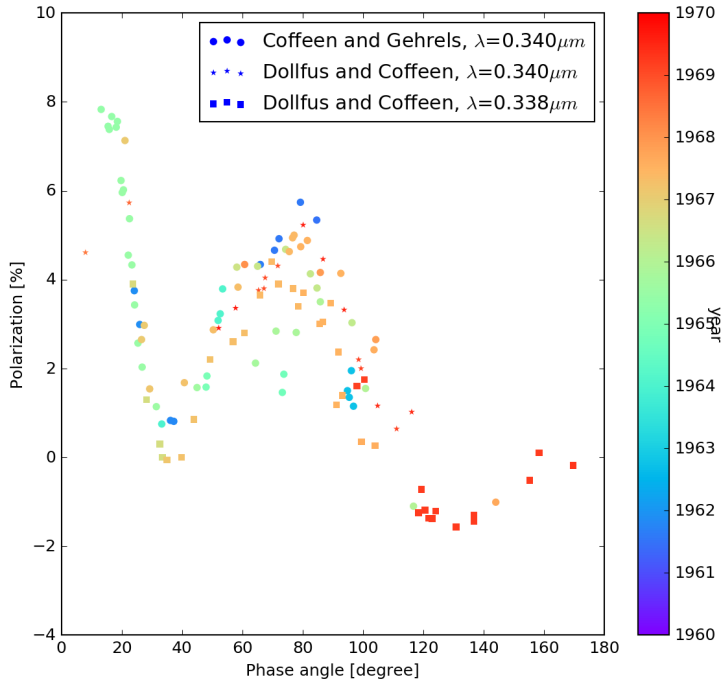

Fig. 6: All polarization data for set 1 (see Table 1): $\lambda = 0.340\mu m$ and $0.338\mu m$. The symbols refer to the papers in which the data was published and the colors to the years the data were taken.

It is in general hard to distinguish temporal variability. This is due to the fact that the measurements were not made with the goal to observe the temporal variability. Figure 6 illustrates this. In 1965, Coffeen and Gehrels mainly observed at small phase angles, while the middle phase angle range was observed by Dollfus and Coffeen in 1968 and the range with larger phase angles in 1970. Due to this spreading of phase angle regions over years, it is hard to observe variations over time. But some of the wavelength sets are suitable to analyse for temporal variability. These will be discussed below.

Set 5 (Figure 9) shows that the polarization of Venus observed by Gehrels in 1975/1976 is clearly higher than the polarization observed in the 1965/1968 period. The data obtained by Gehrels is for $\lambda = 0.522\mu m$ instead of $0.520\mu m$ but since this difference is so small, it is assumed that the higher polarization is not due to this difference in wavelength. This higher polarization can also be seen in the data of set 12 (Figure 11), again for data obtained by Gehrels. But for the data of set 4 (Figure 8) the polarization is highest in 1967. Sets 1, 2, 8, 9, 10, 11 and 14 do not contain any observations in the 1975/1976 time period. Set 6 only has 1 observation in this time frame, so this set will also be excluded. The same holds for set 3, it does not contain enough observations in the 1975/1976 period. Set 13 ($\lambda = 0.950$, Figure 12) shows higher polarisation in the phase angle range of 100°to 150°in the years 1975/1976. Since this is also data obtained by Gehrels, there are two possible conclusions: 1: The polarization was indeed higher in 1975/1976; or 2: There was a systematic error in the observations by Gehrels that resulted in higher polarization.

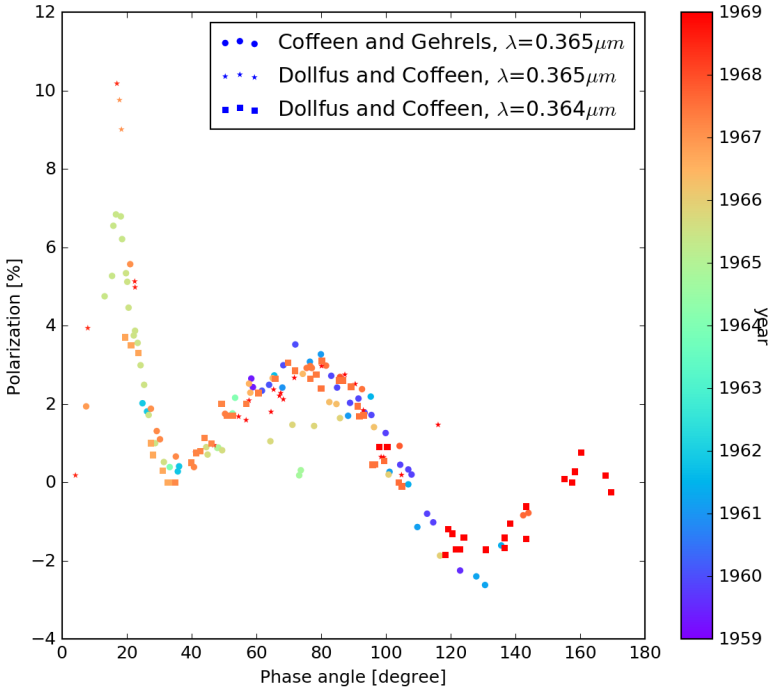

Fig. 7: Similar to Figure 6 except for set 2: $\lambda = 0.364\mu m$ and $0.365\mu m$.

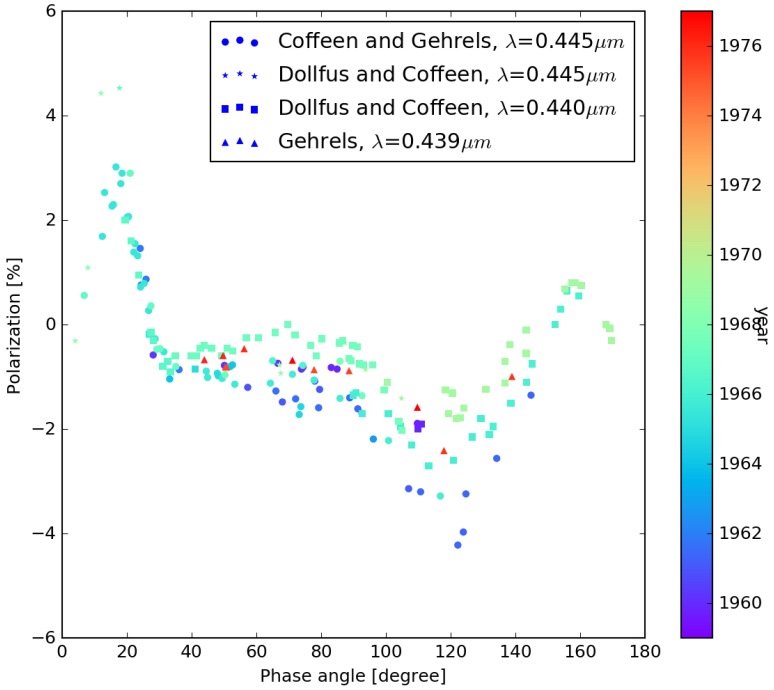

Fig. 8: Similar to Figure 6 except for set 4: $\lambda = 0.439\mu m$, $0.440\mu m$ and $0.445\mu m$.

In the period 1968-1970, higher polarization is observed in set 4 (Figure 8), set 5 (Figure 9), set 8 (Figure 10), set 12 (Figure 11) and set 14 (Figure 13). The other sets (1, 2, 3, 6, 9, 10, 11 and 13) do not contain observations in the years 1968 to 1970. From sets 5 and 12 it can be seen that the polarization of Venus observed around 1968-1970 is higher than the polarization observed in 1966 but not higher than the polarization observed in 1976.

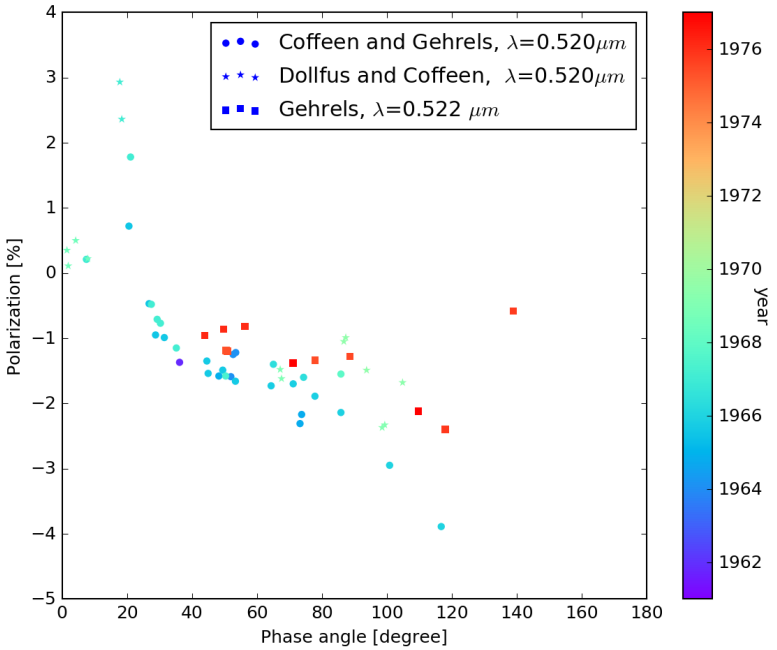

Fig. 9: Similar to Figure 6 except for set 5: $\lambda = 0.520\mu m$ and $0.522\mu m$.

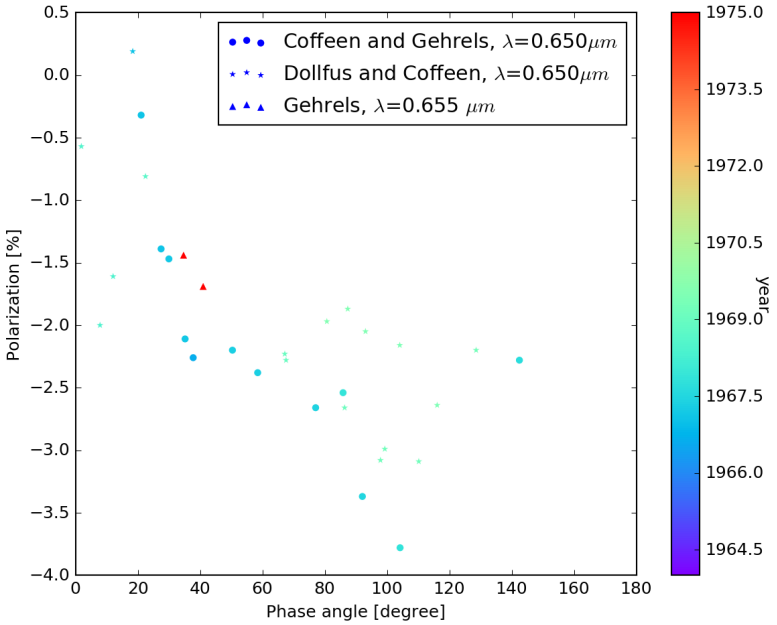

Fig. 10: Similar to Figure 6 except for set 8: $\lambda = 0.650\mu m$ and $0.655\mu m$.

From set 8 (Figure 10) and 14 (Figure 13) it is notable that the data by Dollfus and Cofeen has more outliers than the other data sets. This is data obtained between March 1969 and 4th of July 1969. During spring 1969 the observations were done by Veverka instead of Coffeen and Gehrels. When someone takes over the observations, it might happen that small changes occur due to differences in working method. Therefore it should be considered that those outliers could have been due to a different observer and are not necessarily changes in the atmosphere of Venus.

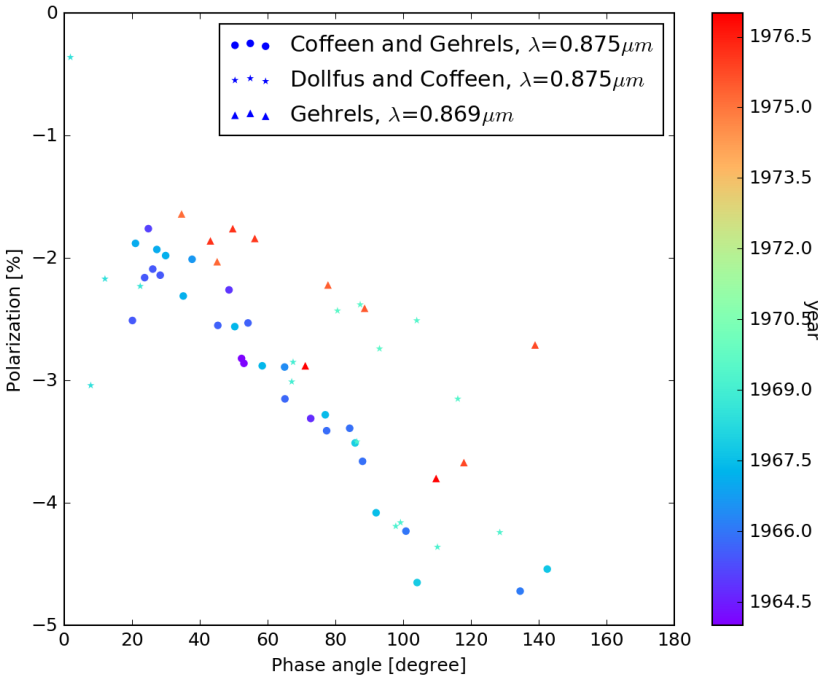

Fig. 11: Similar to Figure 6 except for set 12: λ = 0.869μm and 0.875μm

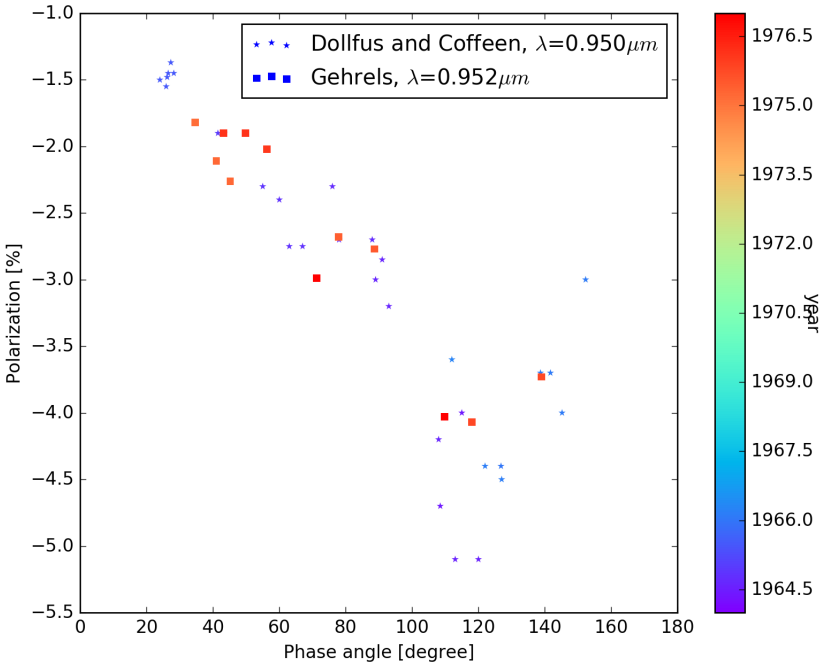

Fig. 12: Similar to Figure 6 except for set 13: λ = 0.950μm and 0.952μm.

Dollfus & Coffeen (1970) also mention a decrease in polarization in the years 1964/1965 in the ultraviolet region. From sets 1 (Figure 6), 2 (Figure 7) and 4 (Figure 8), it can indeed be seen that the data has more lower outliers in that period than other years.

Throughout it can be concluded that it is possible to see some variations with time: the polarization of Venus was higher around 1968-1970 and around 1975-1976. But for a reliable analysis it is im-

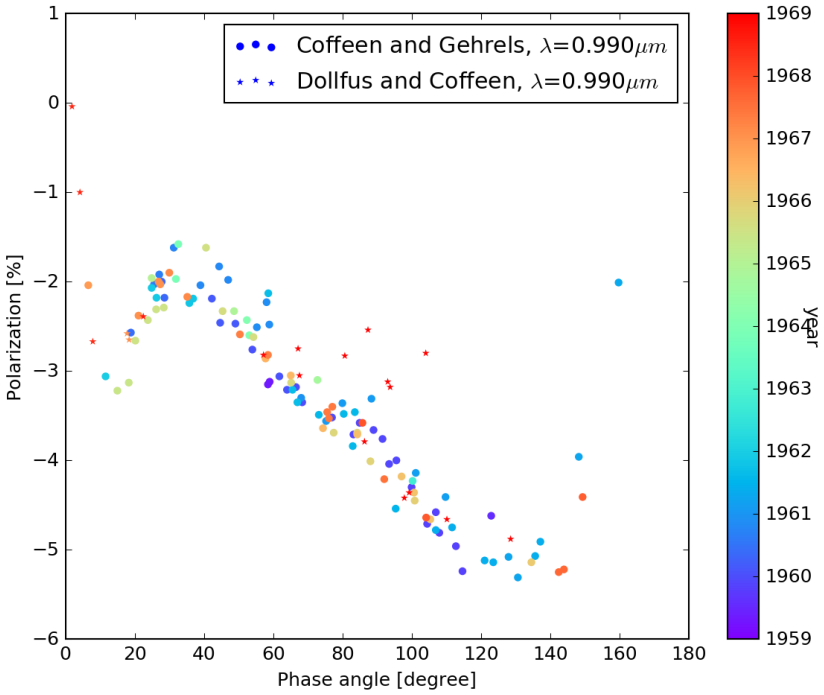

Fig. 13: Similar to Figure 6 except for set 14: $\lambda = 0.99\mu m$

portant to have more structured data points. For future research it is therefore important to measure over the whole phase angle range in a consecutive time period, for Venus this is approximately 1.6 Earth years (minus the time Venus is located behind the Sun and between the Earth and the Sun). And then to repeat this for multiple periods.

5. Method

To analyse the historical data, we use numerical simulations. With the numerical simulations we calculate polarization curves for specific input parameters. The numerically simulated polarization curves will be plotted in the same figures as the associated observations. In this way, polarization curves based on different cloud and haze properties can be compared with the observations and an estimation of the cloud and haze properties of Venus can be made. The parameter space in which the cloud properties will be searched for is based on literature, see subsection 5.2.

First a short description of the numerical code will be given, thereafter, the application to our research will be discussed in more detail.

5.1. Numerical code

The code that is used for the numerical simulations is called PyMieDAP (Python Mie Doubling-Adding Program) (Rossi et al. 2018). PyMieDAP is a Python module around FORTRAN routines to perform Mie scattering calculations and the Doubling-Adding method to perform radiative transfer calculations (Rossi et al. 2018). The PyMieDAP tool assumes a locally flat atmosphere that is horizontally homogeneous. For Venus this is a good assumption as long as the planet can be ver-

tically inhomogeneous. Vertical inhomogeneity can be created by stacking different atmospheric layers. The atmosphere consists of multiple layers that are added on top on each other. Each layer can consists of gas molecules and (i.e. cloud and haze) aerosol particles. The horizontally homogeneous atmosphere can also be transformed in an horizontal inhomogeneous atmosphere by defining bands at different latitudes with different atmospheric properties. This feature is very useful in order to compare with results from Kawabata et al. (1980) and to search for polar cap properties.

Rayleigh scattering

The scattering of the gas molecules is described by anisotropic Rayleigh scattering (see Hansen & Travis (1974)). The elements of this matrix are functions of the single scattering angle (Θ), wavelength (λ) and the depolarization factor (ρ) of the gaseous molecules. While the depolarization factor is dependent on the wavelength, PyMieDAP assumes a wavelength independent value (Rossi et al. 2018). For the Venus case this is not a problem since the depolarization factor of CO_2 is fairly wavelength independent (Rossi et al. 2018). To calculate the gaseous extinction optical thickness, b^m, of an atmospheric layer, the pressure difference across the layer is used together with the acceleration of the gravity of the planet and the mass per mole of the gas (see Rossi et al. (2018)):

$$b^m(\lambda) = \sigma^m(\lambda) N_A \frac{p_{bot} - p_{top}}{mg} \tag{6}$$

where σ^m is the molecular extinction cross-section in $\mu m^2 particle^{-1}$, N_A the constant of Avogadro, $p_{bot} - p_{top}$ the pressure difference in bars, m the mass per mole in atomic mass units and g the acceleration of gravity in ms^{-2}. The gaseous extinction optical thickness can also directly be given as input. PyMieDAP computes this molecular extinction cross section and the molecular scattering cross section. In order to do this, the refractive index of the gas is needed. PyMieDAP contains formulas to calculate the refractive index for a CO_2 based atmosphere (Rossi et al. 2018). The Venus atmosphere consists of CO_2 and N_2 gas. Appendix G contains formulas to implement the atmosphere that contains 97.5% CO_2 gas and 3.5% N_2 gas. In this Appendix it can be seen that the effect of the 3.5% N_2 gas on the refractive index is negligible. We will therefore continue with assuming pure CO_2 gas.

Mie scattering

Small particles can be added to the gas, these are called the aerosol particles. With a Mie-algoritm the aerosol single scattering matrix is computed. Mie theory holds for spherical particles only (Rossi et al. 2018; Hansen & Travis 1974). If this assumption is not valid for certain aerosols, you should provide the matrix or expansion coefficients to PyMieDAP yourself. But for the Venus case the assumptions of spherical particles holds, so there is no need to provide a matrix or expansion coefficients to PyMieDAP.

Finally PyMieDAP computes the optical thickness, the single scattering albedo and the single scattering matrix for all the layers. For the multiple scattering the adding-doubling radiative transfer

algorithm as described in de Haan et al. (1987) is used within PyMieDAP. This algorithm fully includes linear and circular polarization for all orders (Rossi et al. 2018) and is based on the theory that when the transmission and reflection are known for two layers the total transmission and reflection for the combined layer can be determined by computing the successive reflections back and forth between the two layers (Hansen & Travis 1974).

To calculate the disk-integrated signals, the signals should be integrated over the illuminated and visible part of the planet. PyMieDAP is pixel based and the planetary disk is divided into pixels. It is important to choose enough pixels to make sure the planet properties across each pixel can be assumed to be horizontally homogeneous. Then the total flux can be calculated at the center of each pixel. With the help of a summation over the illuminated and visible pixels, the disk-integrated flux vector is obtained (Rossi et al. 2018).

5.2. Input

Since multiple atmospheric layers are added on top of each other, PyMieDAP needs to know where all the layers start. This can be indicated with the bottom pressures of the layers. A relatively simple model is used to describe the Venus atmosphere. Starting at a surface pressure of 93*bar* (Lissauer & de Pater 2013) a layer of clear gas is used, followed by an optically thick cloud (starting at 1*bar*) with a haze on top (starting at 20*mb*). Above the haze another layer of clear gas is used, this layer starts at 1*mb* and fills the atmosphere till 0*bar* is reached, see Figure 14.

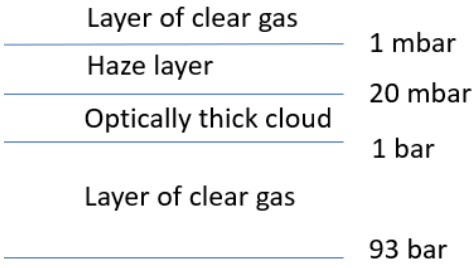

Fig. 14: Atmospheric layers: 93 *bar* is the surface pressure and the top of the atmosphere is located at 0 *bar*.

For the pressure profile of the cloud, the starting value was chosen to be the value obtained by Hansen & Hovenier (1974) so a cloud top pressure of 50*mb* was applied. But this value did not correspond to a nice fit with the data discussed in section 4. Therefore the altitudes mentioned in Titov et al. (2018) where translated into pressures with help of the pressure profile estimated by Jenkins et al. (1994). It was found that the 20*mb*, such as the other pressures mentioned before, which follow from those altitudes, were in good agreement with the observed polarization as mentioned in section 4. Therefore we continue with a cloud top pressure of 20*mb*.

Input	Explanation	Value
dpol (ρ)	Depolarisation factor CO_2	0.9
gravity (g)	Gravity of the planet	8.87 m/s^2
mma	Molecular mass in atomic mass units of CO_2	44
press	Pressure difference between the atmospheric layers used to calculate the gaseous extinction optical thickness	-
Aerosol properties	Effective radius and variance, optical thickness and refractive index	-
Cloud properties	Effective radius and variance, optical thickness and refractive index	-
rindex$_{gas}$	Determines the refractive index of the gas based on the type gas	CO_2

Table 2: Input PyMieDAP

The code needs, beside the definition of the atmospheric layers, various other input values. The input is shown in Table 2. Since the cloud is optically thick, the choice of the surface albedo is not important. The polarization curves for an albedo of, for example, 0.4 and 1.0 are identical. The choice is made to use a Lambertian surface with an albedo of 0.8 for Venus.

There are several distributions that can be used to describe the size distribution of the cloud and haze particles. Hansen & Travis (1974) investigated the effect on polarization of single scattering of unpolarized incident light of using different size distributions. Hansen & Travis (1974) found only small differences between the tested size distributions. Hansen & Hovenier (1974) made use of the Gamma-distribution to describe the Venus cloud particles. Nowadays more researchers use the Log-normal distribution to describe the Venus particles, for example Pérez-Hoyos et al. (2018) and Marcq et al. (2020). The parameters describing the *Two parameter gamma distribution* are the effective radius (r_{eff}) and the effective variance (v_{eff}) of the particles. The *Log normal distribution* uses r_g and σ. This means the r_{eff} and v_{eff} have to be translated into r_g and σ if we want to compare the distributions. This is done with:

$$r_g = \frac{r_{eff}}{(v_{eff})^{5/2}} \tag{7}$$

$$\sigma = e^{\sqrt{ln(1+v_{eff})}} \tag{8}$$

When this is implemented in PyMieDAP, the two size distributions can be compared. This is done for a selection of wavelenghts, see Appendix B. For the comparison we use a homogeneous Venus model containing clouds and hazes. The particles are spherical (Hansen & Hovenier 1974) which meet the assumption for the Mie scattering as discussed above. After looking at the figures, which can be reviewed in Appendix B, it can be concluded that also for the more complex Venus models, the difference between Gamma and Log-normal distribution is minimal. The biggest difference is 0.3% polarization but this is for phase angles 150° and upwards, the number of observations we have in that phase angle region is limited. It is therefore safe to continue in the foot steps of Hansen and Hovenier and use the Gamma-distribution for the haze and cloud particles.

As a starting point, the effective radius and variance of the cloud and haze particles will be chosen to be fixed: $r_{eff_{cloud}}$=1.05μm, $v_{eff_{cloud}}$=0.07 (Hansen & Hovenier 1974) and $r_{eff_{haze}}$=0.23μm, $v_{eff_{haze}}$=0.18μm (Knollenberg et al. 1980). This choice turns out to be justified, except for the $r_{eff_{haze}}$ which is updated to $r_{eff_{haze}}$=0.25μm, the figures that support this are added in Appendix A.

Other parameters that will be varied in order to investigate their influence on the measured degree of polarization, are displayed in Table 3. The parameters will be changed one by one: the other ones will be kept equal to the values found in the literature (as mentioned in this chapter).

Input	Explanation	Wavelength dependent
r_{eff} cloud	Effective radius of the cloud particles	No
v_{eff} cloud	Effective variance of the cloud particles	No
τ cloud	Optical thickness of the clouds	Yes
n_r cloud	Refractive index of the clouds	Yes
r_{eff} haze	Effective radius of the haze particles	No
v_{eff} haze	Effective variance of the haze particles	No
τ haze	Optical thickness of the haze	Yes
n_r haze	Refractive index of the haze	Yes

Table 3: Wavelength dependence PyMieDAP input

The Venus clouds are optically thick, therefore the optical thickness of the clouds should be at least of order ten. Hansen & Hovenier (1974) used a optical thickness of 256 in their paper about the polarization of Venus. Rossi et al. (2015) used a value of 30 in their analysis of the SPICAV-IR data. It is also possible to use the column number density, N in $particles/\mu m^2$, as an input parameter instead of the optical thicknesses of the cloud and haze (Rossi et al. 2018), as follows:

$$N = \frac{\tau}{\sigma^a} \tag{9}$$

where τ is the optical thickness of the cloud or haze and σ^a the scattering cross section in $\mu m^2/particle$. The advantage of using the column number density is the fact that the column number density is wavelength independent. Keeping the input for the effective radii, variances and refractive indices equal to what was discussed before, the column density is varied. In this way an optimal value of $N = 6.5\ particles\ \mu m^{-2}$ was found. This corresponds to an optical thickness of 40.5 for $\lambda = 0.340\mu m$ and 55 for $\lambda = 0.990\mu m$, when assuming sulfuric acid particles with the properties as discussed before. The optical thickness of the haze was varied between $\tau = 0.01$ and $\tau = 0.8$. It turned out that a very thin haze, with τ_h between 0.01 and 0.04 (N=0.09$particles\ \mu m^{-2}$) provided the best fit with the data.

The parameters discussed above are a starting point for fitting the Venus polarization data. The parameters that are varied in order to obtain a good fit are the refractive index of the cloud, the refractive index of the haze, the optical thickness of the cloud and the optical thickness of the haze. Every fit will be judged by the eye. Later on, after finding a proper fit for a homogeneous model, horizontal inhomogeneity was investigated. We aim to use one homogeneous model for all wavelengths as much as possible. This might not be possible everywhere and if not, it will be stated specifically.

6. Results

This section will discuss the results obtained during the research. Starting with a short analysis of the single scattering, followed by the sensitivity study. The sensitivity study results in best-fitting atmospheric parameters which will be used for the investigation on absorption and horizontal inhomogeneity.

6.1. Single scattering

Before presenting the results for the planet as a whole, it is insightful to discuss the single scattering due to the aerosols (Mie scattering). The features that are present in the single scattering should be visible in the overall polarization as well since the linear polarized flux (Q) should stay roughly the same, while the total flux (F) increases for multiple scattering. The single scattering flux and polarization can be found in Figure 15 for $\lambda = 0.340\mu m$, $0.520\mu m$, $0.740\mu m$ and $0.990\mu m$. The single scattering by the cloud particles shows the primary rainbow very clearly (the positive peak at the phase angles $\alpha \sim 18°$), this primary rainbow has a negative sign at the near infrared wavelengths ($\lambda = 0.740\mu m$ and $0.990\mu m$). Rainbows occur when there are one (or more) internal reflection(s) and the scattering angle reaches a maximum value as a function of the incident angle on the sphere (Hansen & Travis 1974). The change in sign is in agreement with the observed polarization data: those become completely negative at the near-infrared wavelengths, see Figures 11, 12, and 13. This strong dependence of the polarization observations on wavelength suggests that the cloud particle size must be on the order of the wavelength (Hansen & Hovenier 1974). The second rainbow starts around 70° phase angle but for the longer wavelengths this feature fades out. Around $\alpha = 150° - 160°$ and size parameter ~ 15 (the size parameter $= \frac{2\pi r_{eff}}{\lambda}$ (Hansen & Hovenier 1974)) there is a small hill in positive polarization: this is what van de Hulst (1957) calls the "anomalous diffraction". It is clearly visible for $\lambda = 0.340\mu m$ and $0.520\mu m$ but it slowly fades out for the longer wavelengths. This anomalous diffraction is due to the interference between diffracted light and light reflected and transmitted by the particle in the near-forward direction (Hansen & Hovenier 1974). The single scattering for the haze particles changes from negative for the shorter wavelengths to completely positive for the longer wavelengths. The haze particles are very small, especially compared to the near-infrared wavelengths. Therefore the single scattering of the haze particles starts to behave like Rayleigh scattering which results in the positive polarization curve for $\lambda = 0.990\mu m$.

6.2. Sensitivity study

Now the results of the sensitivity study into the influence of parameter values on the planet polarization signal will be discussed. The first thing to investigate is the influence of the optical thickness of the cloud and the refractive index of the cloud particles. Hansen & Hovenier (1974) already investigated the sensitivity for the effective radius of the cloud particles and the refractive index of

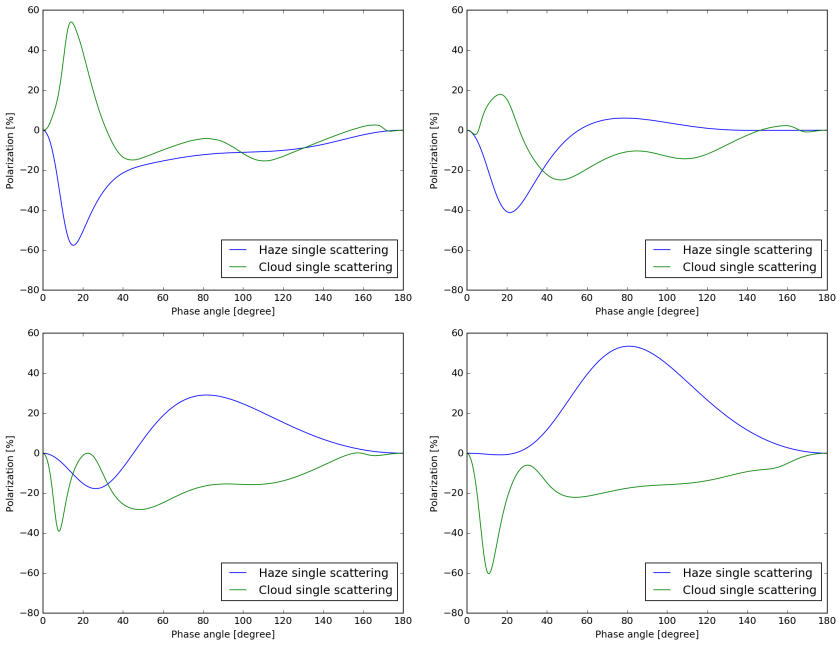

Fig. 15: Single scattering polarization curves for the cloud and haze aerosols. *Top left*: λ = 0.340μm, *top right*: λ = 0.520μm, *bottom left*: λ = 0.740μm and *bottom right*: λ = 0.990μm.

the cloud particles for λ = 0.365μm, 0.550μm and 0.990μm. This paper contributes to their research by expanding this to more wavelengths and also adding the sensitivity study for the haze.

The refractive index is related to the type of aerosol. From the refractive index that best fits the observations, the type of aerosol can be determined. It indeed can be seen in the figures of Appendix C that the values that give a nice fit are between n_r=1.47 for λ=0.340μm and n_r=1.43 for λ=0.990μm such as Hansen & Hovenier (1974) already derived. Meaning that the cloud particles are composed of 75% sulfuric acid solution.

Changing the optical thicknesses of the haze and clouds has different effects for the UV and the near-infrared wavelengths. Looking at Figure 18 and 19 helps us with explaining this. Refreshing the relation between optical thickness and column number density, shows that with decreasing optical thickness the column number density decreases as well. A decreasing column number density for the cloud particles indicates a stronger contribution of the gas, so the curve will start to behave more like Rayleigh scattering and the polarization goes up in the mid phase angles. For longer wavelengths (starting at λ = 0.650μm), see for example Figure 19, the effect of adding gas to the clouds is only small and therefore no significant changes in the curves are found. For the column number density of the haze it is the other way around: the effect in the shorter wavelengths is less strong than the effect in the longer wavelengths, see Figure 22 and 23. On top of that, it can clearly be observed that for the longer wavelengths, the polarization decreases when the column density decreases. In this case adding more gas does not result in more positive polarization but it does strengthen the effect of the negative polarization.

For the sensitivity study, the UV-absorption (see Section 6.4) has not yet been added to the model, this explains why the fit is not optimized for the UV wavelengths. For some cloud/haze properties the effects of varying the parameters only appear after a certain wavelength. This is why we sometimes discuss a range of wavelengths. The figures only show one wavelength, this is to keep the reading concise, but figures for all wavelengths can be found in Appendix C.

Varying the refractive index and the optical thickness of the cloud or haze influences the polarization curves in the following way:

– For $0.340\mu m < \lambda < 0.550\mu m$: Increasing the **refractive index of the cloud particles**, shifts the primary rainbow to the smaller phase angles and shifts the curve down for the middle phase angles, see Figure 16. For $0.550\mu m \leq \lambda \leq 0.99\mu m$: Increasing the refractive index of the cloud particles, shifts the primary rainbow to the larger phase angles and increases the peak at $\alpha \sim 160°$, see Figure 17.

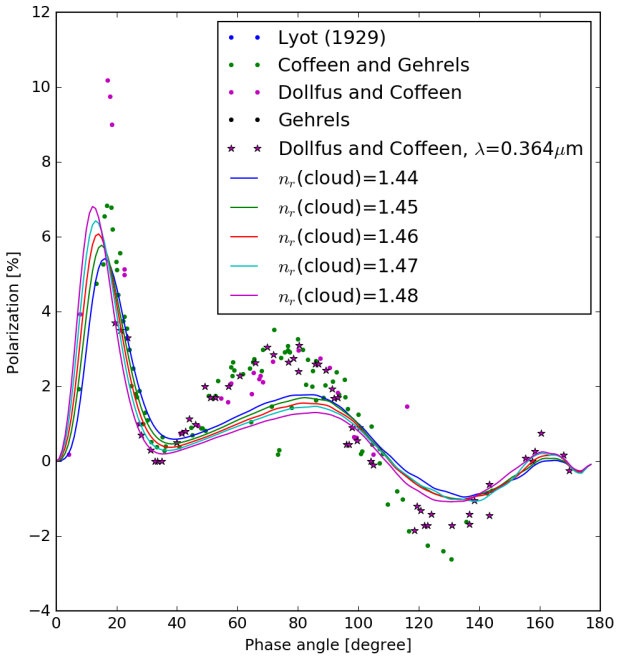

Fig. 16: Varying refractive indices for the cloud particles for λ=0.365μm and 0.364μm. Input: r_{eff}(cloud)=1.05μm, v_{eff}(cloud)=0.07, r_{eff}(haze)=0.25μm, v_{eff}(haze)=0.18, N(cloud)=6.5 particles μm^{-2}, N(haze)=0.09 particles μm^{-2}, n_r(haze)=1.46

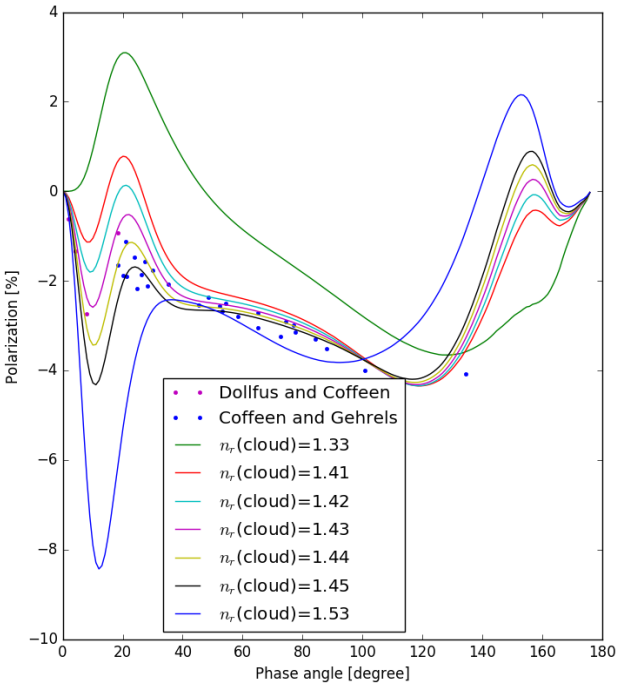

Fig. 17: Varying refractive indices for the cloud particles for λ=0.740μm. Input: similar to Figure 16 except for n_r(haze)=1.43.

– Increasing the **optical thickness of the cloud** lowers the polarization in the 30°to 150°phase angle region, see Figure 18. For $\lambda > 0.650\mu m$, the differences are minimal, see Figure 19.

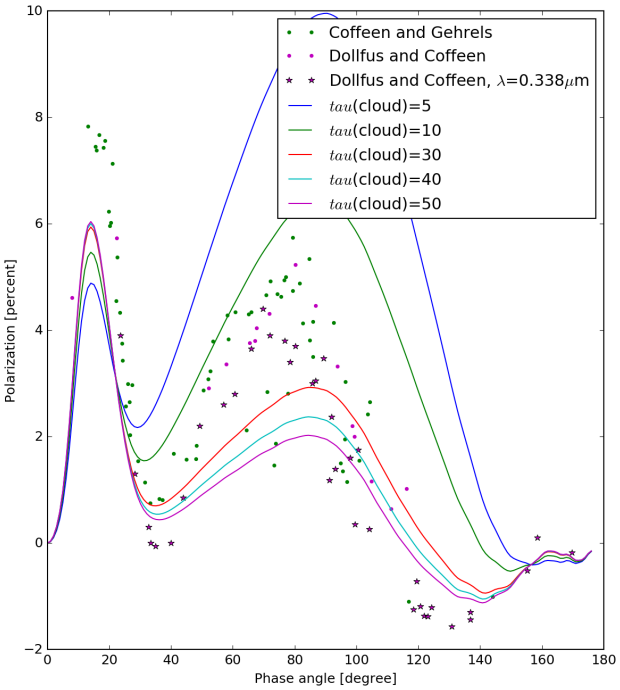

Fig. 18: Varying the optical thickness of the cloud for λ=0.340μm and 0.338μm. Input: similar to Figure 16 except for n_r(cloud)=1.466 & n_r(haze)=1.466

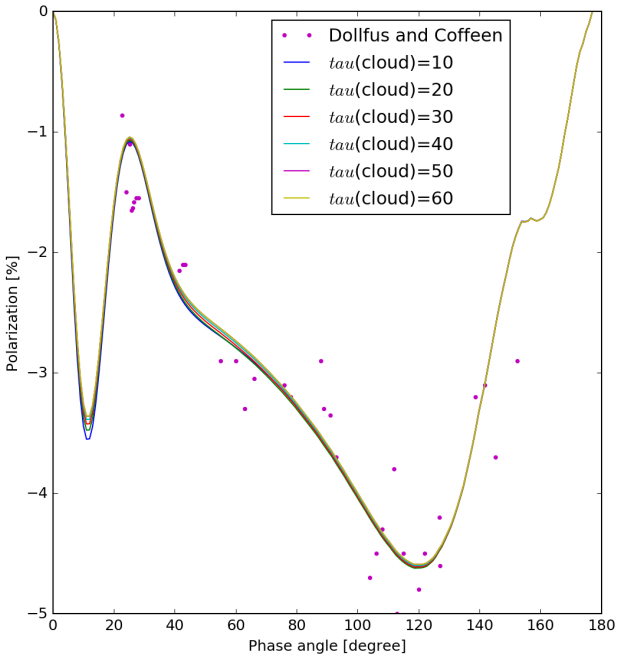

Fig. 19: Varying the optical thickness of the cloud for λ=0.840μm. Input: similar to Figure 16 except for n_r(cloud)=1.43 & n_r(haze)=1.43

– For 0.340μm < λ < 0.685μm: Increasing the **refractive index of the haze** shifts the entire curve to lower polarization, see Figure 20. For 0.685 ≤ λ ≤ 0.990μm: Increasing the refractive index of the haze shifts the entire curve to higher polarization, see Figure 21.

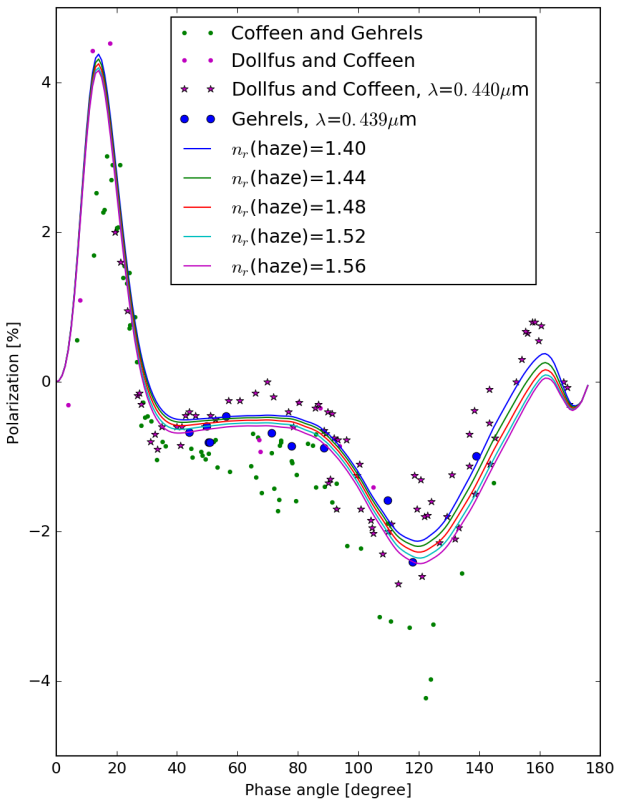

Fig. 20: Varying refractive index of the haze particles for λ=0.445μm, 0.440μm and 0.439μm. Input: similar to Figure 16 except for n_r(cloud)=1.45.

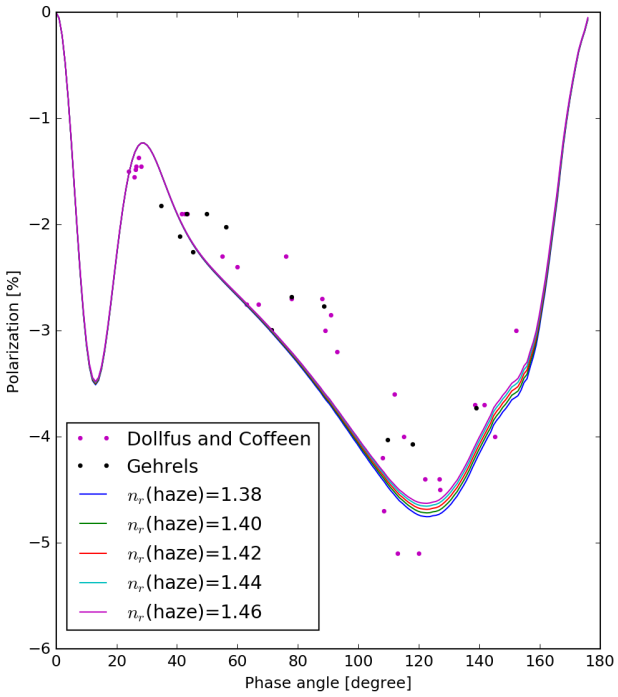

Fig. 21: Varying refractive index of the haze particles for $\lambda = 0.950\mu m$. Input: similar to Figure 16 except for n_r(cloud)=1.43.

– Varying the **optical thickness of the haze** especially influences the peaks around $\alpha \sim 18°$, $\alpha \sim 120°$, $\alpha \sim 160°$. Increasing the optical thickness of the haze, weakens (making positive values less positive and negative values less negative) the percentage of polarization in the peaks mentioned before, see Figure 22. The longer the wavelength, the more the effect spreads over the phase angles, see Figure 23.

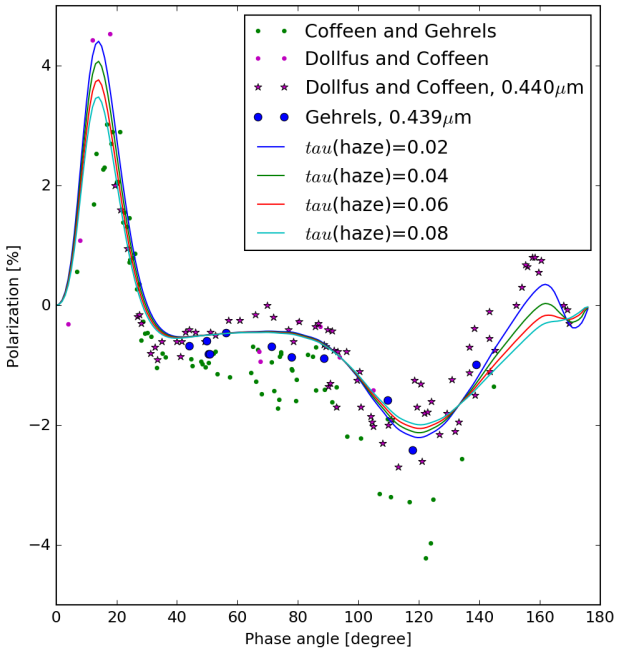

Fig. 22: Varying optical thickness of the haze for λ=0.445μm. Input: similar to Figure 16 except for n_r(cloud)=1.45 & n_r(haze)=1.45.

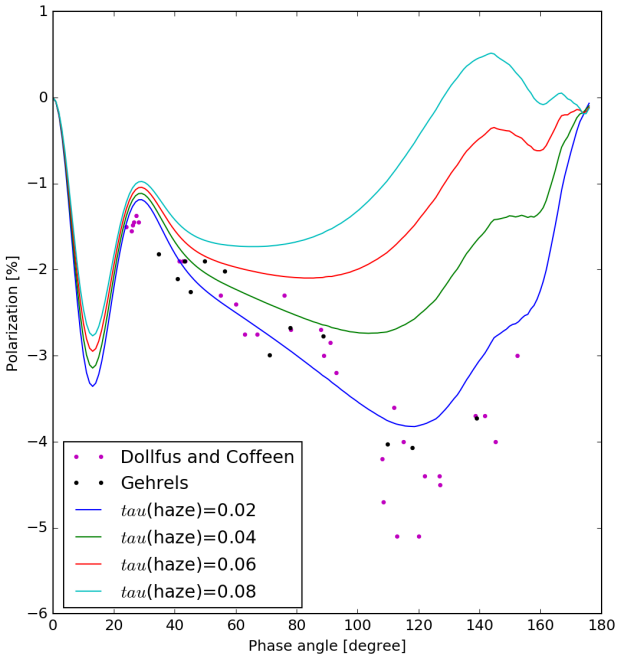

Fig. 23: Varying optical thickness of the haze for λ=0.950μm. Input: similar to Figure 16 except for n_r(cloud)=1.43 & n_r(haze)=1.43.

From this sensitivity study it can be concluded that it is important to make polarization measurements in a broad range of wavelengths. The properties of the cloud (optical thickness and refractive index) can be estimated when there are only a few wavelengths available. But if you want to estimate the optical thickness of the cloud better than 'optically thick' or 'optically thin', you really need the UV-wavelength region. To distinguish the properties of the haze, the UV-wavelengths are needed to estimate the refractive index and the near-infrared wavelengths are needed to estimate the optical thickness of the haze.

6.3. Starting point data exploration

Now that the sensitivity study is done, best-fitting values for the parameters can be found to continue the research. The values that are chosen to continue with are the values that resulted from the best fit in all wavelengths. So it could be that for specific wavelengths the best-fitting values are actually different than the ones that are used during the research. Since the optical thickness is wavelength dependent, the choice is made to use the column number density from now on. The values for the column number density were already determined in section 5.2: N_{cloud} = 6.5 $particles\ \mu m^{-2}$ and N_{haze} = 0.09 $particles\ \mu m^{-2}$, these will stay the same. The best-fitting refractive indices, for the haze and cloud particles, to the historical data where searched in a wide parameter space (between n_r=1.40 and n_r=1.60). The optimized values were found very close to the values of Hansen & Hovenier (1974). These values are in good agreement with the values found by Palmer & Williams (1975) for 75% sulfuric acid. Meaning that the values vary from n_r = 1.47 to n_r = 1.43 for respectively λ=0.340μm to λ=0.990μm. The effective radii were already discussed in section 5.2: $r_{eff}(cloud)$ = 1.05μm and $r_{eff}(haze)$ = 0.25μm.

6.4. Absorption

There is still a lot unknown about the absorption in the Venus clouds. From the numerical simulations we can see that adding absorption is definitely necessary in the UV-wavelengths region (Figure 24). It was the only way to really improve the fit in the UV-wavelengths. Absorption is linked to the imaginary part of the refractive index. Absorption in the mode 2 particles (particles with effective radii of 1.05μm and a sulfuric acid concentration of 75% (Rossi 2016)) on the order of 10^{-4}-10^{-3} is added to the model. According to Marcq et al. (2020) there should be absorption in the mode 1 particles (particles with effective radii of 0.25μm that consist of sulfuric acid with various concentrations (Rossi 2016)) as well, using their values ($1.5 * 10^{-2}$ for $\lambda = 0.340\mu m$) for the imaginary refractive index of the mode 1 particles results in Figure 25. The ratio between the mode 1 and mode 2 particles corresponds to the ratio in which the opacity is due to mode 1 or mode 2. In this figure the real parts of the refractive indices for the mode 1 and mode 2 particles are identical. For our model, adding these mode 1 particles with absorption does not improve the fit with the historical polarization curves. First of all, the peak of the primary rainbow shifts to smaller phase angles and is too low so that it does not align with the polarization observations anymore. Second, the shape flattens too much from phase angle 90° onwards causing the peak of negative polarization at $\alpha = 120°$ to be shifted to larger phase angles. The lack of positive effect of the models by Marcq et al. (2020) on the fit with the historical polarization data could be caused by the fact that Marcq et al. (2020) investigated very regional data, maybe so regional that the influence on the total disk-integrated polarization is negligible. The data Marcq et al. (2020) used was obtained by ESA's Venus Express mission in 2006-2014, it could be that there were less mode 1 particles with absorption when our data was taken because of Venus's active clouds and possible vulcanism. We have decided that for this research, the absorption will be limited to the mode 2 particles.

The purpose of this paper is not to answer questions on the nature of the UV-absorption but to investigate the effect of the polarization curves for different places of absorption. We will look at absorption around the equator, absorption at the poles, absorption in the form of patchy clouds and absorption in a subsolar cloud.

6.4.1. Patchy clouds

A method to spread the absorber across the planet is with the help of patchy clouds: clouds with absorption are created, these clouds are mixed with clouds containing the same properties but without the absorption. In this way a clouded planet can be created with absorption that is non-homogeneously spread. The patchy clouds cover the entire planet. From Figure 26, it can be seen that it is possible to find a fit to the data by modelling Venus with 80% clouds with absorption and 20% clouds without absorption. But the numerical polarization curve of the homogeneous clouds with absorption follows the shape of the observations best for $\alpha > 110°$. The value for n_i depends on the wavelength and varies between 10^{-3} (for $\lambda = 0.340\mu m$) and $3*10^{-3}$ (for $\lambda = 0.400\mu m$). Since the Venus clouds are dynamically very active it is possible that the absorber is non-homogeneously

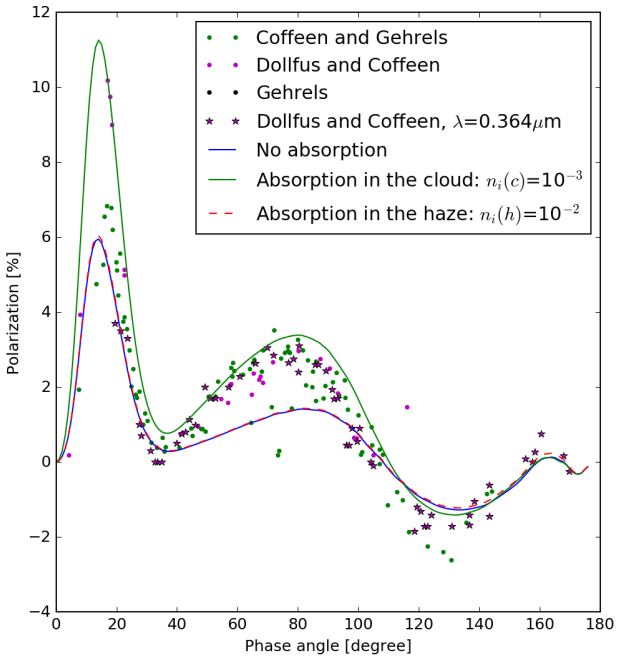

Fig. 24: No absorption (blue line), absorption in the cloud particles (green line, $n_i = 10^{-3}$) and absorption in the haze particles (red line, $n_i = 10^{-2}$) for λ=0.365μm.

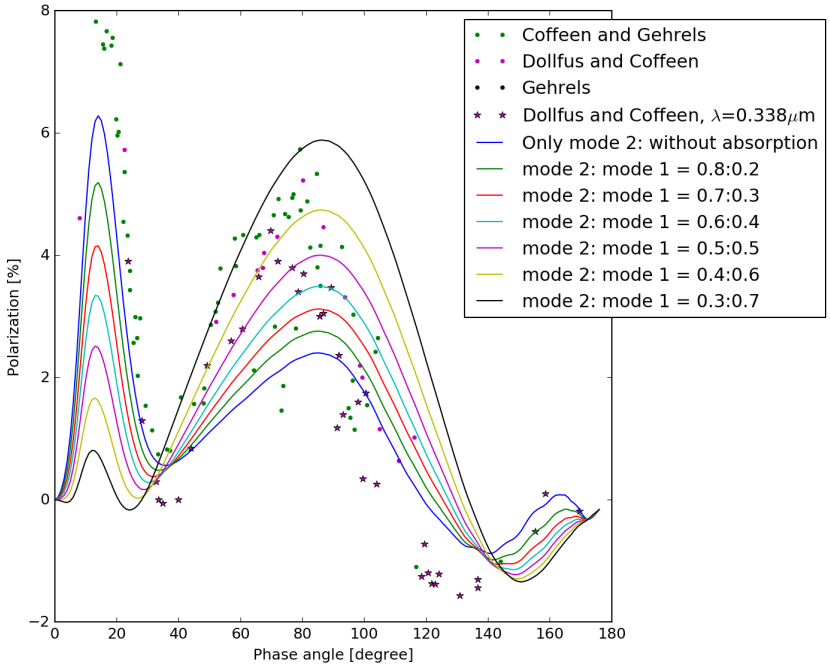

Fig. 25: Addition of mode 1 particles with absorption of $1.5 * 10^{-2}$ for λ=0.340μm and λ=0.338μm.

spread around the planet. The figures for λ = 0.340μm and 0.400μm can be found in Appendix D. The wiggles that are visible in the polarization curves are due to the limited number of pixels (n_{pix}=65). A higher number of pixels reduces the wiggles but because of the increasing computation time, we can not use too many pixels.

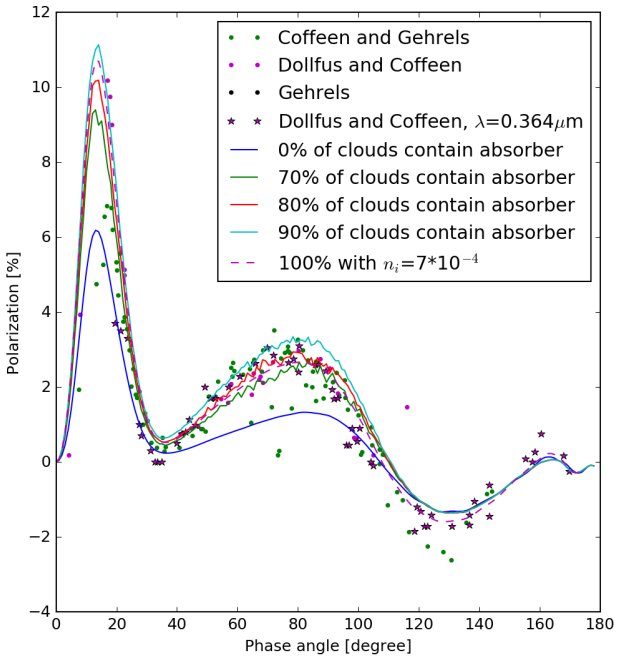

Fig. 26: Different percentages of patchy clouds containing absorption for λ=0.365μm and 0.364μm (set 2). Input: r_{eff}(cloud)=1.05μm, v_{eff}(cloud)=0.07, r_{eff}(haze)=0.25μm, v_{eff}(haze)=0.18, N(cloud)=6.5 particles μm^{-2}, N(haze)=0.09 particles μm^{-2}, n_r(cloud)=1.46, n_r(haze)=1.46 and n_i(cloud)=$1.5 * 10^{-3}$ for the absorbing patchy clouds.

6.4.2. Absorption at the equator and around the poles

Now, absorption will be added only to the equator or poles, respectively. The south pole covers the area from −90° to −50° latitude, the equator covers −50° to 50° latitude and the north pole region covers the area from 50° to 90° latitude. In Figure 27, it can be seen that the fit of the polarization curve to the polarization observations improves in the phase angle range from 100° till 170° when adding absorption to the equator only. When the absorption is only added at the poles, the polarization stays way too low in the middle phase angles. It can be concluded that it is more likely for the absorber to be mainly present around the equator area instead of the polar area. It is known that there exist a transition between the cloud and haze properties around 50° latitude (Titov et al. 2018) so this hypothesis could be feasible. Similar figures for λ = 0.340μm and 0.400μm can be found in Appendix D.

6.4.3. Subsolar cloud

The next possibility to investigate is the presence of absorption in the subsolar cloud. The subsolar cloud is the cloud that exists around the subsolar point. The subsolar point is the point where the sunlight enters the atmosphere exactly perpendicular, so where the Sun is overhead. Since Venus spins very slowly around his own axis, this subsolar point stays quite fixed with respect to the planetary surface for a longer period. But the clouds rotate fast, the top level of the clouds rotates in roughly 4 Earth days (NASA 2018). Meaning that the atmosphere above the clouds heats up and this hot atmosphere can influence the local cloud and/or haze properties. The cloud particles

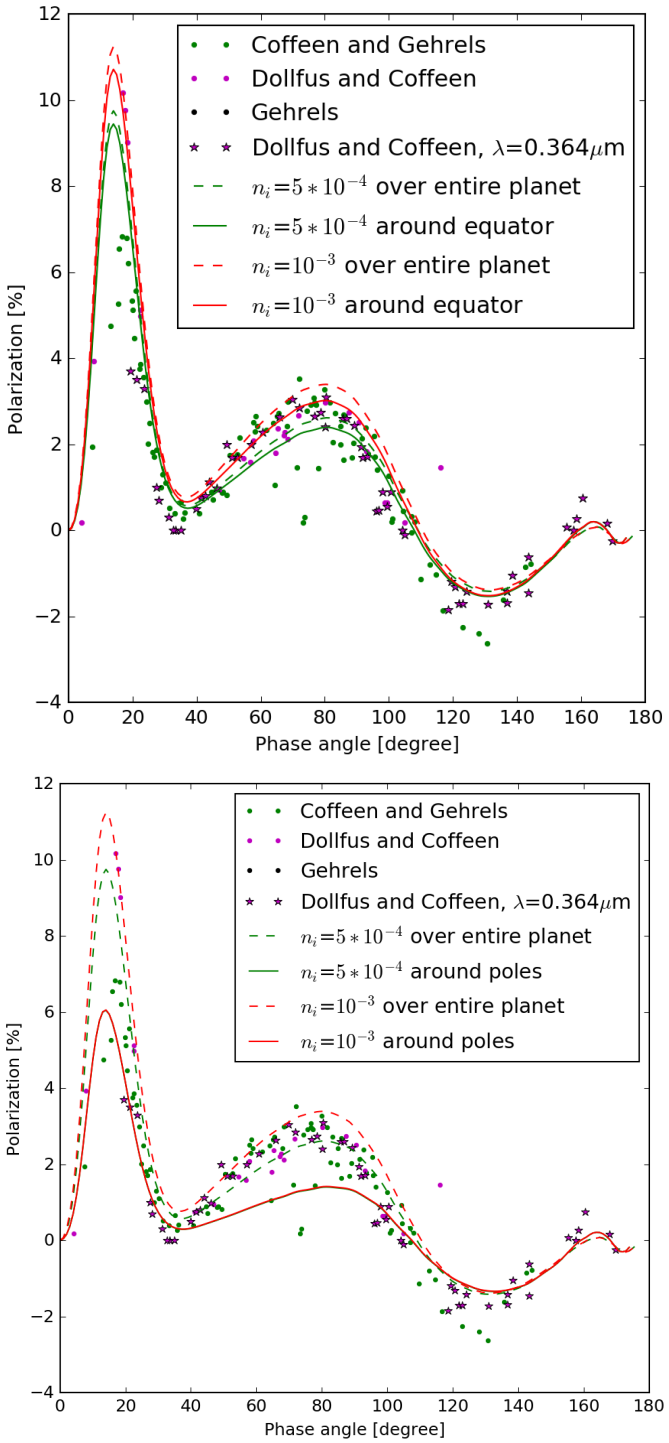

Fig. 27: Effect of adding absorption to the equator (top) and poles (bottom) for λ=0.365μm and λ=0.365μm (set 2). For the bottom figure, the green en red line coincide. Input: r_{eff}(cloud)=1.05μm, v_{eff}(cloud)=0.07, r_{eff}(haze)=0.25μm, v_{eff}(haze)=0.18, N(cloud)=6.5 particles μm^{-2}, N(haze)=0.09 particles μm^{-2}, n_r(cloud)=1.46, n_r(haze)=1.46.

around the subsolar point are given an imaginary part of the refractive index between 10^{-4} and 10^{-3}, depending on the wavelength. Using this method, a subsolar cloud with absorption is created. From Figure 28 it can be seen that the fit improves for the larger phase angles but has too little polarization for the middle phase angles. It is therefore not likely that the absorption is limited to the subsolar cloud. The figures for λ = 0.340μm and 0.365μm can be found in Appendix D.

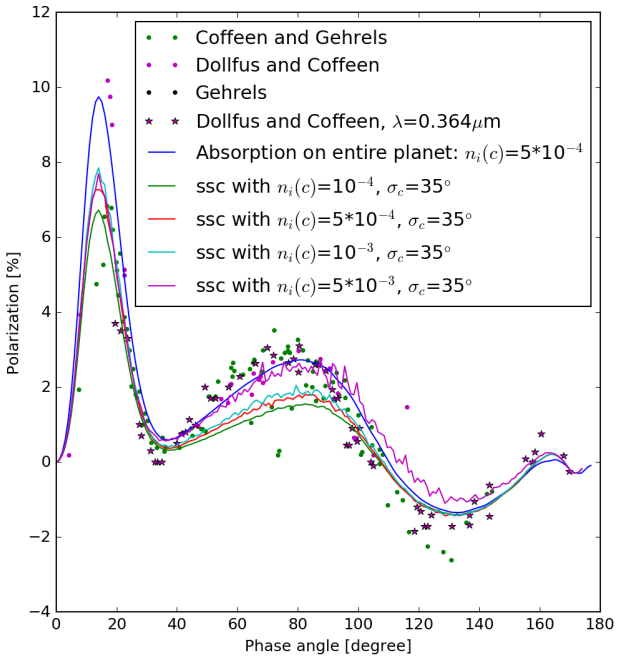

Fig. 28: Subsolar cloud (ssc) containing absorber for λ=0.365μm and 0.364μm (set 2). Input: Equal to input of Figure 27 but with n_i(cloud) variable for the subsolar cloud.

6.4.4. Absorption in the gas

It is also possible to have absorption in the gas instead of in the particles. Although CO_2-gas is not absorbing at UV wavelengths there can be another, yet unidentified gas absorbing at those wavelengths. With applying a value for the *optical thickness related to the gaseous absorption*, absorption in the gas can be simulated. The results for different values of this gaseous absorption in the cloud layer for $\lambda = 0.365\mu m$ are shown in Figure 29. From this figure (and Figure D.10 and D.12 in the appendix) it can be seen that it is possible to find a good fit to the historical data using absorption in the gas. The supporting figures for $\lambda = 0.340\mu m$ and $0.400\mu m$ can be found in Appendix D. The only disadvantage of adding absorption to the gas is the higher peak with maximum polarization in the smaller phase angles region: this peak is too high. Values for the gaseous absorption optical thickness vary between 0.9 (λ=0.340μm) and 1.1 (λ=0.400μm). Adding absorption to the gas in the haze does not improve the fit.

6.4.5. Conclusions on absorption

Several ways of adding the absorption have been discussed in this section. The models with the best results are presented in Figure 30. From this figure it is clear that it is not possible to conclude which model is most likely. The largest difference lies within the 15° phase angle where the polarization of the patchy cloud model is 1.5% polarization lower than the others, see the red line in Figure 30. Because of the similarity it will be really hard to draw a conclusion using only disk-integrated polarization data. But it can be said for sure that there should be some kind of UV-absorption in the clouds. The values needed for the imaginary part of the refractive index of the cloud parti-

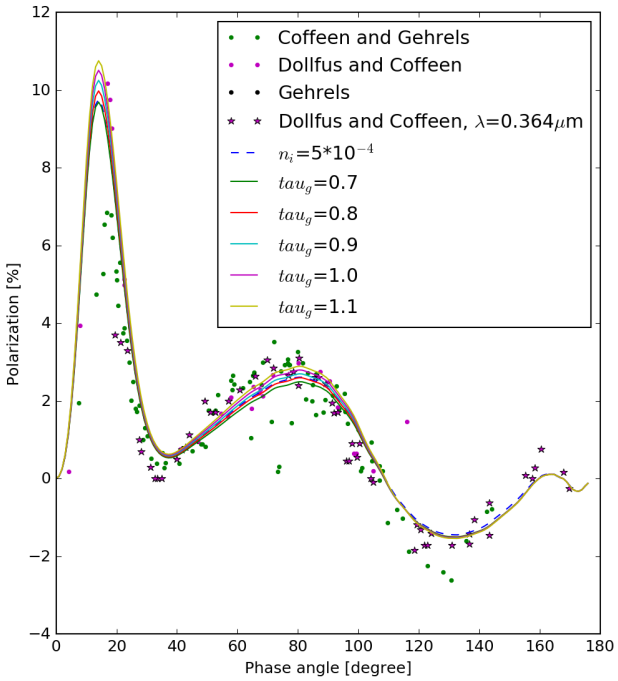

Fig. 29: Adding absorption to the gas for λ=0.365μm and 0.364μm (set 2). tau_g represents the absorption optical thickness of the gas. r_{eff}(cloud)=1.05μm, v_{eff}(cloud)=0.07, r_{eff}(haze)=0.25μm, v_{eff}(haze)=0.18, N(cloud)=6.5 particles μm^{-2}, N(haze)=0.09 particles μm^{-2}, n_r(cloud)=1.45, n_r(haze)=1.45.

cles, order 10^{-3}, 10^{-4}, are not in agreement with those of 75% H_2SO_4 H_2O solutions (Palmer & Williams 1975). Although Nozière & Esteve (2005) did some research on sulfuric acid aerosols in the Earth's atmosphere and concluded that the absorption by sulfuric acids can increase over time as a consequence of organic reactions (adol condensation) with acetaldehyde (CH_3CHO). For this research Nozière & Esteve (2005) observed strong absorption bands at the 0.225μm to 0.430μm spectral range. To calculate the associated imaginary part of the refractive index they assumed 1μm 80% sulfuric acid particles (for Venus this is assumed to be 1.05μm and 75%) and a temperature of 230K. Assuming a lifetime of 2 years for the particles, they found an imaginary part of the refractive index of $6.8x10^{-4}$ for = 0.341μm. So far, we do not know about the presence of carbonyl compounds in the Venus atmosphere. But, possibly, volcanic activity could influence the H_2SO_4 concentration or could bring in other reactant concentrations (maybe even carbonyl compounds).

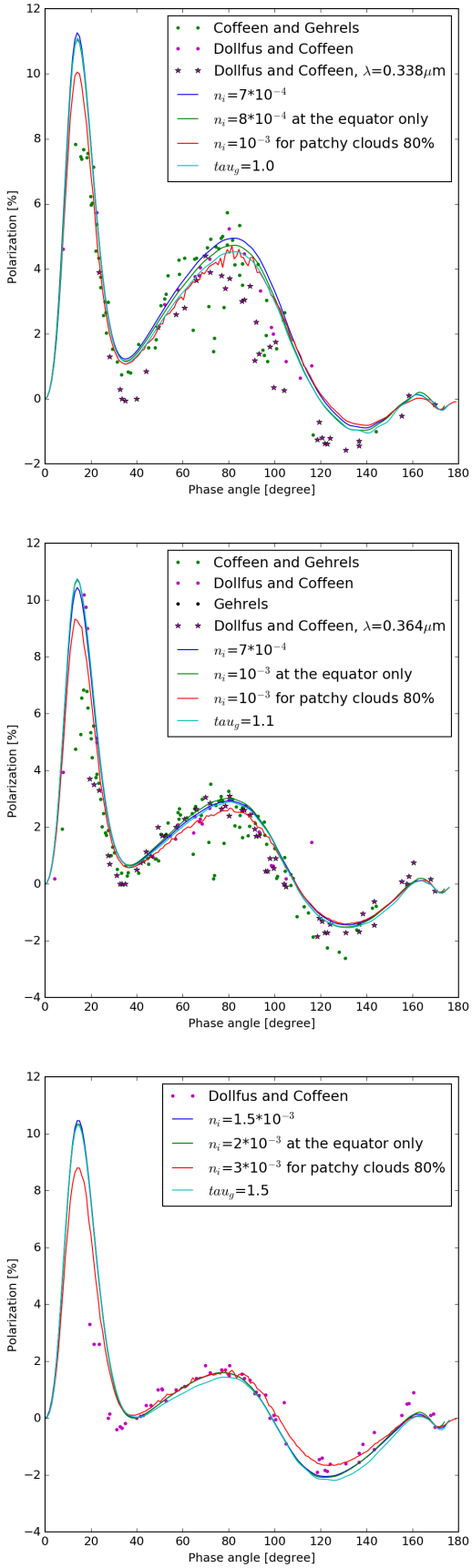

Fig. 30: Absorption summarized in one figure. See Figure 27 for the input. *Top*:λ=0.34μm and λ=0.338μm (set 1), but the input with n_r(cloud)=n_r(haze)=1.466. *Middle*: λ=0.365μm and λ=0.364μm (set 2). *Bottom*: λ = 0.400μm (set 3), but the input with n_r(cloud)=n_r(haze)=1.45.

6.5. Polar cap region

In 1996, Sato et al. (1996) studied the Pioneer Venus data of the polar regions of Venus. With their analysis Sato et al. (1996) found haze particles of r_{eff}=0.25 ± 0.05μm, v_{eff}=0.25 ± 0.05 and n_r=1.435 ± 0.02 (for λ=0.55μm) in the north polar region. In the south polar region they found slightly different values: r_{eff}=0.29 ± 0.02μm, v_{eff}=0.25 ± 0.03 and the real part of the refractive index n_r=1.45 ± 0.02 for λ=0.55μm. For our research, we will vary the properties of the north and south polar haze and cloud but they will be varied in the same way. Meaning that variations that are applied to the north polar region will also be applied to the south polar region.

Kawabata (1981) investigated the polarization of planets with polar cap features. He found that the effect of strongly polarizing polar regions is clearly visible in the disk-integrated polarization data. With his research he found indications that the polar caps of Venus should have strongly polarizing clouds and hazes. The transition to the polar cap region was found to be around 50° latitude (Kawabata 1981). Titov et al. (2018) summarizes several research papers that imply a transition to the polar cap region at around 50° latitude. This is the latitude transition that is used during our research as well. This paper contributes to Kawabata (1981) by investigating which changes in cloud or haze properties can be observed in the disk-integrated polarization data. This investigation is also applied at the historical Venus data to investigate the polar cap features of the Venus atmosphere.

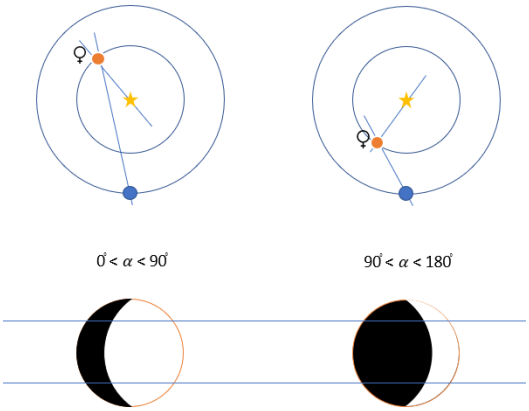

Fig. 31: *Top*:Representation of planet position for small and large phase angles, where the yellow star is the Sun, the orange circle Venus and the blue circle the Earth. *Bottom*: Part of the planet that contributes to the polarization (white) for the shown phase angle.

Changing the properties of the polar regions is expected to mainly effect the polarization at larger phase angles. This can be explained by looking at Figure 31. The top part of the figure represents the positions of the Sun (yellow star), Earth (blue circle) and Venus (orange circle), while the bottom part of the figure represents with white the parts of Venus that contribute to the polarization at the sketched position. The blue lines in the bottom part of the figure represent the latitude lines for the poles. It is clear that at a larger phase angle region (right figure) the contribution of the poles compared to the contribution of the equatorial area is larger than at the small phase angles (left

figure). Only a selection of figures will be displayed in this section, the remaining figures can be found in Appendix E.

6.5.1. Haze properties

When changing the properties in the polar regions (column number density, effective radius, top pressure, and refractive index) of the haze, their effects on the disk-integrated polarization can be investigated. Changing the microphysical properties of the haze particles in the polar regions seems to have minimal effects on the disk integrated polarization. The effects will be discussed below.

Changing the refractive index of the haze particles has a minimal effect, see Figure 32. Similar figures for other wavelengths can be found in Appendix E.4 and show as little variations as Figure 32. There is thus no indication that the haze refractive indices should be different around the polar region.

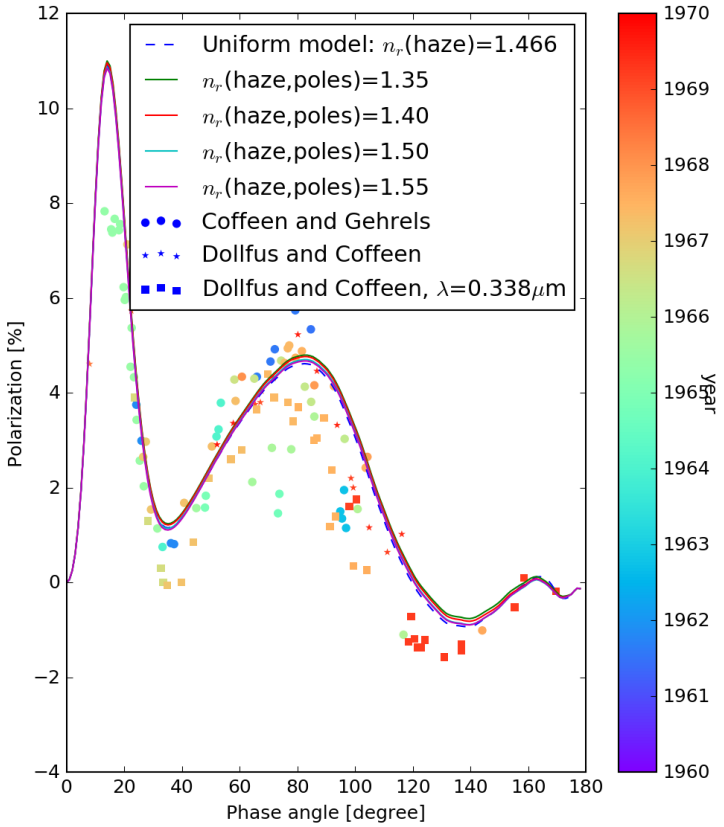

Fig. 32: Varying the refractive index of the haze particles in the polar region for λ=0.340μm and 0.338μm (set 1). Input: see Figure 27 but with n_r(cloud)=1.466, n_r(haze, equatorial)=1.466.

It is possible, especially in the near-infrared wavelength region, to see an effect of different optical thicknesses of the haze. The optical thickness of the haze is varied between τ = 0.01 (N=0.03 $particles\ \mu m^{-2}$) and τ = 0.5 (N=1.47 $particles\ \mu m^{-2}$). Despite the fact that several studies found a thicker haze in the polar regions (Sato et al. 1996; Kawabata 1981) applying this to the historical

polarization Venus data does not lead to a better fit, see for example Figure 33. The figures for more wavelengths are shown in Appendix E.1.

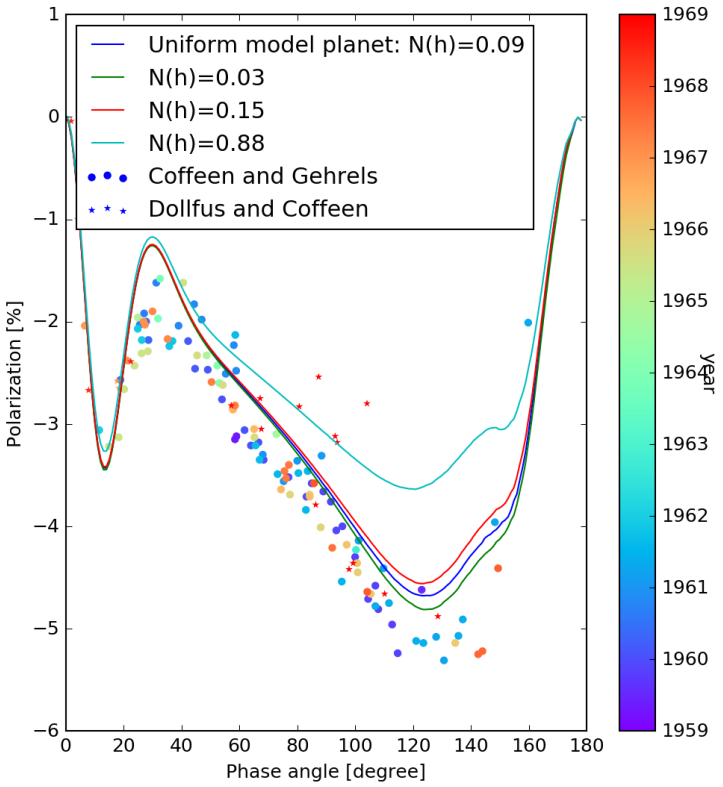

Fig. 33: Varying the column number density in *particles* μm^{-2} of the polar haze for λ=0.990μm (set 14). Input: see Figure 27 but with n_r(cloud)=1.43, n_r(haze)=1.43.

Some research claims that the haze particles are actually larger than r_{eff} = 0.25μm. They make use of a unimodal population with particles between 0.30μm and 0.79μm, depending on the altitude. Or a bimodel population with small (~0.12μm) and larger particles (~0.82μm) (Wilquet et al. 2009). Wilquet et al. (2009) did their research for high latitudes only. Five years later, Luginin et al. (2016) continued this work and found larger haze particles in the mid-latitudes as well. In Appendix A it can be seen that increasing the particle sizes for the haze over the entire planet does not improve the fit but from Figure 34 it can be seen that larger haze particles around the poles do improve the fit to the historical data for the larger phase angles. It would not be surprising that if the polar regions have different ambient circumstances, maybe the particles can grow larger because of a different environment.

Changing the haze top pressure in the polar regions has no observable effect on the fit. In Appendix E three figures (Figure E.12, E.13 and E.14) who support this are added.

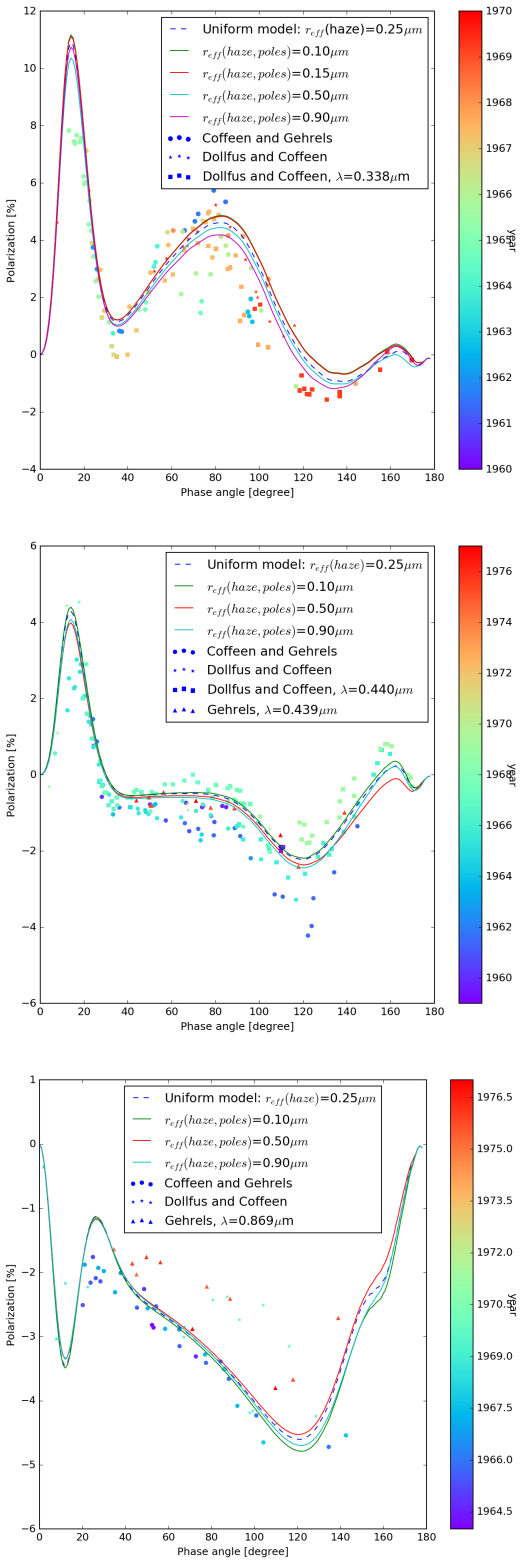

Fig. 34: Varying the effective radius of the haze particles around the poles for: *Top*: λ=0.340μm, *Middle*: λ=0.445μm and *Bottom*: λ=0.875μm. Input: r_{eff}(cloud)=1.05μm, v_{eff}(cloud)=0.07, r_{eff}(haze, equatorial)=0.25μm, v_{eff}(haze)=0.18, N(cloud)=6.5 particles μm^{-2}, N(haze)=0.09 particles μm^{-2} and n_r(cloud)=1.466, n_r(haze)=1.466 for λ=0.340μm and n_r(cloud)=1.45, n_r(haze)=1.45 for λ=0.445μm and n_r(cloud)=1.43, n_r(haze)=1.43 for λ=0.875μm.

6.5.2. Cloud properties

For the cloud properties, we performed the same investigation with varying the properties in the polar region as for the haze. The effects will be discussed below.

As expected, making the cloud extremely thin has a significant effect on the polarization in the shorter wavelengths, see Figure 35. Applying this to the Venus data delivers not enough proof for a different optical thickness of the cloud around the poles. On top of that, as long as the cloud is optically thick (so only changes a little), it will be very hard to distinguish the differences in the disk-integrated polarization data.

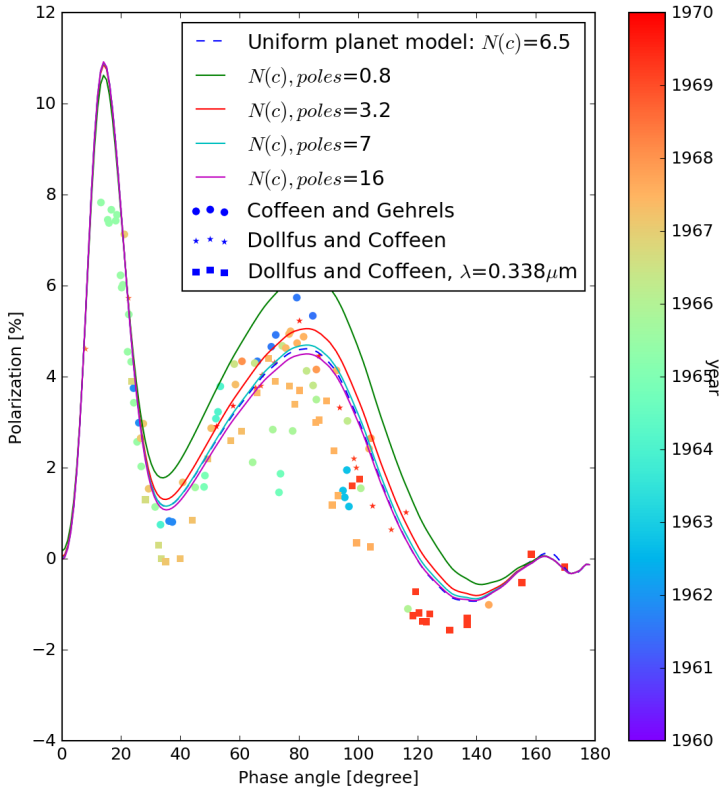

Fig. 35: Varying the column number density in particles μm^{-2} of the cloud in the polar regions for λ=0.340μm and λ=0.338μm (set 1). Input: r_{eff}(cloud)=1.05μm, v_{eff}(cloud)=0.07, r_{eff}(haze)=0.25μm, v_{eff}(haze)=0.18, N(cloud, equatorial)=6.5 particles μm^{-2}, N(haze)=0.09 particles μm^{-2} and n_r(cloud)=1.466, n_r(haze)=1.466.

Varying the cloud top pressure in the polar region has more effect on the disk-integrated polarization data than varying the optical thickness of the cloud. Decreasing the pressure improves the fit for the larger phase angles, see Figure 36. For the longer wavelengths, the effect of this pressure change is minimal, see Figure 37 and Appendix E.7. A decreasing cloud top pressure means that the cloud is physically thicker and the haze is physically thinner. For 20 *mb* the cloud extends up to 70 *km*, if this is decreased to 10 *mb*, the cloud would extend to roughly 80 *km* altitude.

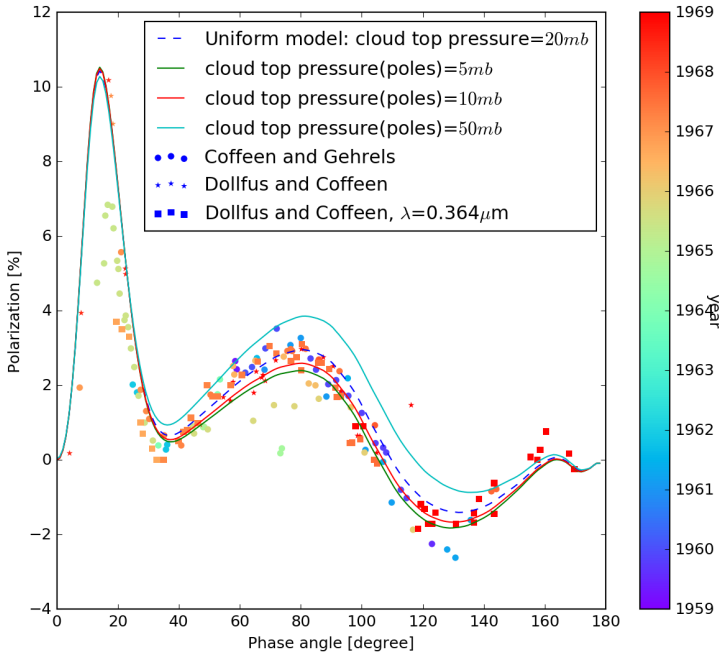

Fig. 36: Varying the cloud top pressure in the polar regions for $\lambda = 0.365\mu m$ and $\lambda = 0.364\mu m$ (set 2). Input:see Figure 35 but with N(cloud, equatorial)=N(cloud), n_r(cloud)=1.46 and n_r(haze)=1.46.

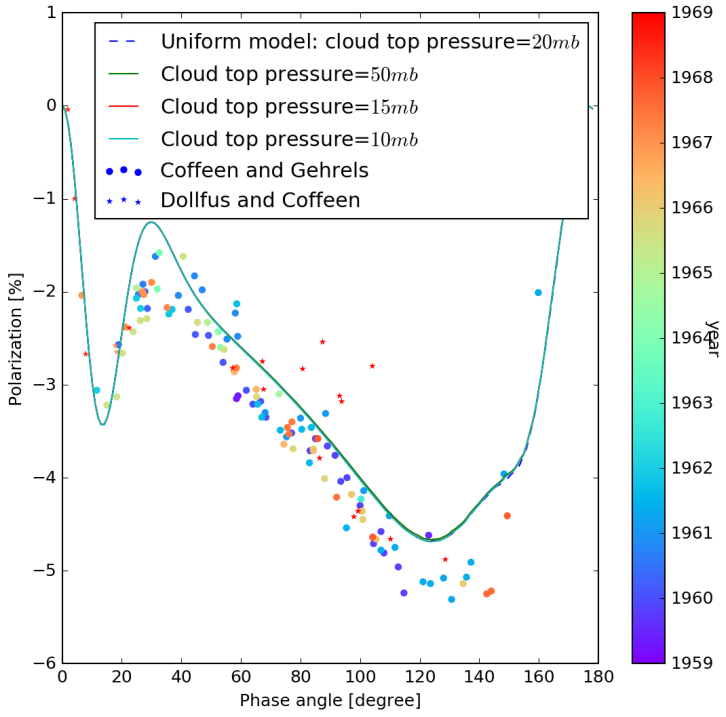

Fig. 37: Varying the cloud top pressure in the polar regions for $\lambda = 0.990\mu m$ (set 14). Input:see Figure 35 but with N(cloud, equatorial)=N(cloud), n_r(cloud)=1.43 and n_r(haze)=1.43.

In Figure 38 and Appendix E.6 it can be seen that varying the effective radius of the cloud particles in the polar regions between $0.85\mu m$ and $1.25\mu m$ hardly influences the polarization curves. Applying more extreme values ($0.2\mu m$ to $3.05\mu m$) does not improve the fit (see Figure 39 and Appendix E.6. So, the historical polarization data does not show any proof for differently sized cloud particles in the polar regions.

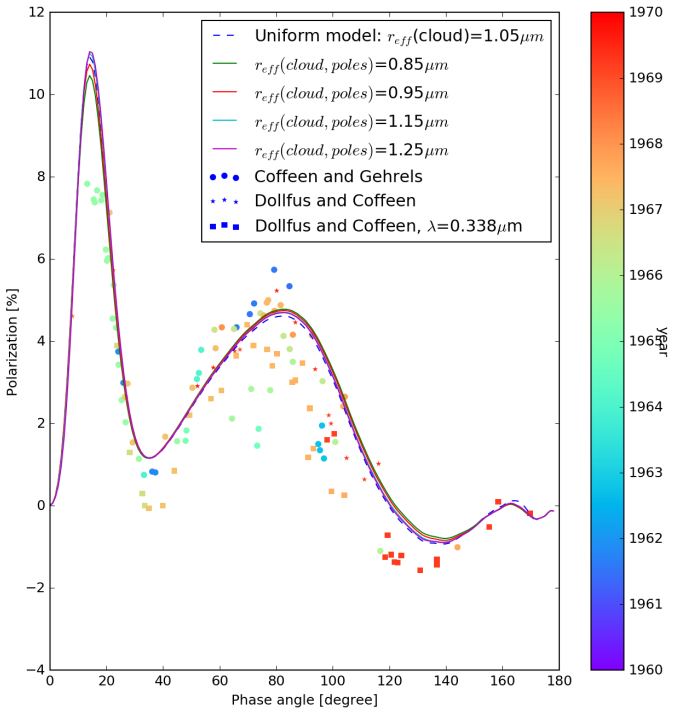

Fig. 38: Varying the effective radius of the cloud in the polar regions for λ=0.340μm and 0.338μm. Input:see Figure 35 but with N(cloud, equatorial)=N(cloud), r_{eff}(cloud, equatorial)=1.05μm, n_r(cloud)=1.466 and n_r(haze)=1.466.

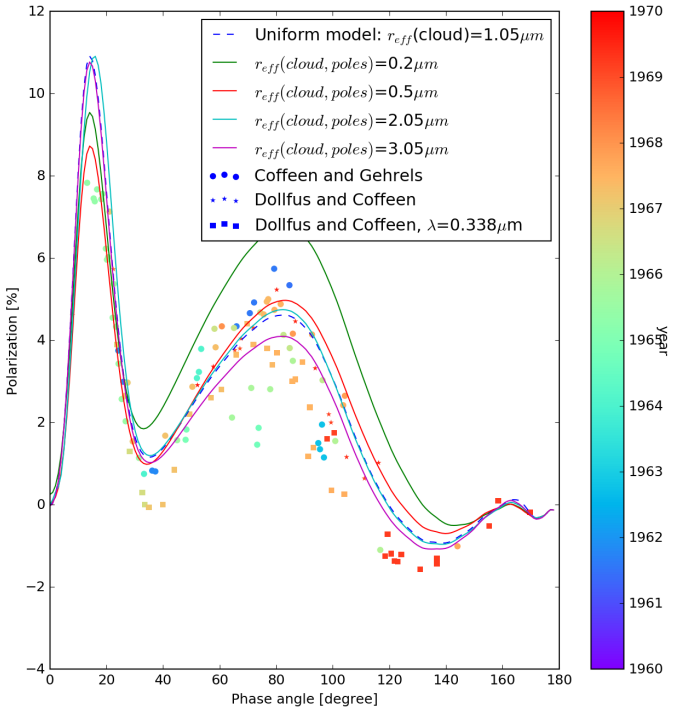

Fig. 39: Varying the effective radius of the cloud in the polar regions for λ=0.340μm and 0.338μm with more extreme values than Figure 38. Input:see Figure 35 but with N(cloud, equatorial)=N(cloud), r_{eff}(cloud, equatorial)=1.05μm n_r(cloud)=1.466 and n_r(haze)=1.466.

6.5.3. Conclusions on the polar cap region

An important outcome of this research is that it does not contribute to the statement made by Kawabata (1981) and Sato et al. (1996) that the haze is optically thicker around the poles. Sato et al. (1996) made use of local observations only. We did not find proof for this optically thicker haze but we did found that it would be possible to detect different optical thicknesses for the haze around the poles using disk-integrated data, especially when looking at the near-infrared wavelength region. Further, it is also possible to observe changes in: the effective radius of the cloud and haze particles; the refractive index of the cloud particles; the cloud top pressure; and in the optical thickness of the clouds. But one should note that the optical thickness of the clouds can only be distinguished using the UV-wavelengths. It is not possible to observe changes in the refractive index of the haze particles at the poles.

For the application to Venus it was found that adding larger particles to the haze layer and decreasing the cloud top pressure both improved the fit with the historical data. These two actually go hand in hand. Extending the cloud layer means more larger particles in higher altitudes which corresponds to adding larger particles to the haze layer. So it is likely that there exist more larger particles at higher altitudes at the Venus poles. If there are changes in any of the other cloud or haze properties, they are not apparent from the available Venus disk-integrated polarization data.

6.6. Subsolar haze

As discussed before (subsubsection 6.4.3), it could be possible that due to Venus's subsolar point the cloud or haze properties are different there. It is expected that the temperature above the clouds is higher at the subsolar point due to the constant heating. The clouds itself, on the other hand, move very rapidly. This heating could affect the haze particle properties. Here, we vary the effective radius of the haze particles, the refractive index of the haze particles and the optical thickness of the haze around the subsolar point. The extent in degrees of the subsolar cloud with respect to the subsolar point, σ_c, is chosen as 35°.

Changing the effective radius of the haze particles has an opposite effect for the smaller wavelengths compared to the near-infrared wavelengths. At λ=0.340μm, increasing the effective radius of the haze particles seems to improve the fit in the phase angle range 100°- 140° (Figure 40(a)). While it does not improve the fit at λ=0.950μm (Figure 40(b)). Therefore, it is not likely that the haze particles have different sizes around the subsolar point.

The optical thickness or the column number density of the haze is expected to be influenced by heating of the subsolar point (Titov et al. 2018). In Figure 41, it can be seen that the fit improves for the larger phase angles when the column number density of the haze is decreased around the subsolar point. This would mean that due to the local heating, the haze partly evaporates or the formation of the haze is influenced causing the haze formation to decrease. But at other points,

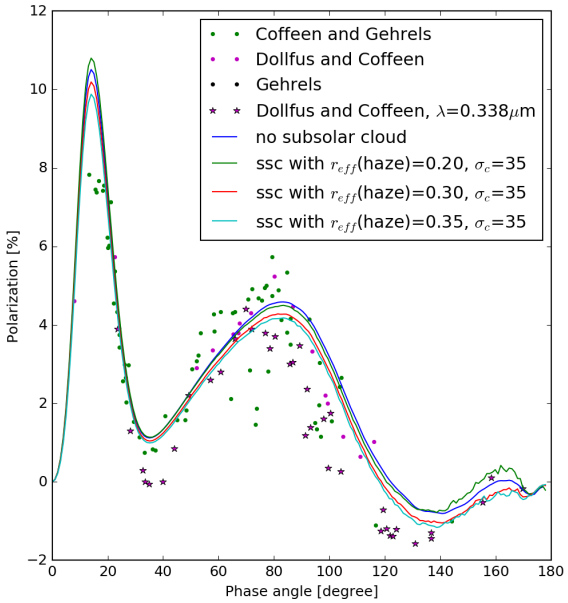

(a) λ=0.34μm and 0.338μm. Input: , n_r(cloud)=1.466, n_r(haze)=1.466.

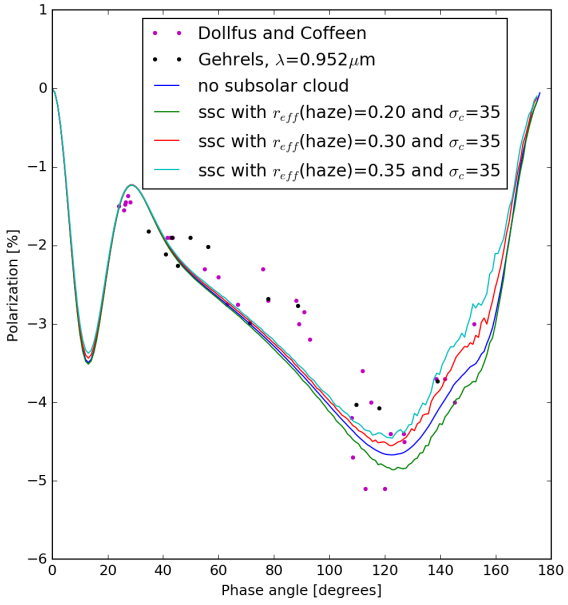

(b) λ=0.95μm and 0.952μm. Input: , n_r(cloud)=1.43, n_r(haze)=1.43.

Fig. 40: Subsolar haze (ssh) with various values for the effective radius. Input: r_{eff}(cloud)=1.05μm, r_{eff}(cloud, subsolar point)=variable, v_{eff}(cloud)=0.07, r_{eff}(haze)=0.25μm, v_{eff}(haze)=0.18, N(cloud)=6.5 particles μm^{-2}, N(haze)=0.09 particles μm^{-2}

such as the phase angle region between 120° and 140° (for λ=0.340μm) this improvement of the fit is not the case. Therefore this evidence is not convincing and more research is needed.

The last thing to change is the refractive index of the haze particles around the subsolar point. We, however, do not find a specific refractive index that improves the fit for every wavelength (see Figure 42), and therefore we cannot conclude that the particles have different refractive indices at the subsolar point.

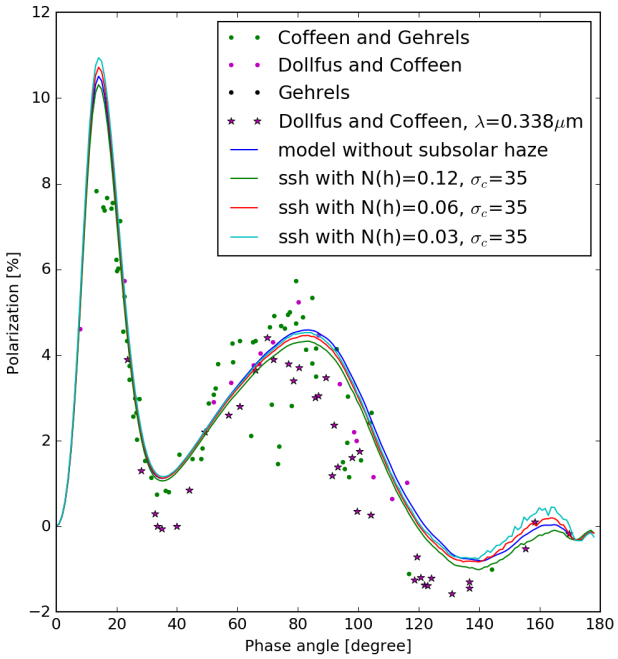

(a) $\lambda = 0.34\mu m$. Input: n_r(cloud)=1.466 and n_r(haze)=1.466

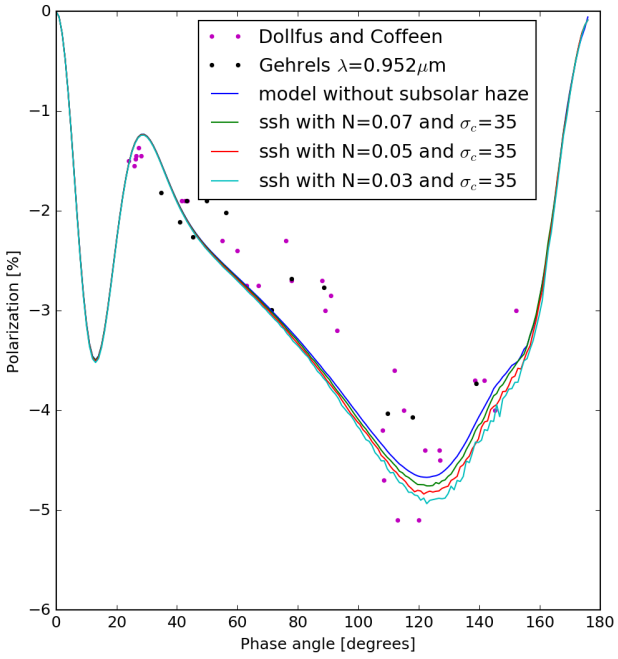

(b) $\lambda = 0.95\mu m$. Input: n_r(cloud)=1.43 and n_r(haze)=1.43

Fig. 41: Subsolar haze with various value for the column number density in *particles* μm^{-2}. Input: see Figure 40 but with r_{eff}(cloud, subsolar point)=variable = r_{eff}(cloud) and N(haze, subsolar point)=variable.

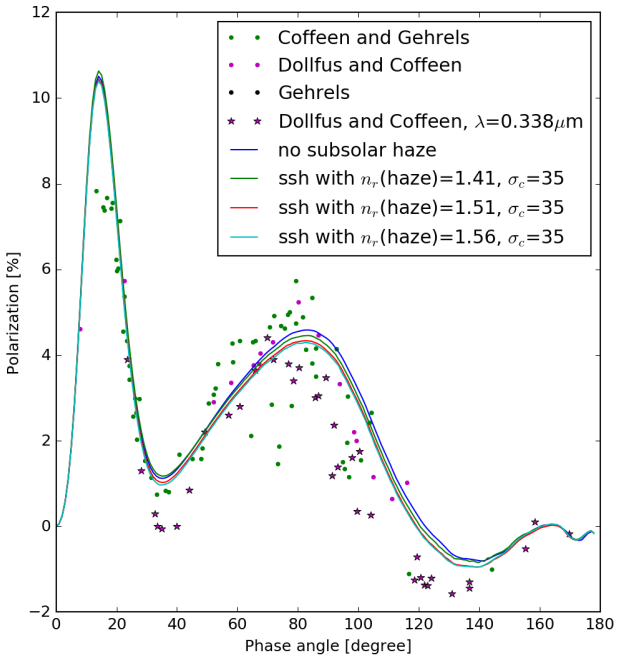

(a) $\lambda = 0.34\mu m$. Input: n_r(cloud)=1.466 and n_r(haze, non subsolar haze)=1.466

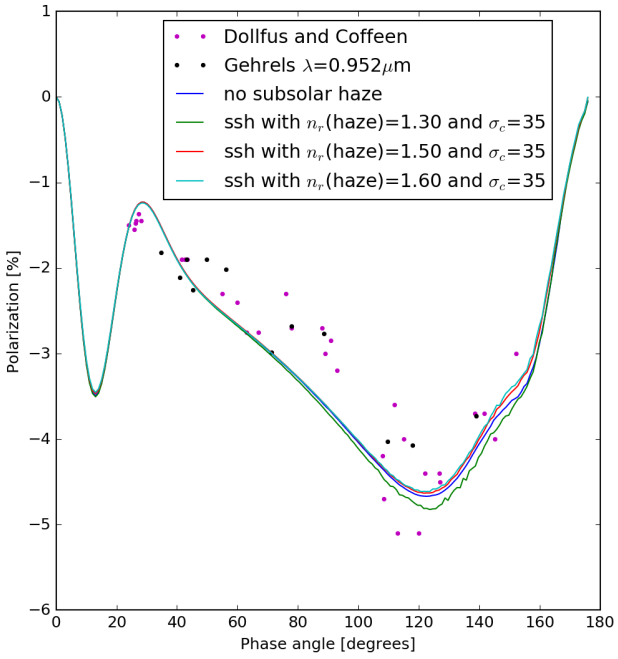

(b) $\lambda = 0.95\mu m$. Input: n_r(cloud)=1.43 and n_r(haze, non subsolar point)=1.43

Fig. 42: Subsolar haze with various values for the refractive index. Input: see Figure 40 but with r_{eff}(cloud, subsolar point)=variable = r_{eff}(cloud) and n_r(haze, subsolar point)=variable.

6.7. Time variability

It is interesting to investigate the time variability in more detail. For this we will only look at λ=0.445μm and 0.875μm since these wavelengths are the only wavelengths with clear time variations.

A problem that arises when analysing the time variability in more detail is the definition of "lower", "higher" and "normal" polarization. For the general research a curve was fitted through the middle of the data, not taking into account time changes. This average fit will be called the "normal" curve. This average fit is, however, not very reliably since the datapoints are not equally spread over time. The observations that are clearly above this curve be called the "higher" polarization and the data observations below will be called the "lower" polarization curve. For λ=0.455μm we see a spread around 40° to 120° phase angle. Looking at the figures of different optical thicknesses of the haze tells us that changes in this parameter do not explain the higher polarization. From the figures with different properties around the poles, it can be seen that changes in the cloud top pressure over the whole planet could explain the higher polarization curve. This is modeled with the help of numerical simulations, see Figure 43. This model gives a fit for the curves with higher and lower polarization by increasing and decreasing the cloud top pressure at the poles. Unfortunately, this change in cloud top pressure around the poles can not be further investigated since the effects of the cloud top pressure are only very small for λ = 0.875μm, see Figure 44.

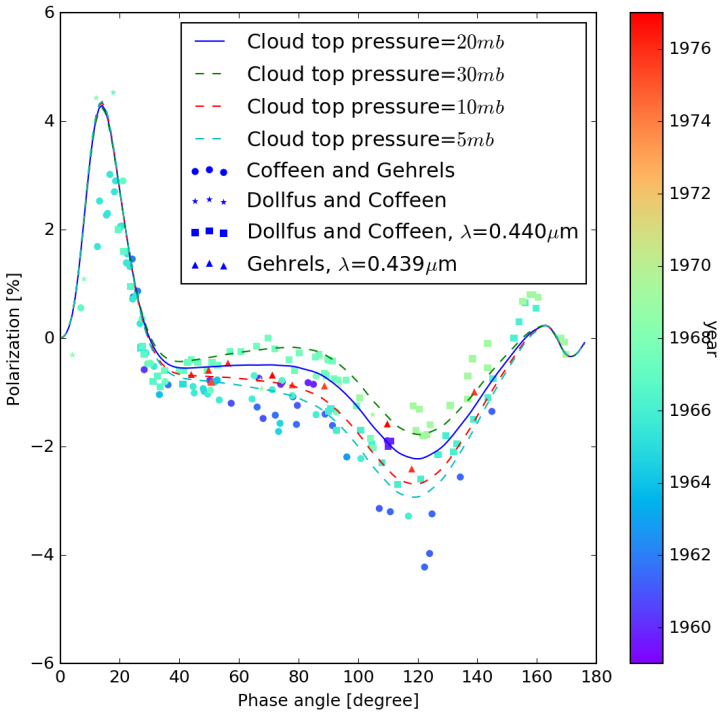

Fig. 43: Changing the cloud top pressure for λ=0.445μm, 0.440μm and 0.439μm in order to investigate the possibility of variability in time. Input:see Figure 35 but N(cloud, equatorial)=N(cloud), n_r(cloud)=1.45 and n_r(haze)=1.45.

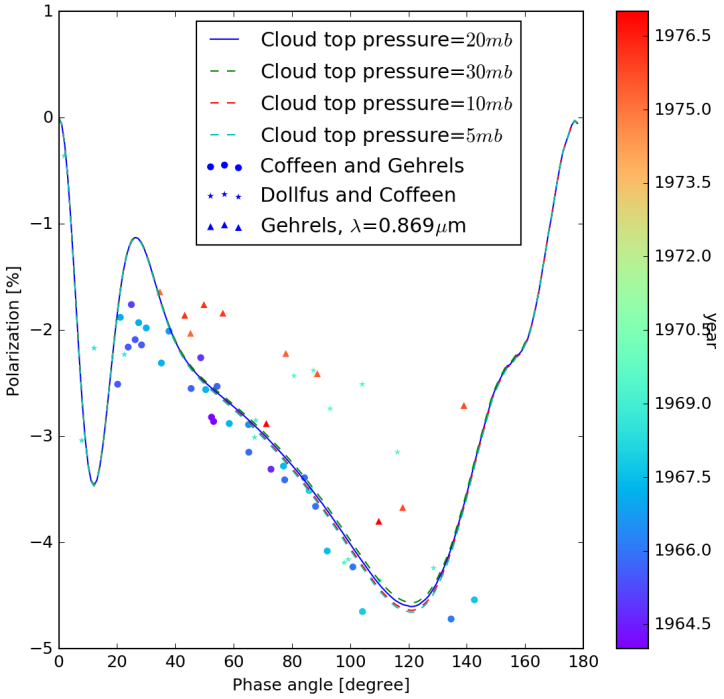

Fig. 44: Changing the cloud top pressure for λ=0.875μm and 0.869μm in order to investigate the possibility of variability in time. Input:see Figure 35 but N(cloud, equatorial)=N(cloud), n_r(cloud)=1.43 and n_r(haze)=1.43

7. Discussion on exoplanets

The knowledge obtained above can be applied to exoplanet research. Therefore this section starts with a comparison between flux and polarization measurements to see which one is favorable. Finally, a simple model to characterize exoplanets is shortly discussed.

In section 2 it was already mentioned that for the interpretation of polarization measurements it is not necessary to know the distance to the observed planet and the radius of the observed planet. The flux data that is obtained with PyMieDAP is normalized with respect to the planet's geometric albedo. This geometric albedo is dependent on the type of atmosphere and usually not known for an exoplanet.

For this section it is very important to keep in mind that it is based on the assumption that all that will be discussed is observable, because at this point it is not possible to do these kind of observations for exoplanets. So one should interpret the results as if it is possible to do the observations. It falls out of the scope of this research to do a complete trade off for future telescope instruments.

7.1. Comparison to flux

Since (exo)planets can be subjected to flux and polarization measurements, it is interesting to compare them. With this comparison discuss the advantages and disadvantages of both. Figures that support the need of possible future missions such as the LUVOIR (concept) telescope, which will have a polarimetry instrument, will be presented. To keep the reading concise not all figures will

be displayed, more figures can be found in Appendix F.

We start with changing the refractive index of the clouds particles. Steps of 0.01 can clearly be distinguished in the polarization curves, see the green, red and lightblue lines in Figure 45(right). The figures for $\lambda = 0.340\mu m$, $0.445\mu m$, $0.650\mu m$ and $0.840\mu m$ can be found in Appendix F.1. In the curves representing the flux, a small difference in the curves is visible in the smaller phase angle region, see Figure 45(left). To make this distinction in the small phase angles would in reality be very challenging because when observing the small phase angles, the planet is very close to its star, see Figure 1. It is often problematic to observe so close to the star and very dependent on the design of the telescope and instrument. Thereby, the phase angle at which we can observe the (exo)planet depends on the orbital inclination of the (exo)planet: $90-i \leq \alpha \leq 90+i$ (where $i = 90°$ is edge-on) (Pearce 2012). Meaning that for some exoplanets it would not be possible to measure the small phase angles.

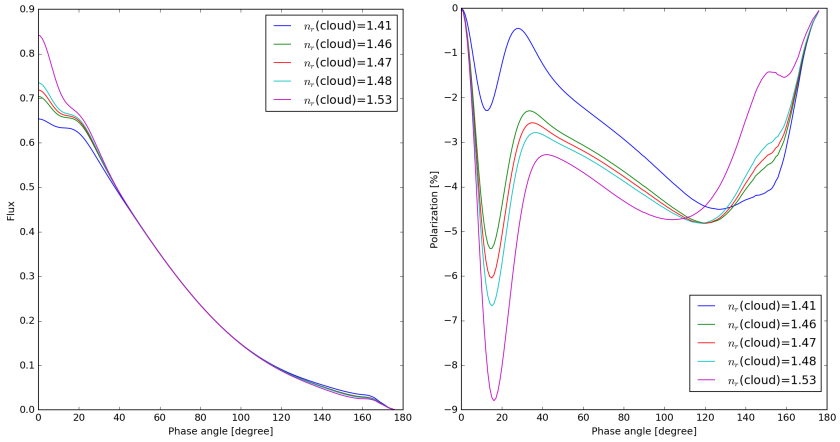

Fig. 45: Varying the refractive index of the clouds for $\lambda = 0.990\mu m$. *Left* shows the flux curves and *right* the corresponding polarization curves. Input: r_{eff}(cloud)=1.05μm, v_{eff}(cloud)=0.07, r_{eff}(haze)=0.25μm, v_{eff}(haze)=0.18, N(cloud)=6.5 particles μm^{-2}, N(haze)= 0.09 particles μm^{-2} and n_r(haze)=1.43.

Varying the optical thickness of the clouds does influence the flux curves more than varying the refractive index of the cloud particles (Figure 46(left)). Meaning that it is possible to determine how optical thick the cloud is with the help of flux measurements, but only if the geometric albedo of the planet is known. This determination is mainly restricted to determining if the cloud is optically thick or thin. With the help of precise polarization observations the optical thickness of the clouds can be determined with more precision (Figure 46(right)).

For the refractive index of the haze there is almost no difference in the flux curves while for the polarization curves is it possible to observe the differences, see Figure 47. Especially for the longer wavelengths (see Appendix F) the differences in flux curves are negligible. If this is combined with the figures for the optical thickness of the haze (Figure 48), it can be concluded that it is not pos-

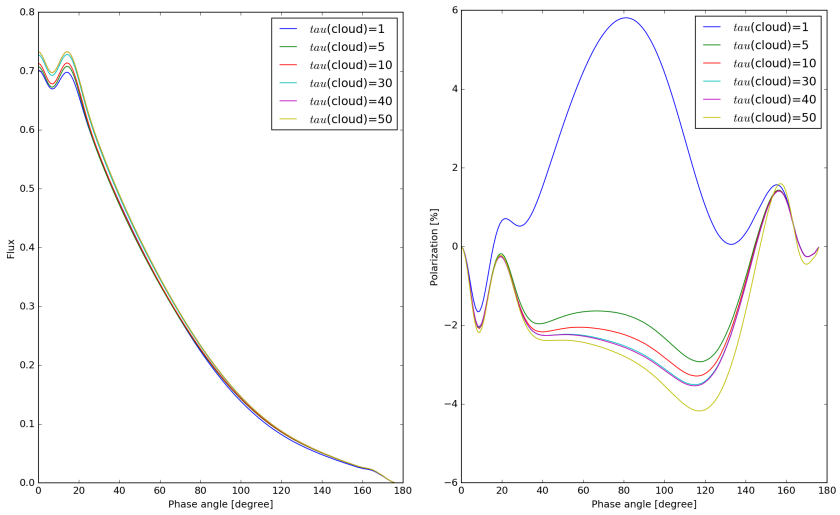

Fig. 46: Varying the optical thickness of the clouds for λ=0.650μm. *Left* shows the flux curves and *right* the corresponding polarization curves. Input: see Figure 45 but with n_r(cloud)=n_r(haze)=1.44.

sible to distinguish any properties of the haze for Venus-like exoplanets when only measuring the flux.

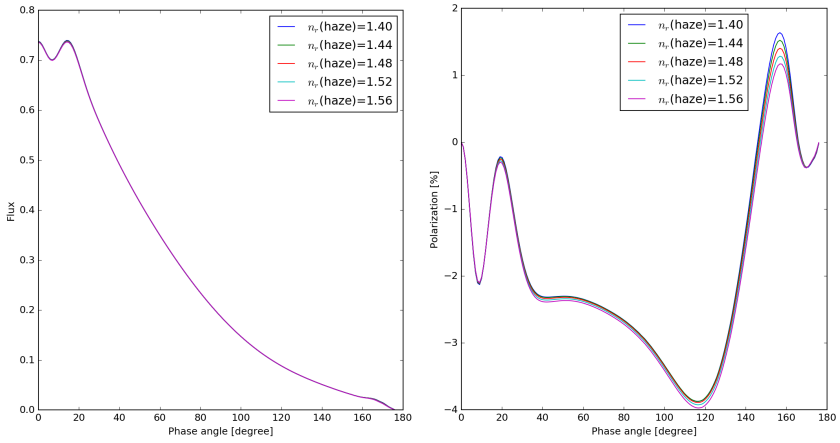

Fig. 47: Varying the refractive index of the haze for λ=0.650μm. *Left* shows the flux curves and *right* the corresponding polarization curves. Input: see Figure 45 but with n_r(cloud)=1.44.

Concluding, when obtaining the flux curves for (exo)planets it is possible to find the optical thickness of the cloud and, if you are able to measure the small phase angles, the refractive index of the cloud assuming the geometric albedo is known. But finding the haze properties (or identifying a haze layer) will be very challenging. For polarization curves it is possible to obtain information on both cloud and hazes, if you are able to observe accurately.

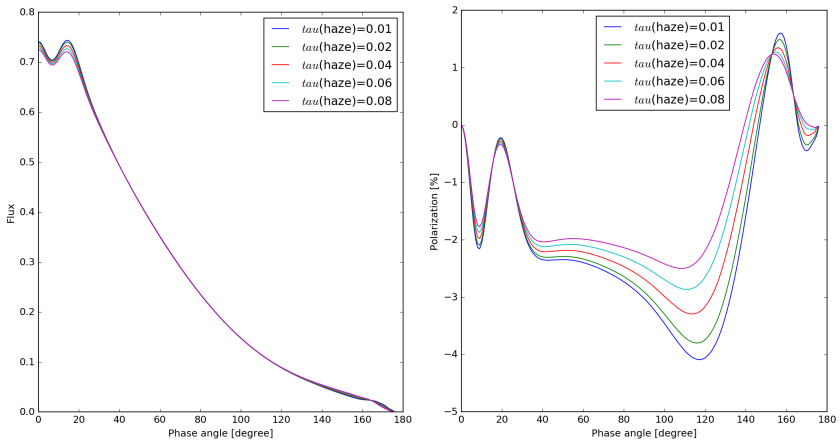

Fig. 48: Varying the optical thickness of the haze for λ=0.650μm. *Left* shows the flux curves and *right* the corresponding polarization curves. Input: see Figure 45 but with n_r(cloud)=n_r(haze)=1.44.

7.2. Other cloud particles

To extend this research a bit, a simple planet model with different refractive indices of the cloud is investigated. For this simple model a homogeneous atmosphere with an optically thick cloud is assumed. Since the influence of a thin haze layer is limited in the flux, the optical thickness of the haze is set to zero. The gas used in this atmosphere model is CO_2 gas, just like on Venus. Then, for particles of r_{eff} = 1.05μm, the refractive index of the particles is changed. The refractive indices are chosen in such a way that they correspond to water (H_2O), 75% sulfuric acid and 95.6% sulfuric acid. The refractive indices for water were derived from Figure 13 in Hansen & Hovenier (1974) (n_r=1.35 for λ=0.365μm, 1.34 for 0.550μm and 1.33 for 0.990μm) and the refractive indices for 95.6% sulfuric acid were obtained from the tables in the paper by Palmer & Williams (1975) (n_r=1.459 for λ=0.365μm, 1.434 for 0.550μm and 1.427 for 0.990μm).

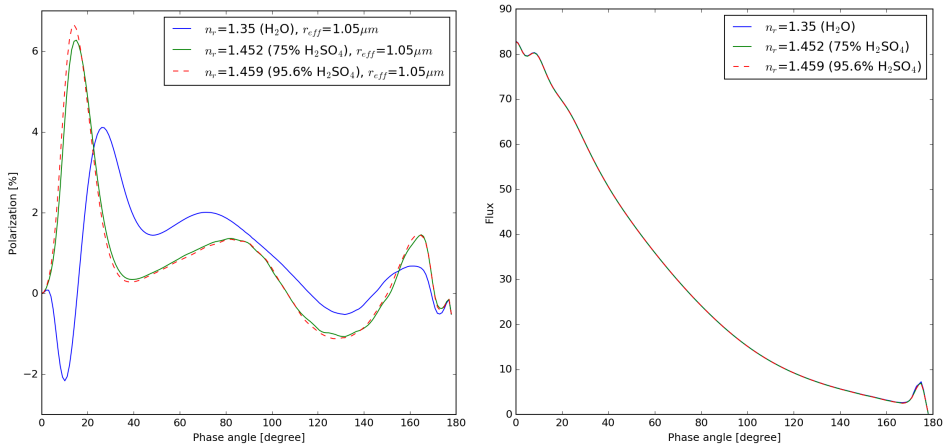

Fig. 49: Polarization (*left*) and flux (*right*) curves for different refractive indices of the cloud particles for λ=0.365μm with N=8 *particles* μm^{-2}.

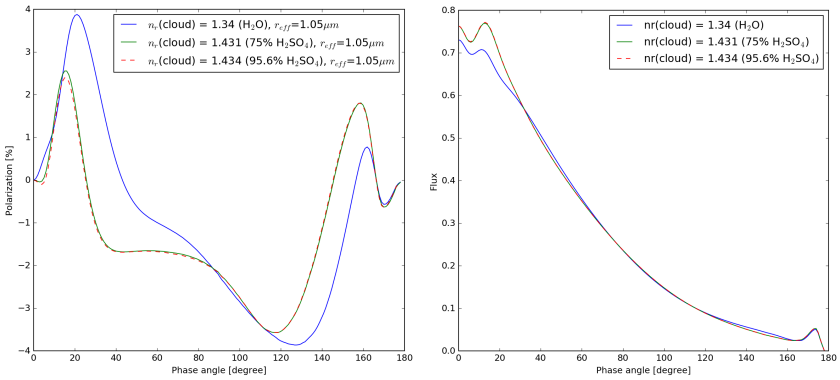

Fig. 50: Polarization (*left*) and flux (*right*) curves for different refractive indices of the cloud particles for λ=0.550μm with N=8 *particles* μm^{-2}.

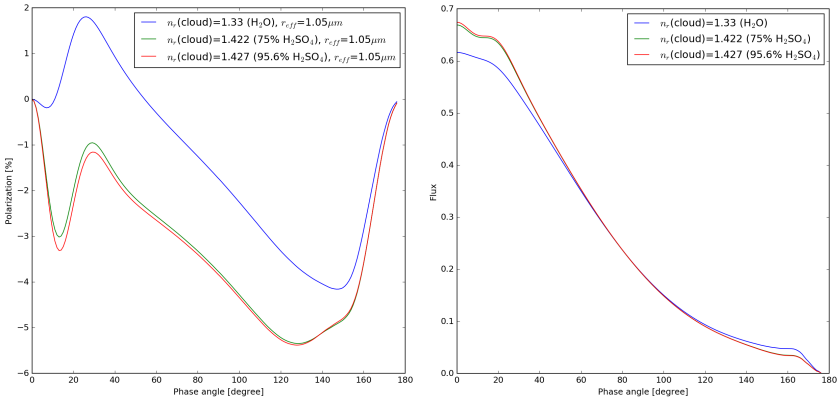

Fig. 51: Polarization (*left*) and flux (*right*) curves for different refractive indices of the cloud particles for λ=0.990μm with N=8 *particles* μm^{-2}.

First we look at Figures 49, 50 and 51. From these figure we can see that sulfuric acid and water cloud particles seem to be distinguishable from disk-integrated polarization data. Smaller changes such as the percentage sulfuric acid, are harder to distinguish. In order to distinguish the percentage sulfuric acid you need to involve near-infrared wavelengths in the observations and observe with high precision in the small phase angles.

The Earth atmosphere contains larger particles as well, therefore larger particles of the order 3 and 4 micron are added as well (Figure 52). It can be seen that these larger cloud particles show more characteristics and it will therefore be easier to recognize them. Especially for the smaller phase angles, the characteristics of water particles become more clear.

If the particles become smaller with respect to the wavelength, the curves start to behave like Rayleigh scattering, see Figure 53. But the difference between water and sulfuric acid clouds stays clearly visible.

For the flux curves (Figures 49, 50, 51), the same holds as for the flux curves discussed before. There are almost no differences in the mid phase angles, while it is easiest to observe there. Not

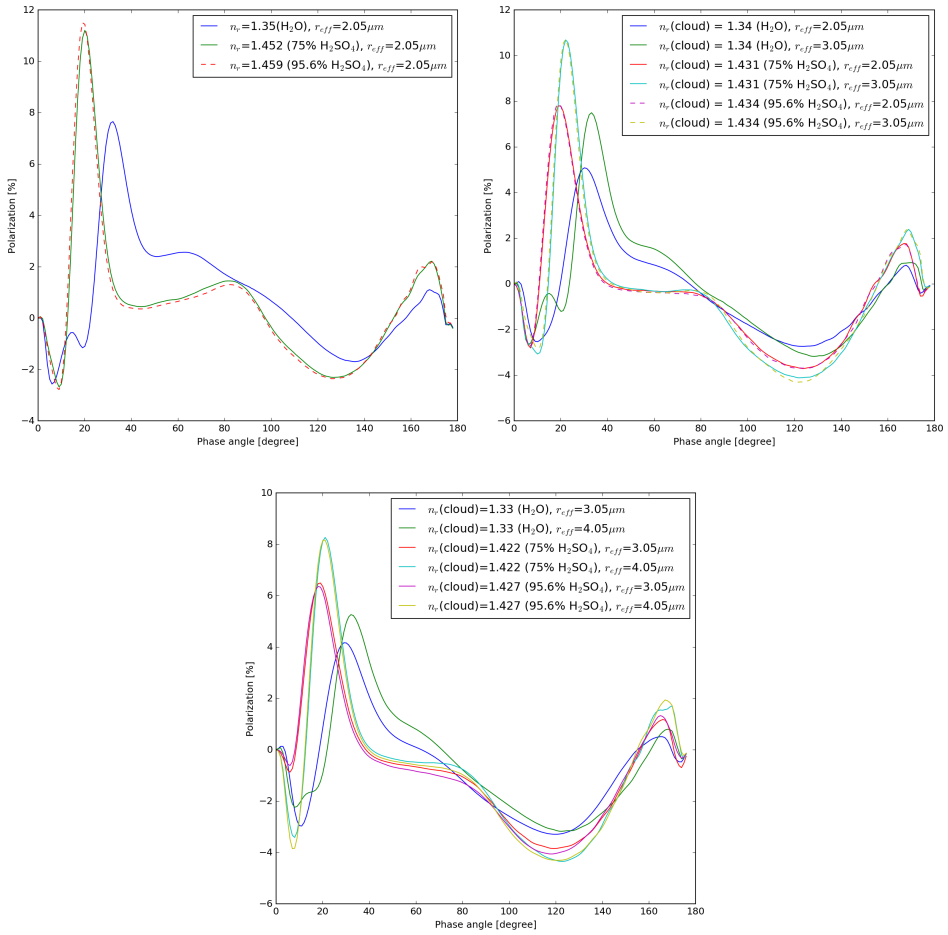

Fig. 52: Different refractive indices and effective radii for the cloud particles for $\lambda = 0.365\mu m$ (*left*), $0.550\mu m$ (*right*) and $0.990\mu m$ (*bottom*).

knowing the geometric albedo of the (exo)planet, will make it even harder, possibly impossible, to draw conclusions when using flux observations only.

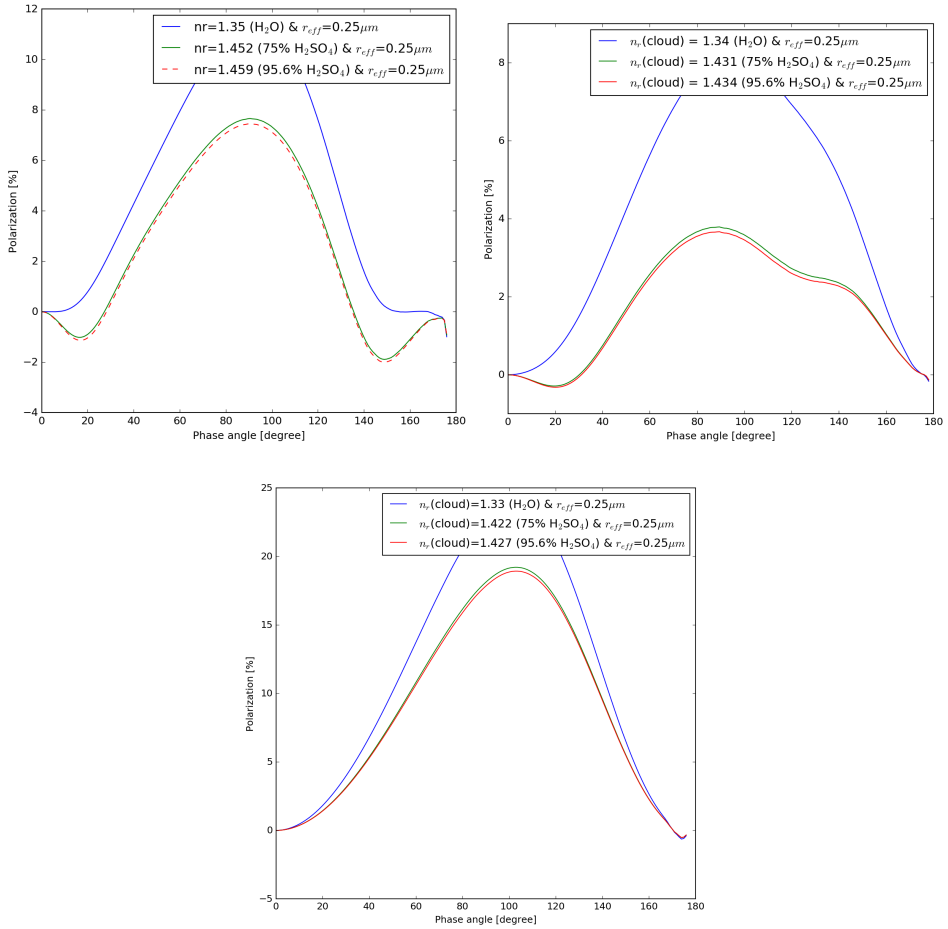

Fig. 53: Figure 52 with smaller effective radii for the cloud particles for $\lambda = 0.365\mu m$ (*left*), $0.550\mu m$ (*right*) and $0.990\mu m$ (*bottom*).

8. Discussion

During this research several assumptions are made. Some have already been discussed in section 5. The Venus atmosphere consists of multiple cloud layers but here we only worked with one thick cloud layer. Since the cloud layer of Venus is optically thick, everything under the cloud is assumed to not influence the polarization curves. Therefore the other lower cloud layers are not modeled separately. This might have a small effect on the final polarization curves.

The optimized value for the optical thickness of the haze which is used during this research ($\tau = 0.04$ for $\lambda = 0.340\mu m$) is lower than the values obtained by other studies (varying between 0.06 and 0.8 for $\lambda = 0.365\mu m$) (Sato et al. 1996), (Kawabata et al. 1980). This can be caused by the difference in type of data, they both used OCPP data. It can also be possible that the haze of Venus changes over longer periods of time and the haze really had a different optical thickness when OCCP measured.

Unfortunately it was not possible to find a perfect fit for all wavelengths and phase angles. The ones that will probably catch the readers eye are:

- for $\lambda = 0.340\mu m$: the numerical model is not steep enough to reach the minimum between $\alpha = 120°$ and $\alpha = 140°$;
- for $\lambda = 0.445\mu m$ and $\lambda = 0.550\mu m$: the numerical simulation does not touch the maximum polarization at $\alpha = 160°$;
- for $\lambda = 0.685\mu m$: the numerical simulation curve is higher than the minimum point of polarization for $\alpha = 120°$;
- for $\lambda = 0.99\mu m$: the computed curve lays above the data instead of on the data.

It was possible to optimize the specific cases but this always resulted in a worse fit for the other wavelengths. So it is possible to optimize the fits per wavelength further if you look at each wavelength separately but in the end, you would like to have one fitting model for all wavelengths.

Upward of $\lambda = 0.650\mu m$, there are no observations for phase angles larger than $\alpha = 150°$. This is therefore also a very interesting phase angle range for future studies. According to the numerical simulations the polarization curve goes up a lot in those larger phase angles. Since there are no measurements in that region it is hard to check if this is really the case. The optimisation for the longer wavelengths is therefore based on the available data in the smaller phase angle region. If the polarization data in the longer wavelength region turns out to behave completely different in the higher phase angles than expected based on the numerical simulations, this could seriously influence the outcome of this research.

9. Recommendations

- The twilight zone or terminator is the transitional region between the dayside and the nightside of a planet. PyMieDAP assumes a strict line between the day and night side of the planet. Since Venus has a thick atmosphere this transition between day and night might not be so strict. Scattered light still arrives at the "dark"side of the planet. This light can also contribute to the polarization, and therefore influence the disk-integrated data especially at intermediate phase angles. The PyMieDAP software is not able to apply the effect of the twilight zone to the models because it assumes a locally flat model atmosphere. It will be interesting for future research to investigate this effect of the Venus twilight zone using another code such as the Monte Carlo code written by Nino Hadžisejdić (Hadžisejdić 2020).
- For future polarization observations it is important to observe in a broad range of wavelengths: from the ultraviolet to the infrared. It is also favorable to measure at as many phase angles as possible. The measurements are preferably taken over different time periods: covering all wavelengths and phase angles every time period. It could be desired to test this on Venus first since it is possible to compare the results with in-situ measurements. But this will results in local measurements. In order to do this analysis of Venus, new disk-integrated measurements of Venus are needed. For these new observations it would be nice to also fill the gaps in the historical data such as the lack of observations for phase angles larger than $\alpha = 150^\circ$ for wavelengths upward $0.650\mu m$.
- For our research we assumed the cloud and haze properties of the north and south poles to be equal. This assumption may not hold, it will be worth investigating this.
- Looking back at Figure 1, it can be seen that for the same phase angle different sides of Venus can be observed. One side is the morning side (measurable in the evening from Earth) and the other side is the evening side (measurable in the morning from Earth). Since the morning and evening side can have different temperatures it is possible that the environments are also different. From the historical data used during this research the observation times (apart from the date) where most of the times not noted down so it was not possible to take into account the morning and night side of Venus. For future studies it would be interested to do this and to investigate whether there are differences.
- For future exoplanet research it is important that the measurements are made in a wide spectrum of wavelenghts. It is thereby important to measure for all the available phase angles. It should be recalled that it is not always possible to measure an exoplanet at all phase angles, since a planet's phase angle coverage depends on its orbital inclination angle i: $90-i \leq \alpha \leq 90+i$.

References

Bates, D. R. 1984, Planet. Space Sci., 32, 785

Beeson, S. & Mayer, J. 2008, Patterns of Light

Coffeen, D. L. & Gehrels, T. 1969, AJ, 74, 433

de Haan, J. F., Bosma, P. B., & Hovenier, J. W. 1987, A&A, 183, 371

Dollfus, A. & Coffeen, D. L. 1970, A&A, 8, 251

Gehrels, T., Gradie, J. C., Howes, M. L., & Vrba, F. J. 1979, AJ, 84, 671

Haberle, R. M., Clancy, R. T., Forget, F., Smith, M. D., & Zurek, R. W. 2017, The atmosphere and climate of Mars

Hadžisejdić, N. 2020, Master's thesis, Delft University of Technology, The Netherlands

Hansen, J. E. & Hovenier, J. W. 1974, Interpretation of the Polarization of Venus., 288–311

Hansen, J. E. & Travis, L. D. 1974, Space Sci. Rev., 16, 527

Jenkins, J. M., Steffes, P. G., Hinson, D. P., Twicken, J. D., & Tyler, G. L. 1994, Icarus, 110, 79

Kawabata, K. 1981, Moon and Planets, 24, 291

Kawabata, K., Coffeen, D. L., Hansen, J. E., et al. 1980, J. Geophys. Res., 85, 8129

Knollenberg, R., Travis, L., Tomasko, M., et al. 1980, J. Geophys. Res., 85, 8059

Lissauer, J. J. & de Pater, I. 2013, Fundamental Planetary Science

Luginin, M., Fedorova, A., Belyaev, D., et al. 2016, Icarus, 277, 154

Lyot, B. 1929, Annales de 1'Observatoire de Paris

Marcq, E., Lea Jessup, K., Baggio, L., et al. 2020, Icarus, 335, 113368

NASA. 2018, Venus, https://solarsystem.nasa.gov/planets/venus/in-depth/

NASA. 2019, LUVOIR Design, https://asd.gsfc.nasa.gov/luvoir/design/

Nozière, B. & Esteve, W. 2005, Geophys. Res. Lett., 32, L03812

Palmer, K. F. & Williams, D. 1975, Appl. Opt., 14, 208

Pätzold, M., Häusler, B., Bird, M. K., et al. 2007, Nature, 450, 657

Pearce, F. R. 2012, Contemporary Physics, 53, 380

Pérez-Hoyos, S., Sánchez-Lavega, A., García-Muñoz, A., et al. 2018, Journal of Geophysical Research (Planets), 123, 145

Pollack, J. B., Toon, O. B., Whitten, R. C., et al. 1980, J. Geophys. Res., 85, 8141

Rossi, L. 2016, PhD thesis, HAL, France

Rossi, L., Berzosa-Molina, J., & Stam, D. M. 2018, A&A, 616, A147

Rossi, L., Marcq, E., Montmessin, F., et al. 2015, Planet. Space Sci., 113, 159

Sato, M., Travis, L. D., & Kawabata, K. 1996, Icarus, 124, 569

Stam, D. M. 2008, A&A, 482, 989

Stam, D. M., Hovenier, J. W., & Waters, L. B. F. M. 2004, A&A, 428, 663

Titov, D. V., Ignatiev, N. I., McGouldrick, K., Wilquet, V., & Wilson, C. F. 2018, Space Sci. Rev., 214, 126

van de Hulst, H. C. 1957, Light Scattering by Small Particles

Wiktorowicz, S. & Stam, D. 2015, Exoplanets, 439 – 457

Wilquet, V., Fedorova, A., Montmessin, F., et al. 2009, Journal of Geophysical Research (Planets), 114, E00B42

Appendix A: Effective radius and variance

Appendix A.1: Cloud particles: effective radius

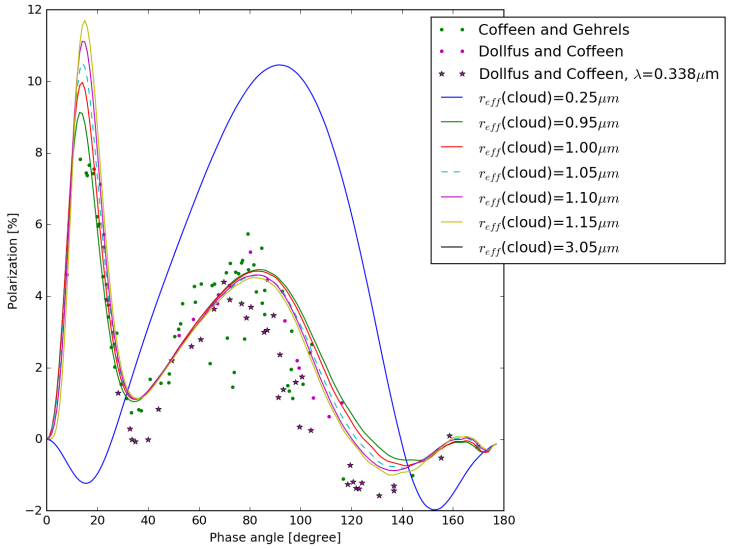

Fig. A.1: Effective radius of the cloud particles for λ=0.340μm. Input: v_{eff}(cloud)=0.07, r_{eff}(haze)=0.25μm, v_{eff}=0.18, N(cloud)=6.5 particles μm^{-2}, N(haze)=0.09 particles μm^{-2} and n_r(cloud)=n_r(haze)=1.47

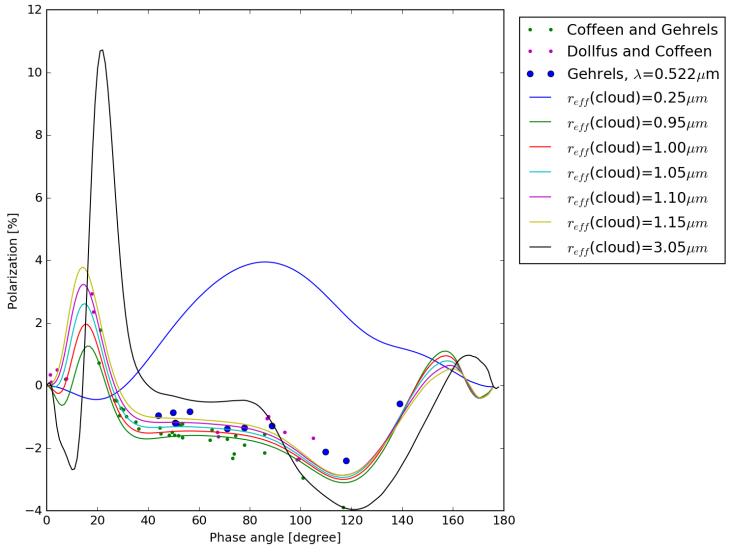

Fig. A.2: Effective radius of the cloud particles for λ=0.520μm. Input: see Figure A.1 but with n_r(cloud)=n_r(haze)=1.44

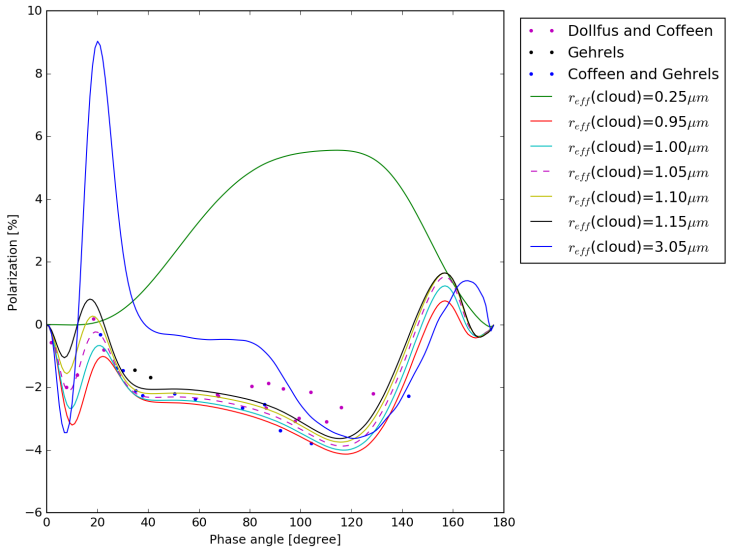

Fig. A.3: Effective radius of the cloud particles for λ=0.650μm. Input: see Figure A.1 but with n_r(cloud)=n_r(haze)=1.44

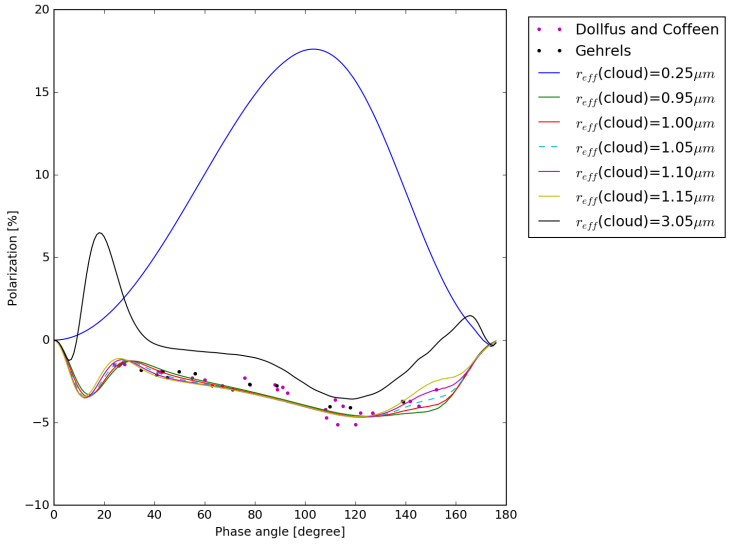

Fig. A.4: Effective radius of the cloud for λ=0.950μm. Input: see Figure A.1 but with n_r(cloud)=n_r(haze)=1.43

Appendix A.2: Cloud particles: effective variance

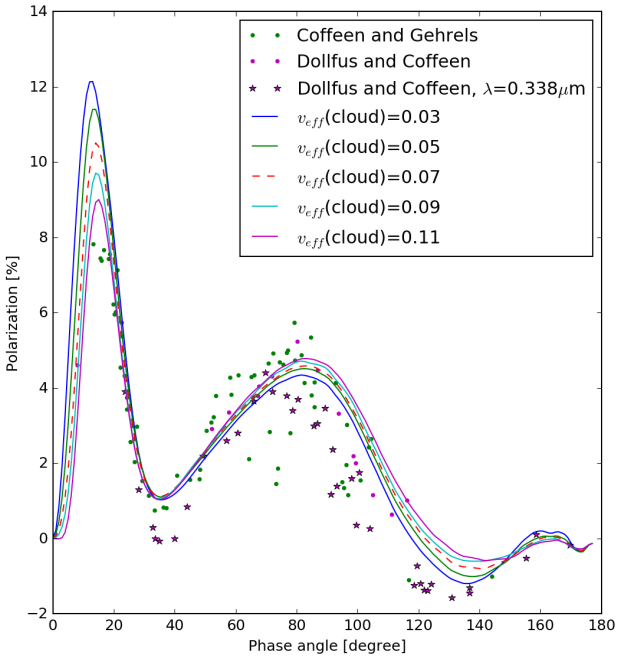

Fig. A.5: Effective variance of the cloud particles for λ=0.340μm. Input: r_{eff}(cloud)=1.05μm, r_{eff}(haze)=0.25μm, v_{eff}=0.18, N(cloud)=6.5 particles μm^{-2}, N(haze)=0.09 particles μm^{-2} and n_r(cloud)=n_r(haze)=1.47

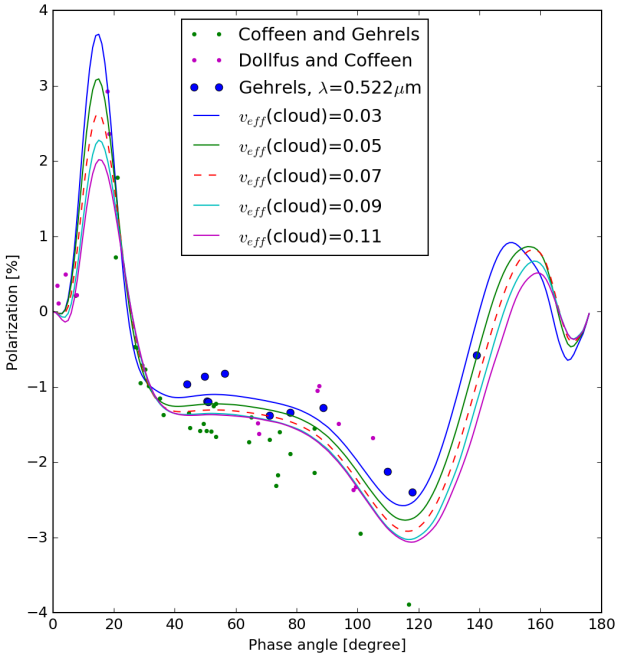

Fig. A.6: Effective variance of the cloud particles for λ = 0.520μm. Input: see Figure A.5 but with n_r(cloud)=n_r(haze)=1.44

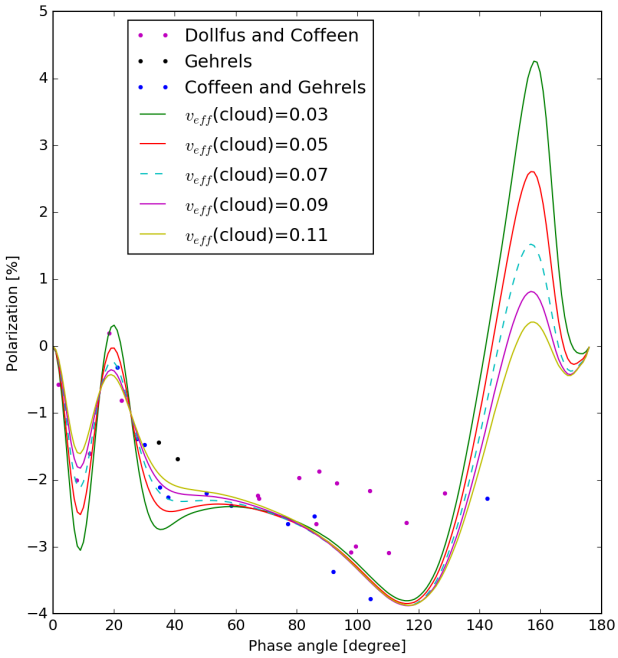

Fig. A.7: Effective variance of the cloud particles for $\lambda = 0.650\mu m$. Input: see Figure A.5 but with n_r(cloud)=n_r(haze)=1.44

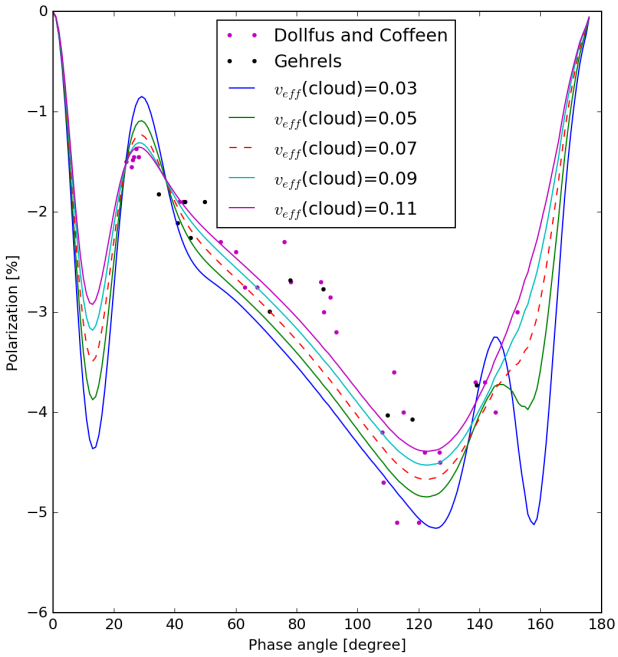

Fig. A.8: Effective variance of the cloud particles for $\lambda = 0.950\mu m$. Input: see Figure A.5 but with n_r(cloud)=n_r(haze)=1.43

Appendix A.3: Haze particles: effective radius

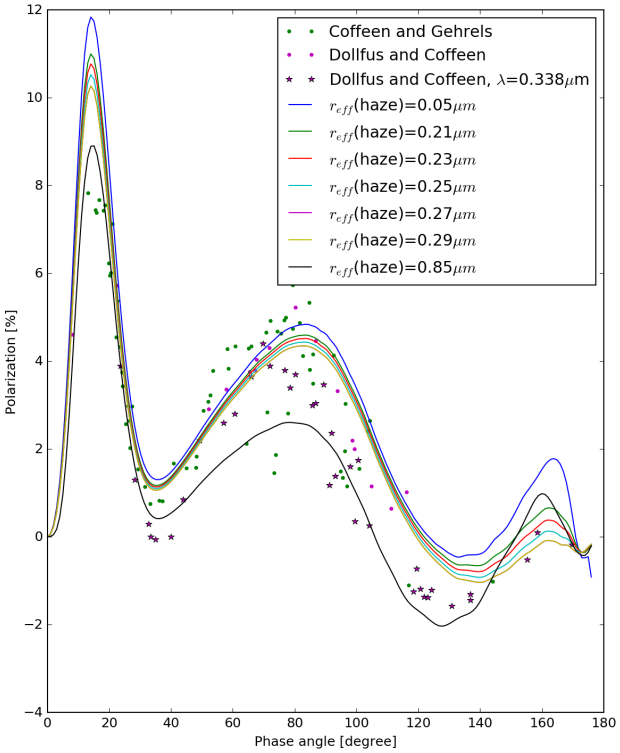

Fig. A.9: Effective radius of the haze particles for λ=0.340μm. Input: r_{eff}(cloud)=1.05μm, v_{eff}(cloud)=0.07, v_{eff}(haze)=0.18, N(cloud)=6.5 particles μm^{-2}, N(haze)=0.09 particles μm^{-2} and n_r(cloud)=n_r(haze)=1.47

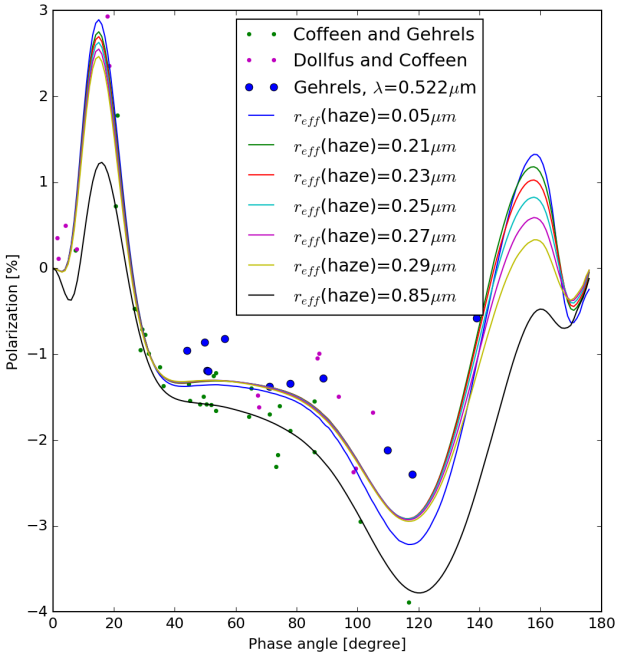

Fig. A.10: Effective radius of the haze for λ=0.520μm. Input: see Figure A.9 but with n_r(cloud)=n_r(haze)=1.44.

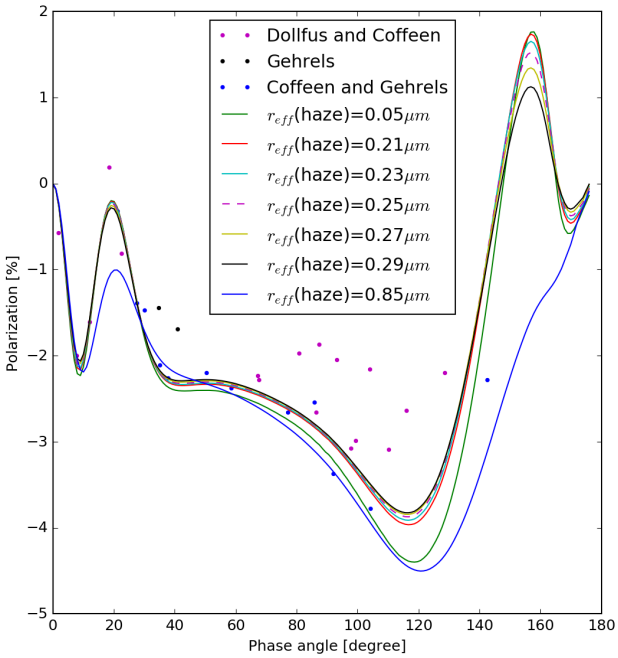

Fig. A.11: Effective radius of the haze particles for λ=0.650μm. Input: see Figure A.9 but with n_r(cloud)=n_r(haze)=1.44.

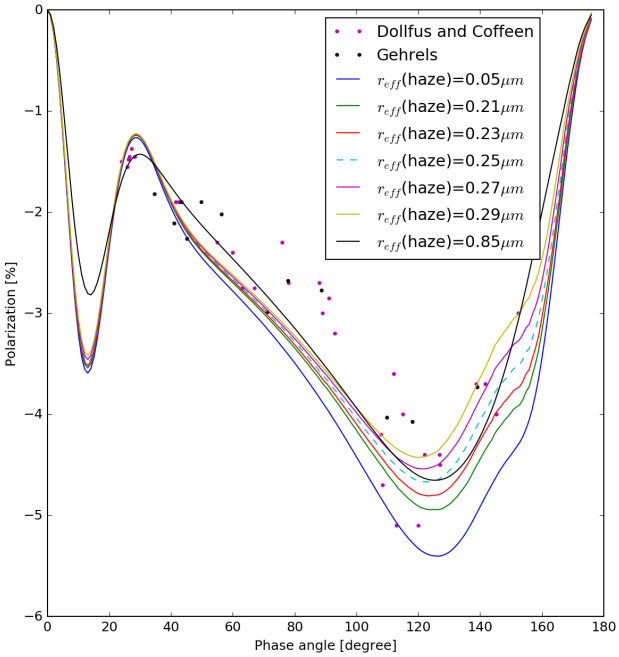

Fig. A.12: Effective radius of the haze for λ=0.950μm. Input: see Figure A.9 but with n_r(cloud)=n_r(haze)=1.43.

Appendix A.4: Haze particles: effective variance

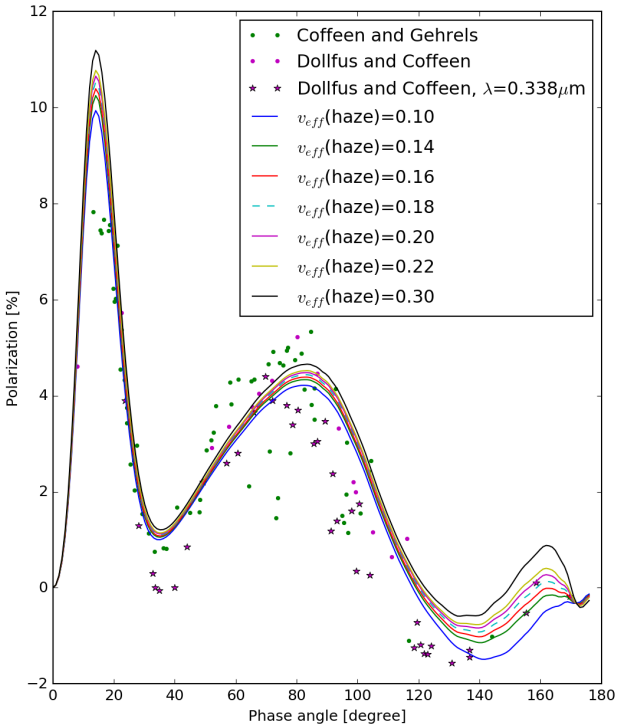

Fig. A.13: Effective variance of the haze particles for λ=0.340μm. Input: r_{eff}(cloud)=1.05μm, v_{eff}(cloud)=0.07, r_{eff}(haze)=0.25μm, N(cloud)=6.5 particles μm^{-2}, N(haze)=0.09 particles μm^{-2} and n_r(cloud)=n_r(haze)=1.47.

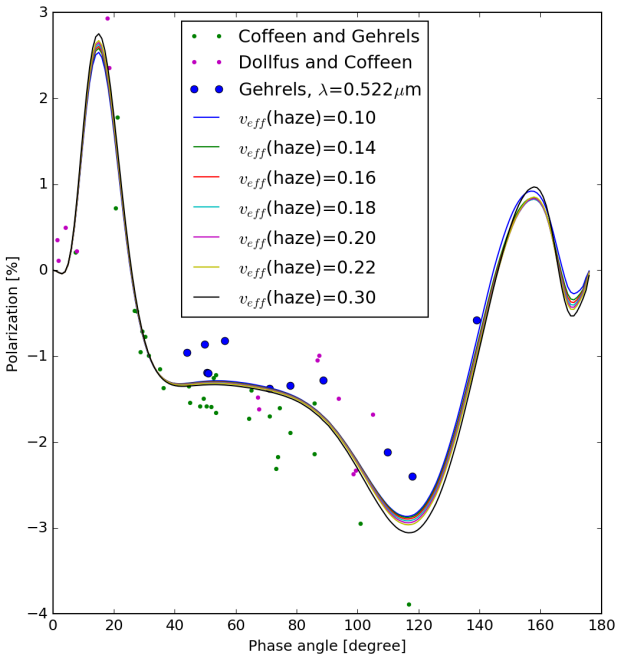

Fig. A.14: Effective variance of the haze for λ=0.520μm. Input: see Figure A.13 but with n_r(cloud)=n_r(haze)=1.44.

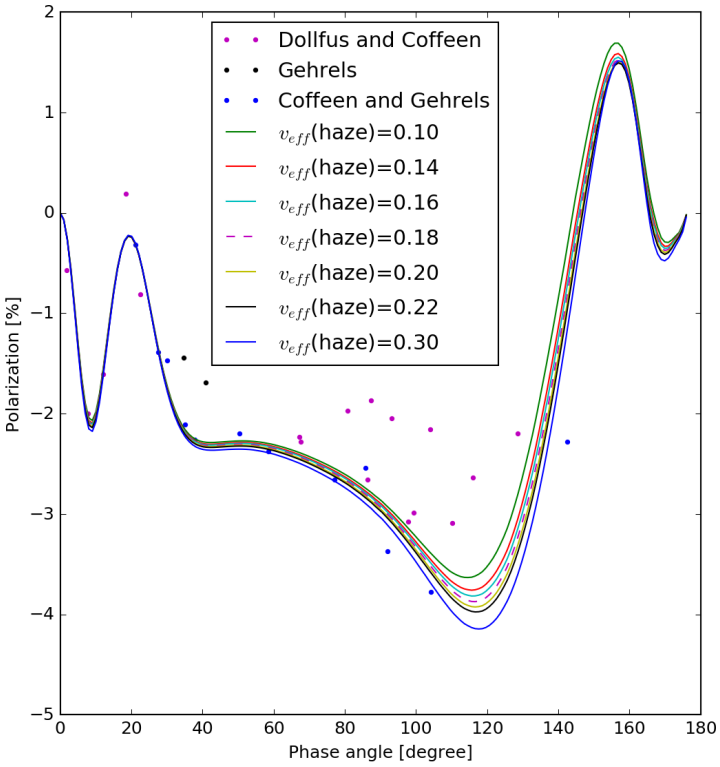

Fig. A.15: Effective variance of the haze particles for λ=0.650μm. Input: see Figure A.13 but with n_r(cloud)=n_r(haze)=1.44.

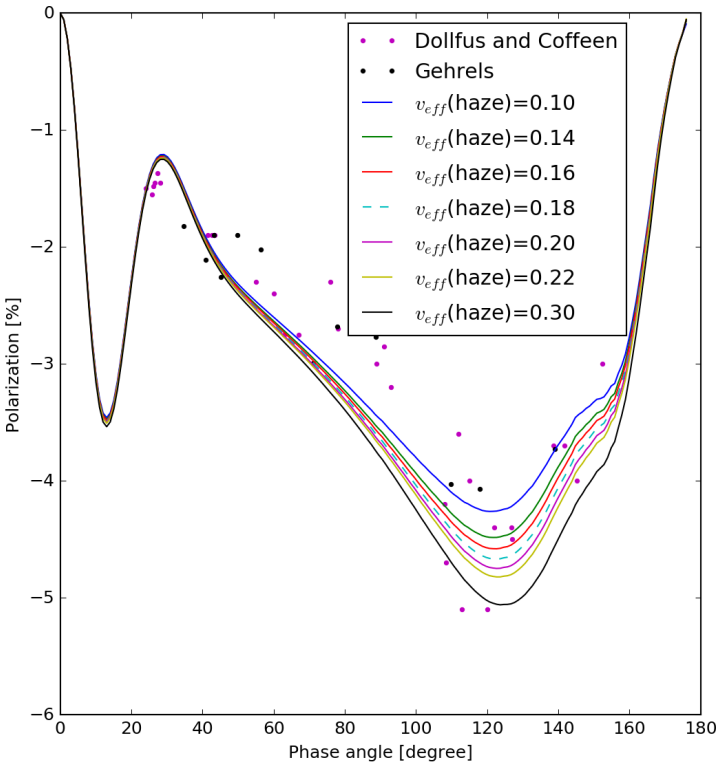

Fig. A.16: Effective variance of the haze for λ=0.950μm. Input: see Figure A.13 but with n_r(cloud)=n_r(haze)=1.43.

Appendix B: Log normal and Gamma distribution

The input for the *Two parameter gamma distribution* is the effective radius (r_{eff}) and the effective variance (v_{eff}) of the particles. The *Log normal distribution* uses r_g and σ. This means the r_{eff} and v_{eff} have to be transferred to r_g and σ. This is done with:

$$r_g = \frac{r_{eff}}{(v_{eff})^{5/2}} \tag{B.1}$$

$$\sigma = e^{\sqrt{ln(1+v_{eff})}} \tag{B.2}$$

When this is implemented in PyMieDAP, the two size distributions can be compared. For a selection of wavelengths, the results are shown below. The model used for the computations is the homogeneous Venus model containing clouds and hazes.

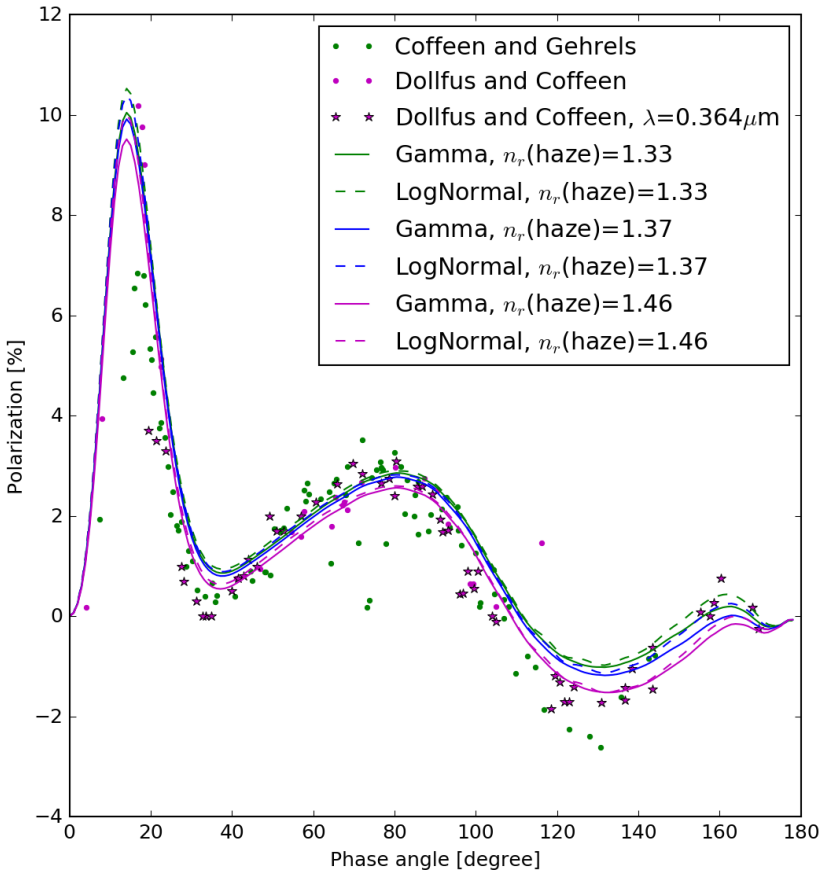

Fig. B.1: Log normal distribution (dotted lines) compared to gamma distribution (solid lines) for λ=0.365μm. Input: r_{eff}(cloud)=1.05μm, $v_{eff}(cloud)$ = 0.07, r_{eff}(haze)=0.25μm, v_{eff}(haze)= 0.18, N(cloud)=6.5, N(haze)=0.09 and n_r(cloud)=1.46.

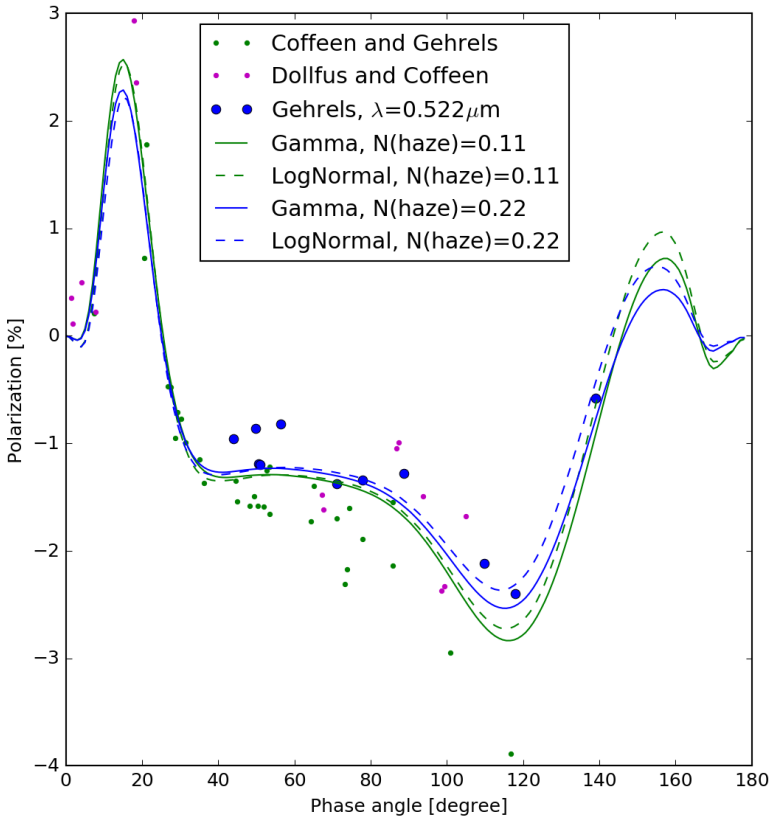

Fig. B.2: Log normal distribution (dotted lines) compared to gamma distribution (solid lines) for λ = 0.520μm. Input: see Figure B.1 but with n_r(cloud)=n_r(haze)=1.44

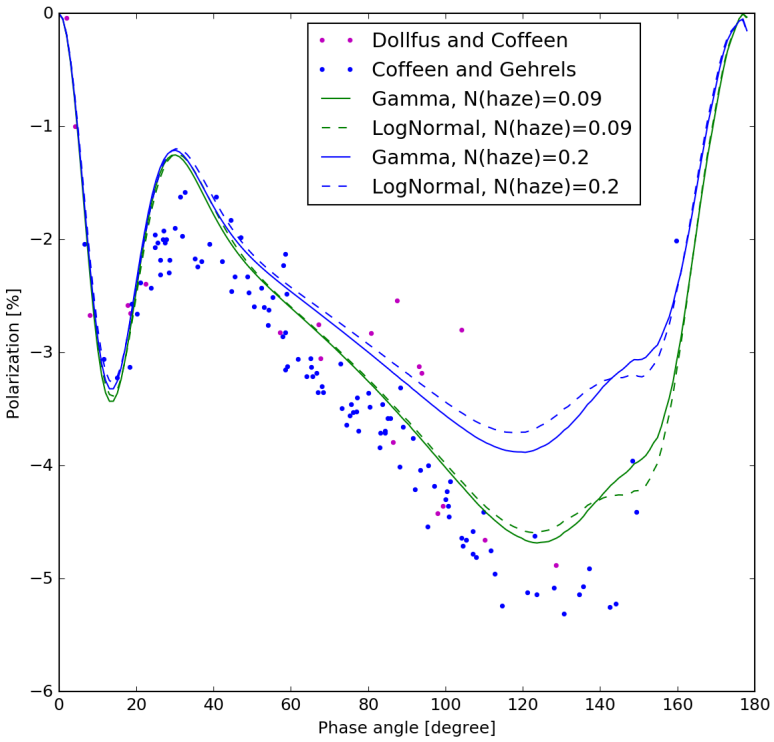

Fig. B.3: Log normal distribution (dotted lines) compared to gamma distribution (solid lines) for λ = 0.99μm. Input: see Figure B.1 but with n_r(cloud)=n_r(haze)=1.43

Appendix C: Sensitivity Study

For the sensitivity study the absorption is not yet added to the model, this explains why the fit is not optimized for the UV wavelengths. Every time a parameter is varied, the other parameters are fixed to a value which is considered optimal. This means the following for the input: $r_{eff}(cloud)$=1.05μm, $v_{eff}(cloud)$=0.07, $N(cloud)$=6.5 (or the corresponding optical thickness, $\tau(cloud)$), $r_{eff}(haze)$=0.25μm, v_{eff}=0.18, $N(haze)$=0.09 (or the corresponding optical thickness, $\tau(haze)$) and n_r=1.47 for λ=0.340μm, 1.46 for 0.365μm, 1.45 for 0.400μm, 1.45 for 0.445μm, 1.44 for 0.520μm, 1.44 for 0.550μm, 1.44 for 0.650μm, 1.44 for 0.685μm, 1.43 for 0.740μm, 1.43 for 0.840μm, 1.43 for 0.875μm, 1.43 for 0.950μm, 1.43 for 0.990μm

Appendix C.1: Cloud properties

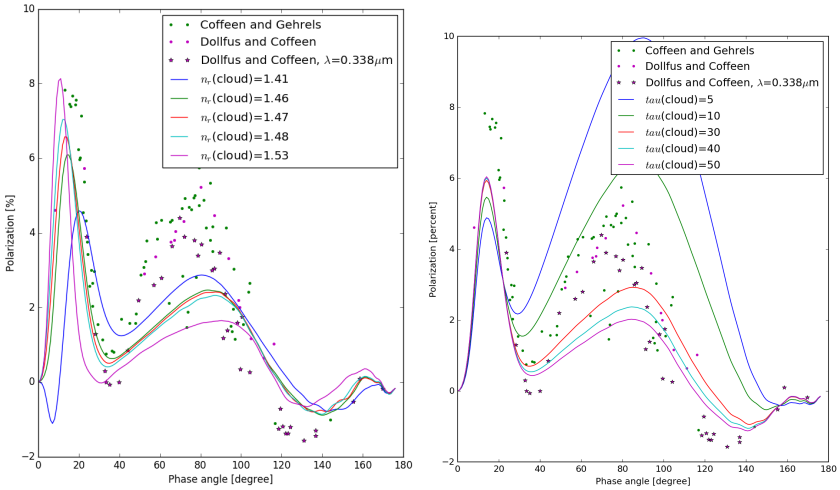

(a) (b)

Fig. C.1: Varying cloud properties for λ=0.340μm (*left*: refractive index, *right*: optical thickness)

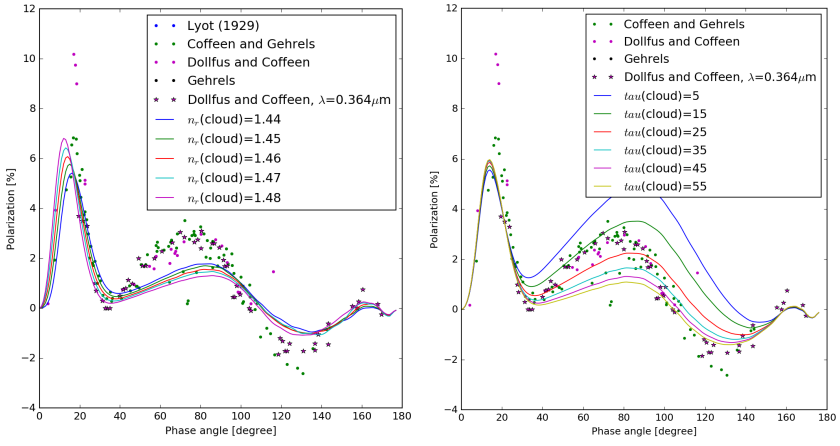

(a) (b)

Fig. C.2: Varying cloud properties for λ=0.365μm (*left*: refractive index, *right*: optical thickness)

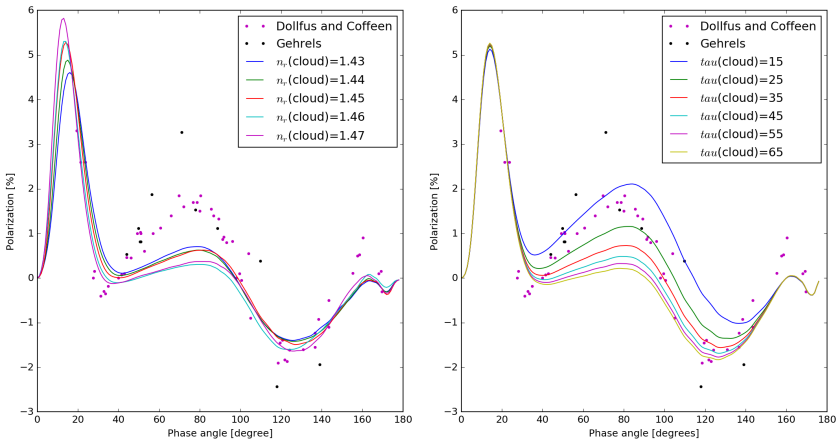

(a) (b)

Fig. C.3: Varying cloud properties for λ=0.400μm (*left*: refractive index, *right*: optical thickness)

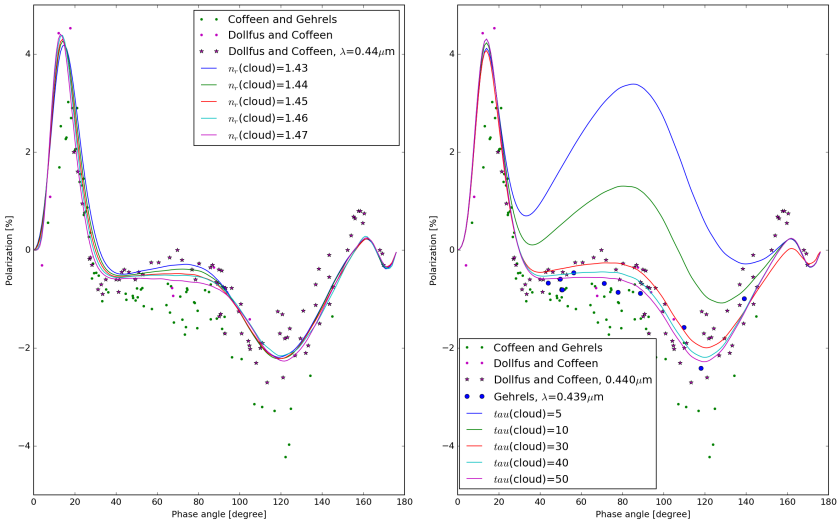

(a) (b)

Fig. C.4: Varying cloud properties for λ=0.445μm (*left*: refractive index, *right*: optical thickness)

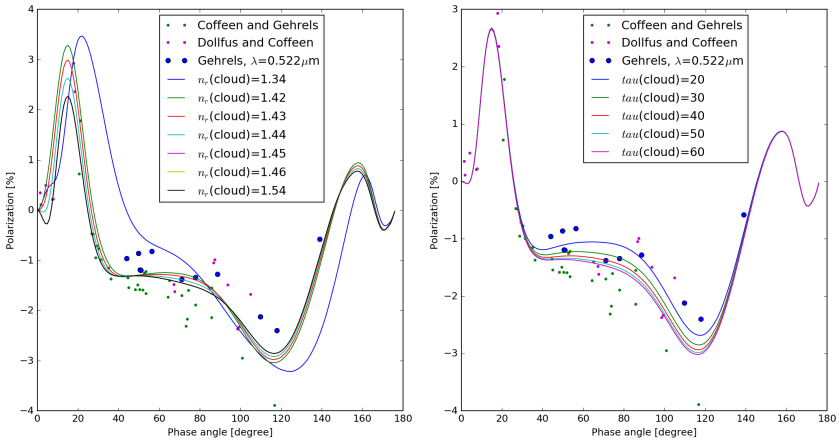

(a) (b)

Fig. C.5: Varying cloud properties for λ=0.520μm (*left*: refractive index, *right*: optical thickness)

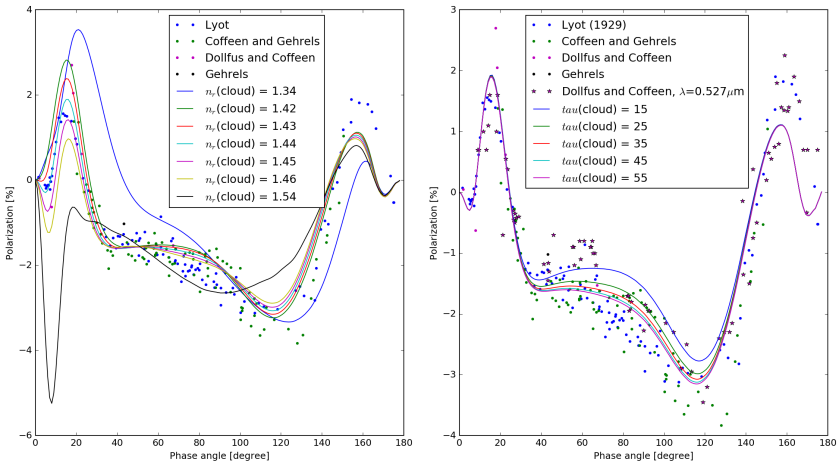

(a) (b)

Fig. C.6: Varying cloud properties for λ=0.550μm (*left*: refractive index, *right*: optical thickness)

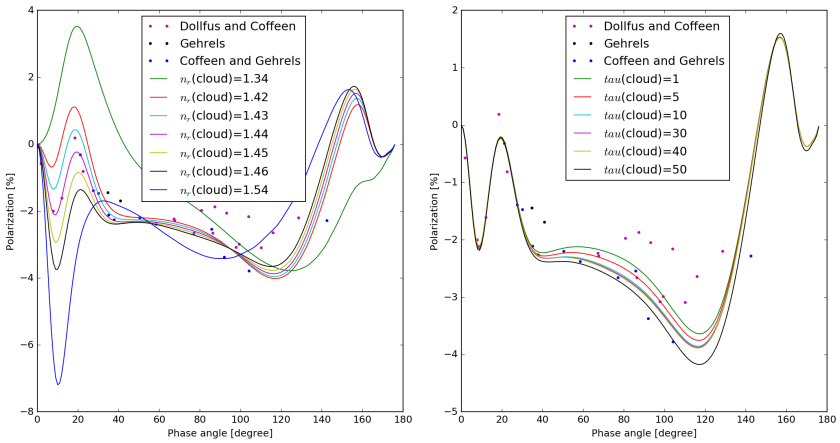

(a) (b)

Fig. C.7: Varying cloud properties for λ=0.650μm (*left*: refractive index, *right*: optical thickness)

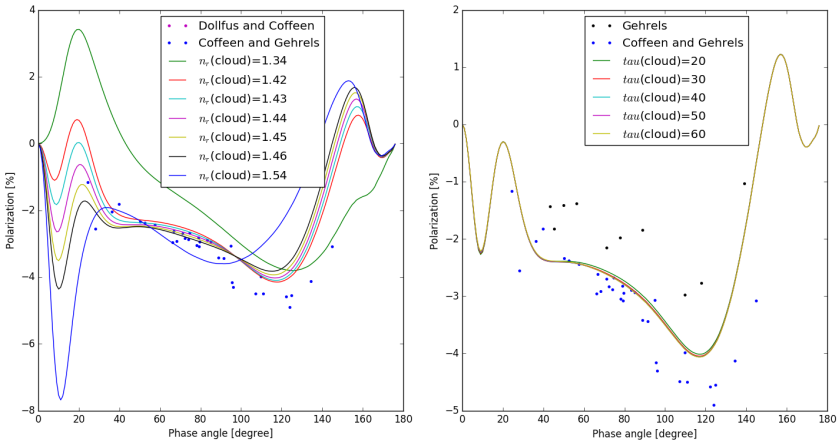

(a) (b)

Fig. C.8: Varying cloud properties for λ=0.685μm (*left*: refractive index, *right*: optical thickness)

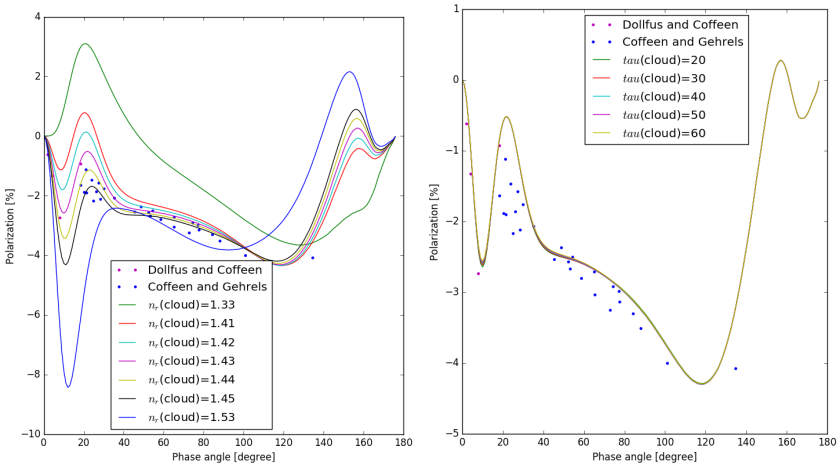

(a) (b)

Fig. C.9: Varying cloud properties for λ=0.740μm (*left*: refractive index, *right*: optical thickness)

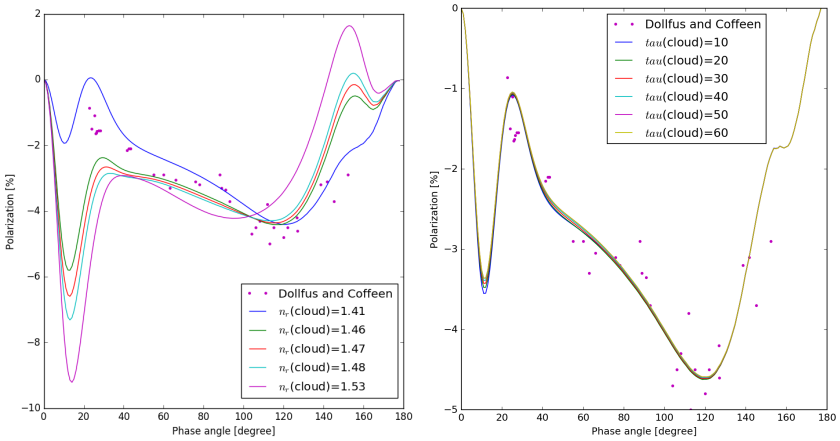

(a) (b)

Fig. C.10: Varying cloud properties for λ=0.840μm (*left*: refractive index, *right*: optical thickness)

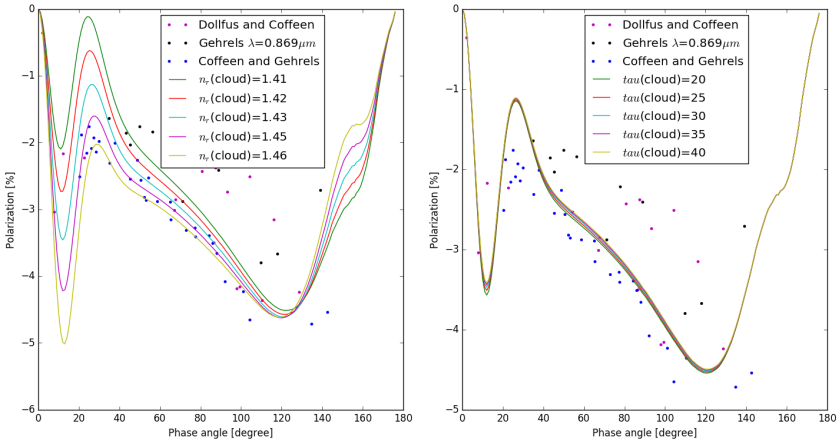

(a) (b)

Fig. C.11: Varying cloud properties for λ=0.875μm (*left*: refractive index, *right*: optical thickness)

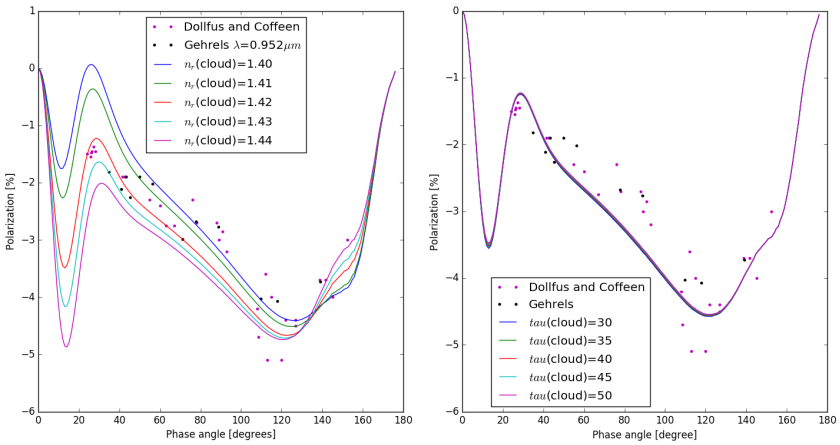

(a) (b)

Fig. C.12: Varying cloud properties for λ=0.950μm (*left*: refractive index, *right*: optical thickness)

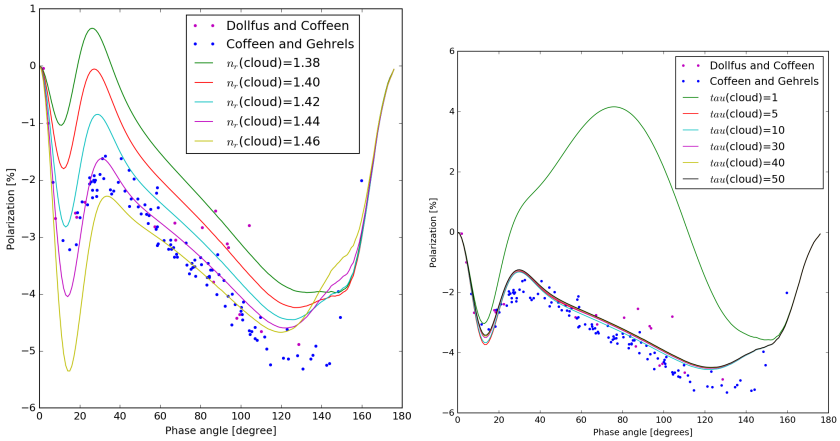

(a) (b)

Fig. C.13: Varying cloud properties for λ=0.990μm (*left*: refractive index, *right*: optical thickness)

Appendix C.2: Haze properties

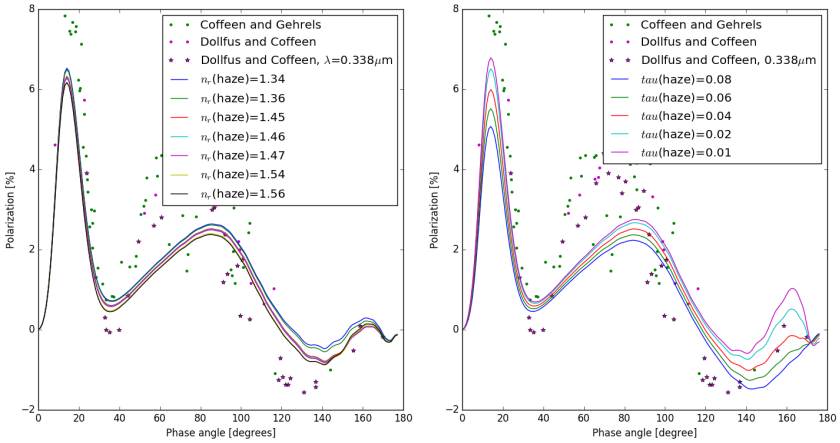

(a) (b)

Fig. C.14: Varying haze properties for λ=0.340μm (*left*: refractive index, *right*: optical thickness)

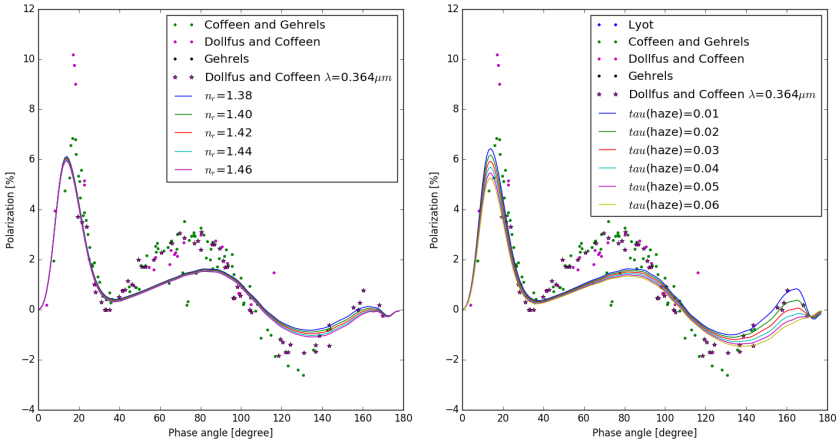

(a) (b)

Fig. C.15: Varying haze properties for λ=0.365μm (*left*: refractive index, *right*: optical thickness)

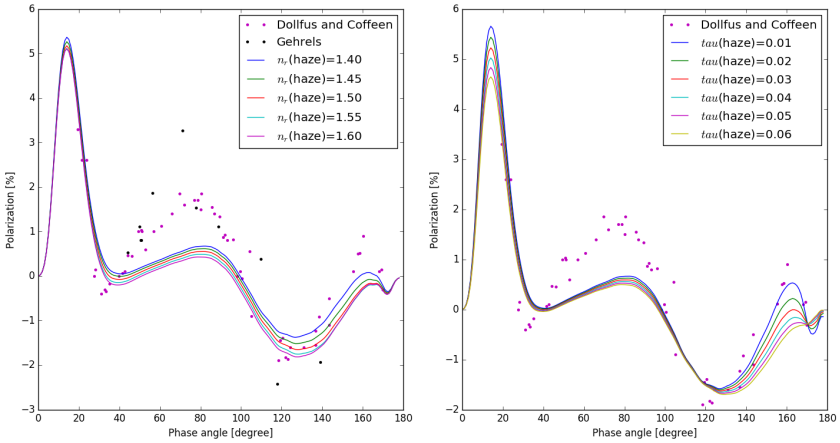

(a) (b)

Fig. C.16: Varying haze properties for λ=0.400μm (*left*: refractive index, *right*: optical thickness)

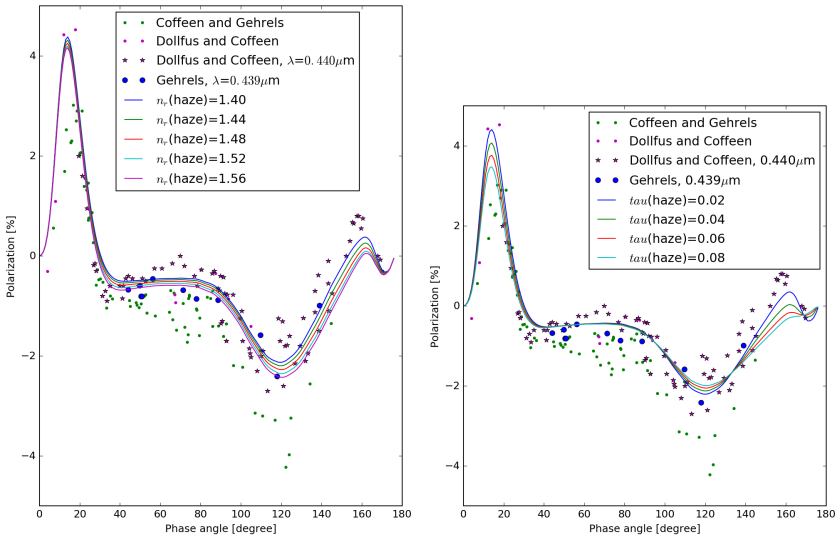

(a) (b)

Fig. C.17: Varying haze properties for λ=0.445μm (*left*: refractive index, *right*: optical thickness)

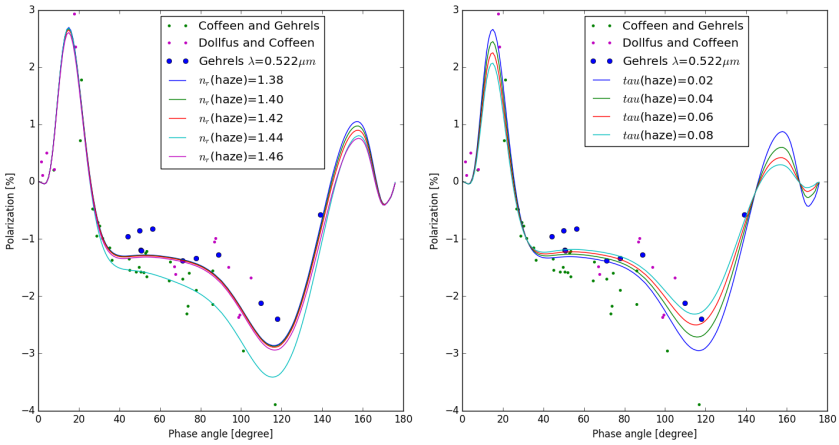

(a) (b)

Fig. C.18: Varying haze properties for λ=0.520μm (*left*: refractive index, *right*: optical thickness)

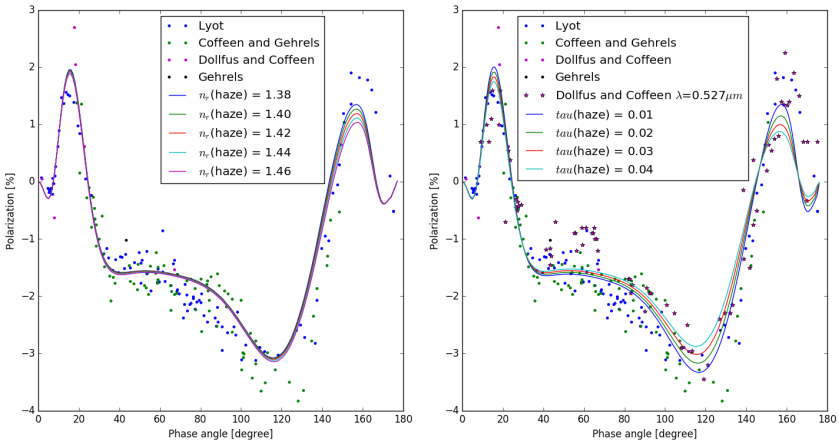

(a) (b)

Fig. C.19: Varying haze properties for λ=0.550μm (*left*: refractive index, *right*: optical thickness)

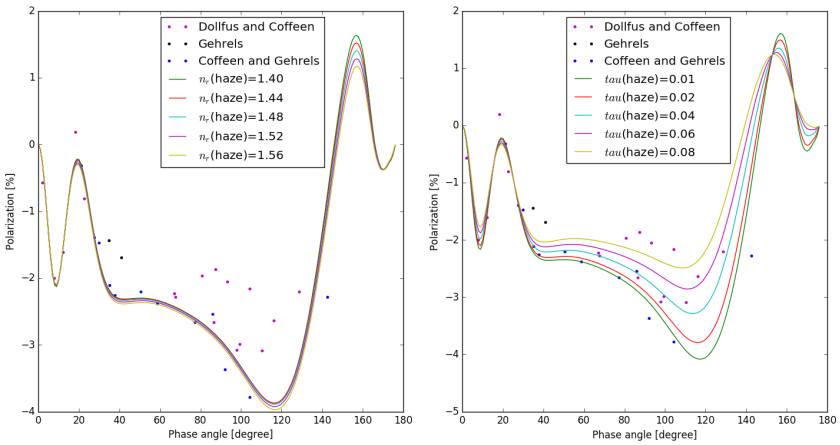

(a) (b)

Fig. C.20: Varying haze properties for λ=0.650μm (*left*: refractive index, *right*: optical thickness)

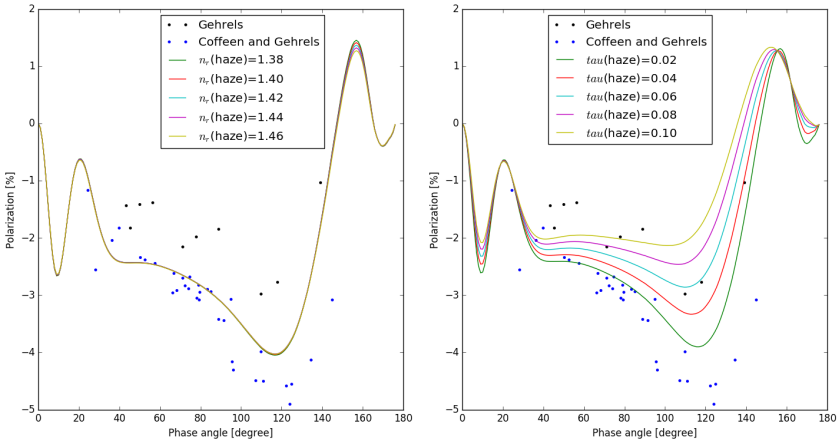

(a) (b)

Fig. C.21: Varying haze properties for λ=0.685μm (*left*: refractive index, *right*: optical thickness)

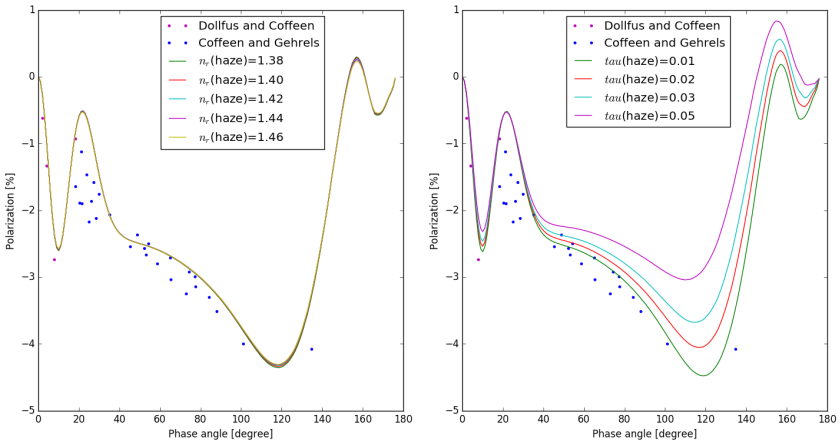

(a) (b)

Fig. C.22: Varying haze properties for λ=0.740μm (*left*: refractive index, *right*: optical thickness)

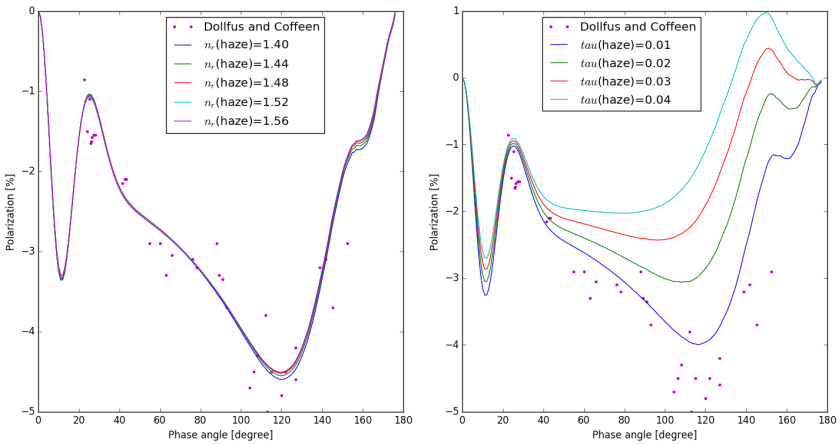

(a) (b)

Fig. C.23: Varying haze properties for λ=0.840μm (*left*: refractive index, *right*: optical thickness)

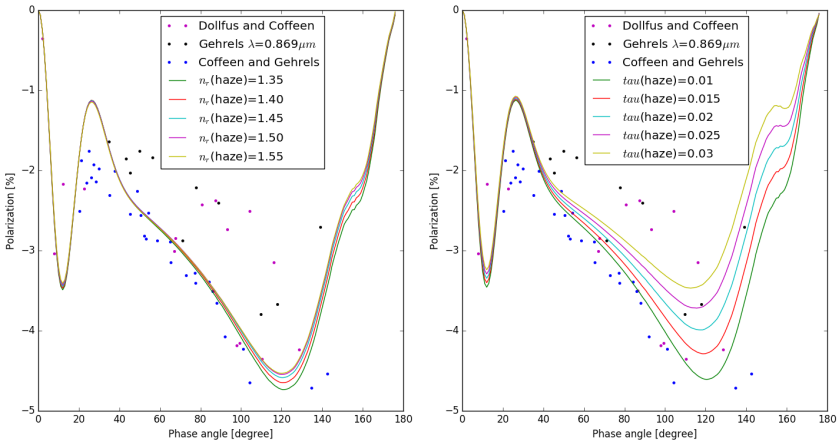

(a) (b)

Fig. C.24: Varying haze properties for λ=0.875μm (*left*: refractive index, *right*: optical thickness)

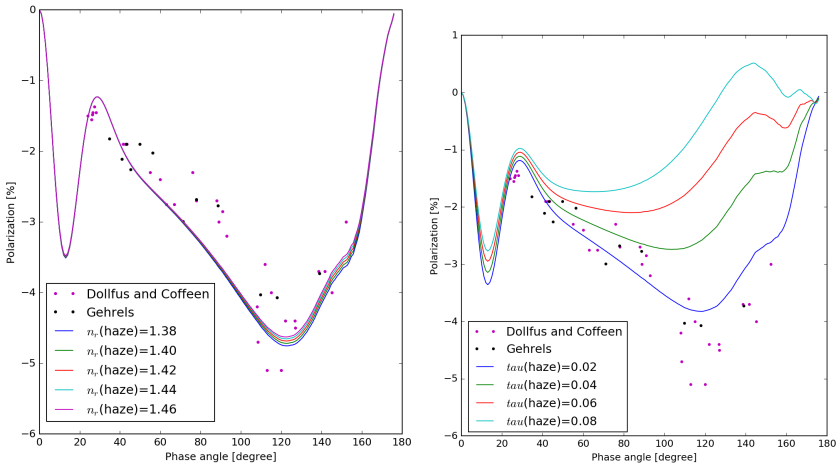

(a) (b)

Fig. C.25: Varying haze properties for λ=0.950μm (*left*: refractive index, *right*: optical thickness)

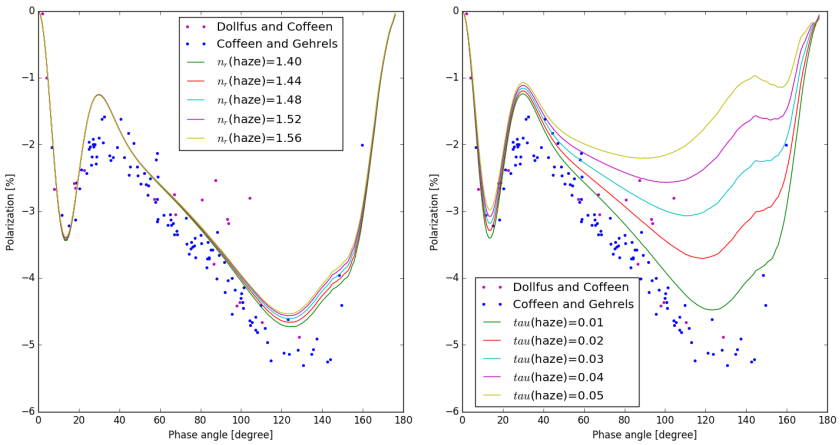

(a) (b)

Fig. C.26: Varying haze properties for λ=0.990μm (*left*: refractive index, *right*: optical thickness)

Appendix D: Absorption

Appendix D.1: Absorption around the equator and around the poles

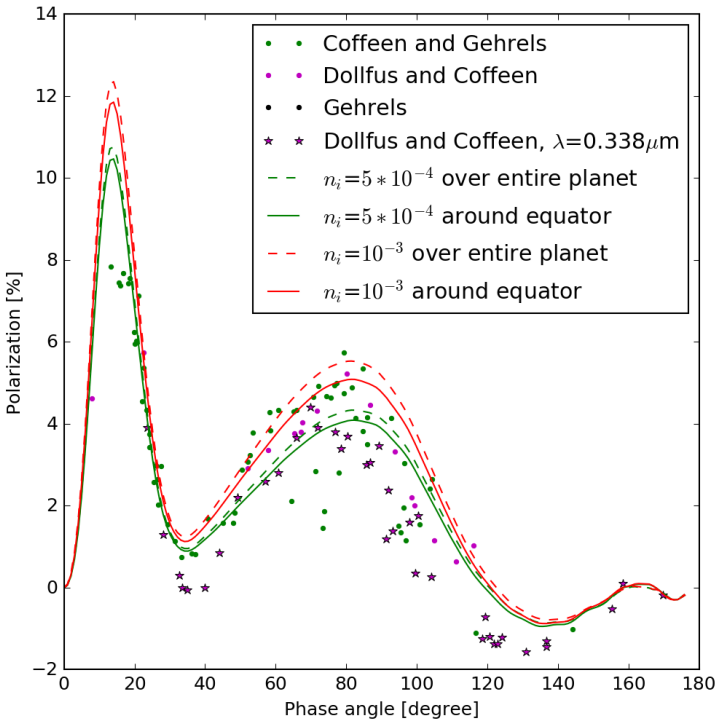

(a) Absorption at the equator.

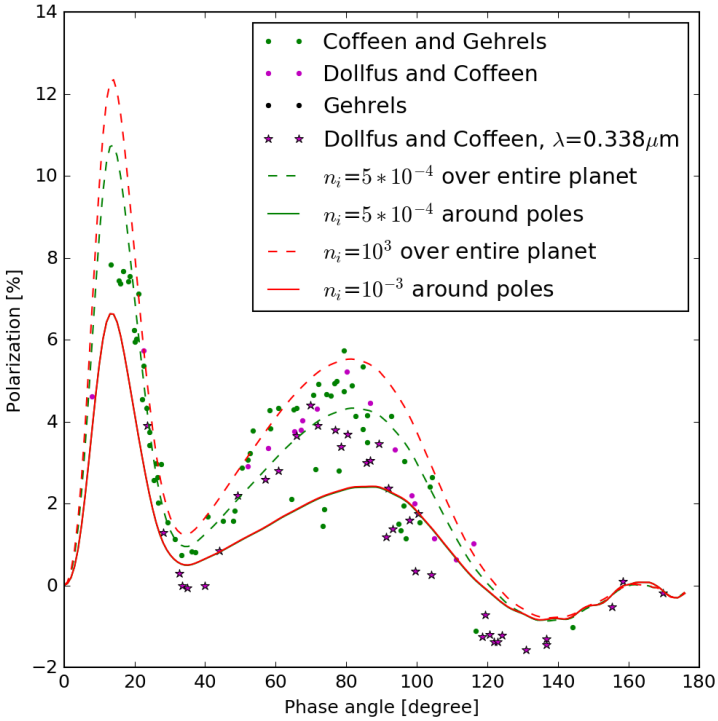

(b) Absorption at the poles.

Fig. D.1: Effect of adding absorption to the equator and poles for λ=0.34μm. r_{eff}(cloud)=1.05μm, v_{eff}(cloud)=0.07, r_{eff}(haze)=0.25μm, v_{eff}(haze)=0.18, N(cloud)=6.5 particle μm^{-2}, N(haze)=0.09 particle μm^{-2}, n_r(cloud)=1.466, n_r(haze)=1.466.

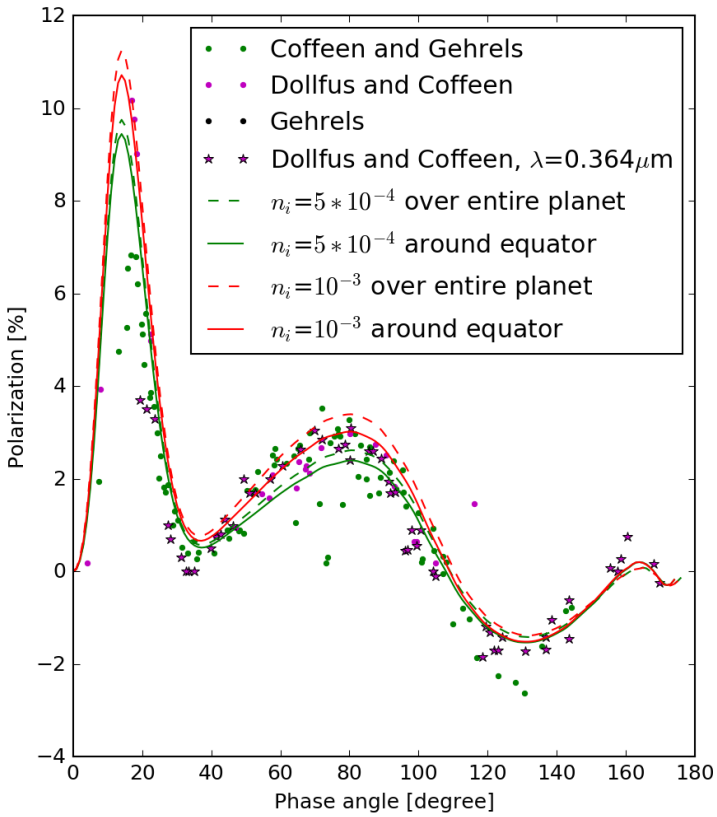

(a) Absorption at the equator.

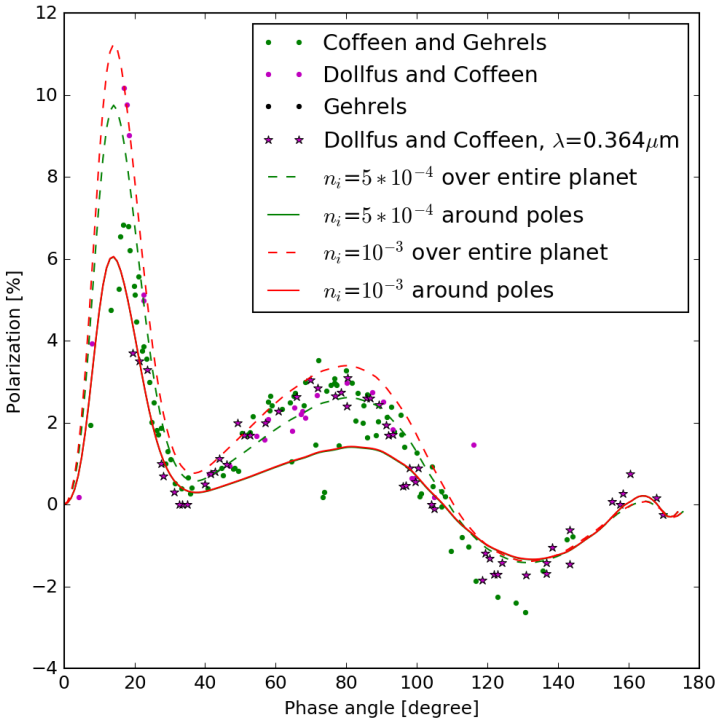

(b) Absorption at the poles.

Fig. D.2: Effect of adding absorption to the equator and poles for λ=0.365μm. r_{eff}(cloud)=1.05μm, v_{eff}(cloud)=0.07, r_{eff}(haze)=0.25μm, v_{eff}(haze)=0.18, N(cloud)=6.5 molecules μm^{-2}, N(haze)=0.09 molecules μm^{-2}, n_r(cloud)=1.460, n_r(haze)=1.460.

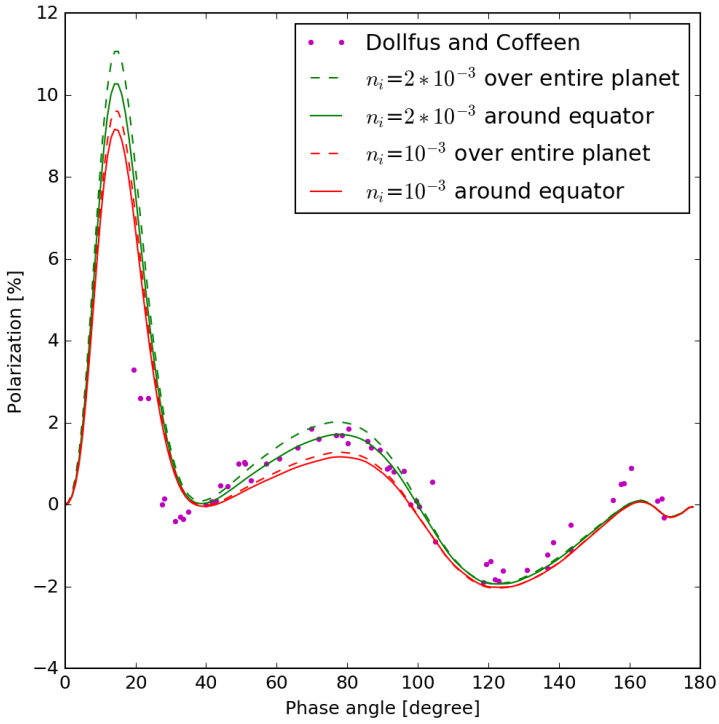

(a) Absorption at the equator.

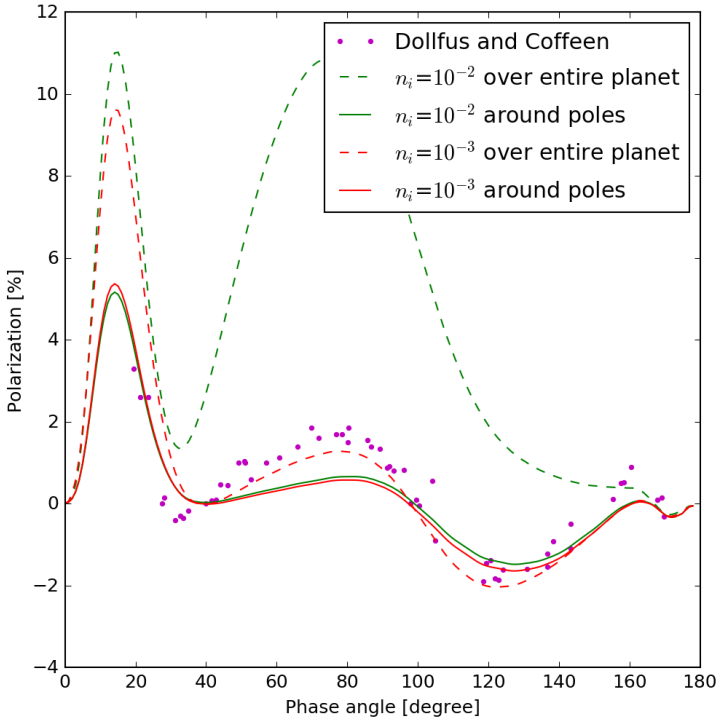

(b) Absorption at the poles.

Fig. D.3: Effect of adding absorption to the equator and poles for λ=0.400μm. r_{eff}(cloud)=1.05μm, v_{eff}(cloud)=0.07, r_{eff}(haze)=0.25μm, v_{eff}(haze)=0.18, N(cloud)=6.5 molecules μm^{-2}, N(haze)=0.09 molecules μm^{-2}, n_r(cloud)=1.45, n_r(haze)=1.45.

Appendix D.2: Patchy clouds

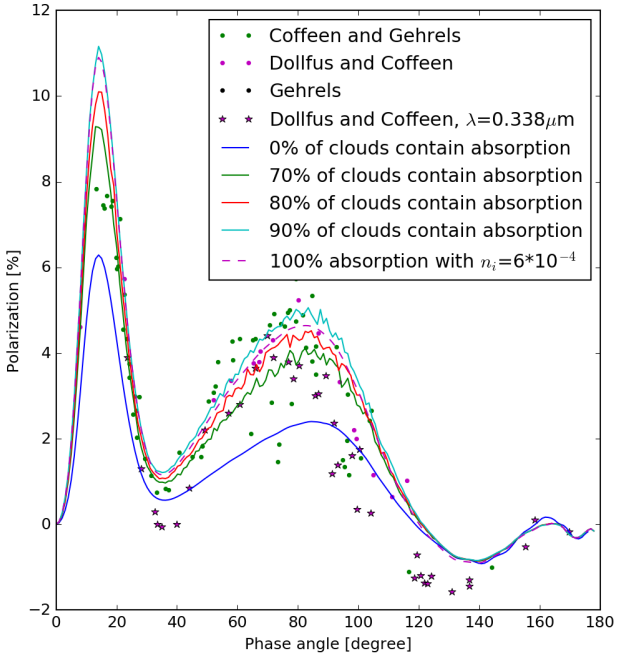

Fig. D.4: Different percentages of patchy clouds containing absorption for λ=0.340μm and 0.338μm. r_{eff}(cloud)=1.05μm, v_{eff}(cloud)=0.07, r_{eff}(haze)=0.25μm, v_{eff}(haze)=0.18, N(cloud)=6.5 particles μm^{-2}, N(haze)=0.09 particles μm^{-2}, n_r(cloud)=1.466, n_i(cloud, basic)=10^{-8}, n_i(cloud, patchy)=10^{-3}, n_r(haze)=1.466.

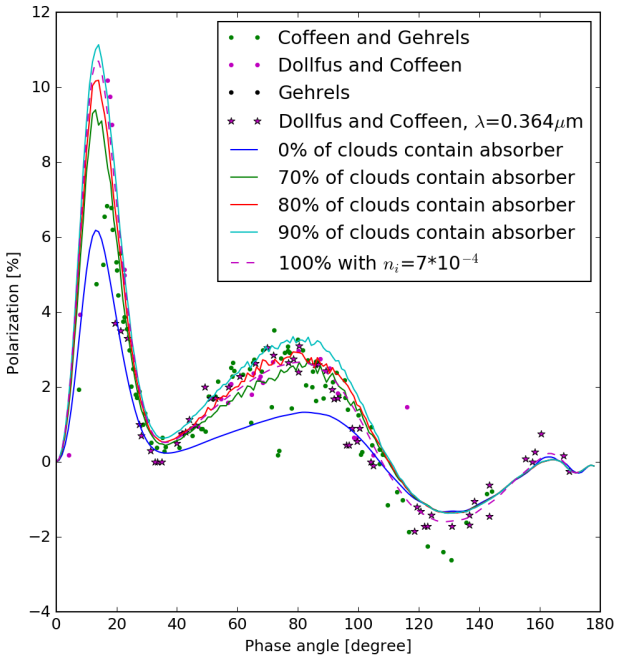

Fig. D.5: See Figure D.4 but for λ=0.365μm and 0.364μm with n_r(cloud)=1.46, n_i(cloud, basic)=10^{-8}, n_i(cloud, patchy)=1.5*10^{-3}, n_r(haze)=1.46.

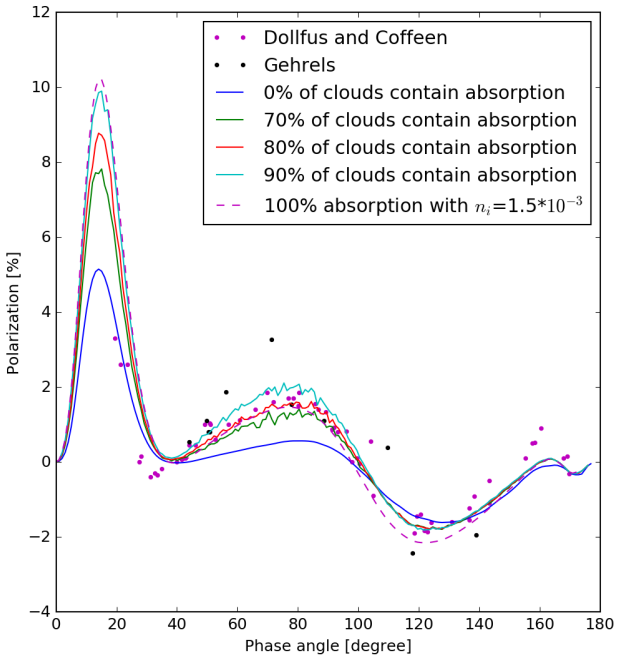

Fig. D.6: See Figure D.4 but for λ=0.400μm with n_r(cloud)=1.45, n_i(cloud, basic)=10^{-8}, n_i(cloud, patchy)=3*10^{-3}, n_r(haze)=1.45.

Appendix D.3: Subsolar cloud

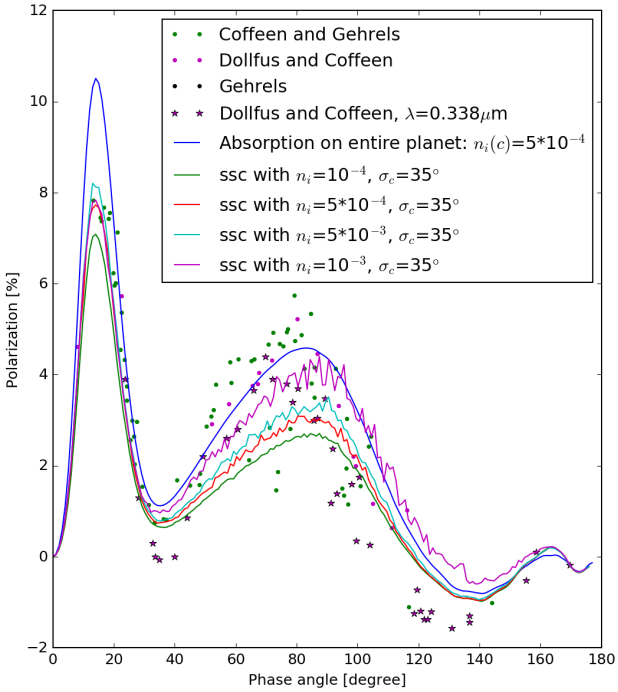

Fig. D.7: Subsolar cloud (ssc) containing absorber for λ=0.340μm. Input: r_{eff}(cloud)=1.05μm, v_{eff}(cloud)=0.07, r_{eff}(haze)=0.25μm, v_{eff}=0.18, N(cloud)=6.5 particles μm^{-2}, N(haze)=0.09 particles μm^{-2}, n_r(cloud)=n_r(ssc)=1.466, n_i(cloud)=10^{-8}, n_r(haze)=1.466.

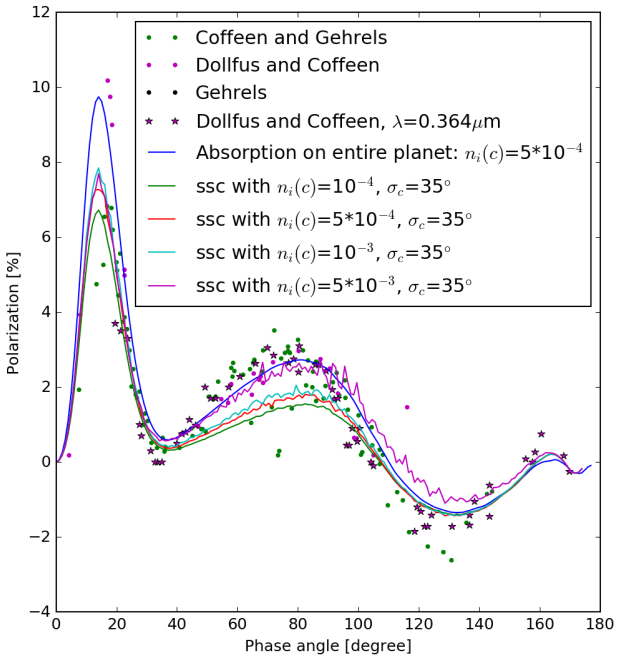

Fig. D.8: See Figure D.7 but for λ=0.365μm with n_r(cloud)=n_r(ssc)=1.46 and n_r(haze)=1.46.

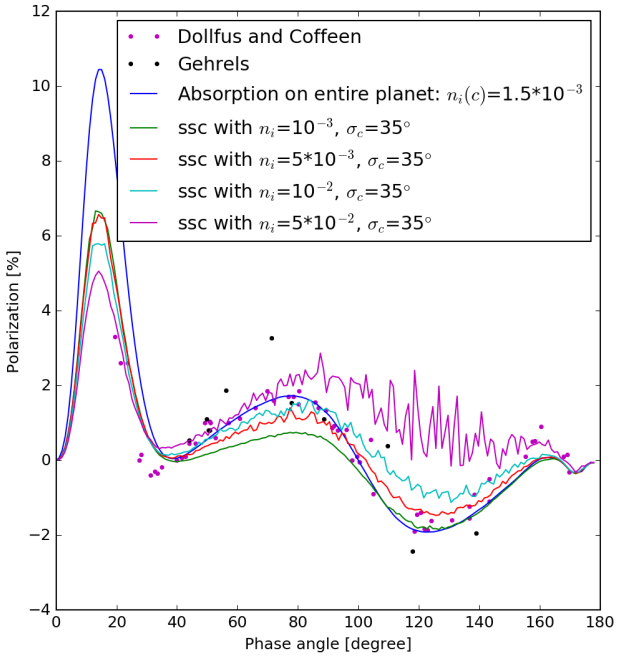

Fig. D.9: See Figure D.7 but for λ=0.400μm with n_r(cloud)=n_r(ssc)=1.45 and n_r(haze)=1.45.

Appendix D.4: Absorption in the gas

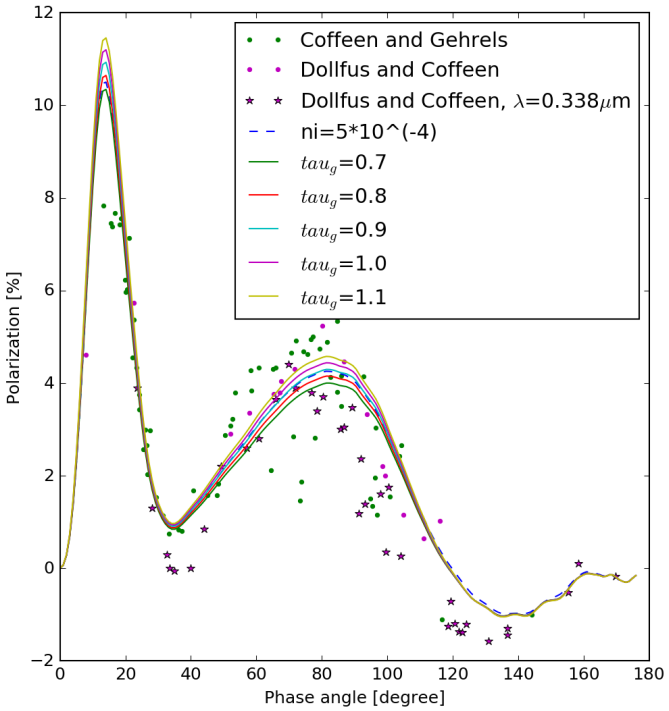

Fig. D.10: Absorption in the gas for λ=0.340μm and 0.338μm. r_{eff}(cloud)=1.05μm, v_{eff}(cloud)=0.07, r_{eff}(haze)=0.25μm, v_{eff}(haze)=0.18, N(cloud)=6.5 particles μm^{-2}, N(haze)=0.09 particles μm^{-2}, n_r(cloud)=1.466, n_r(haze)=1.466.

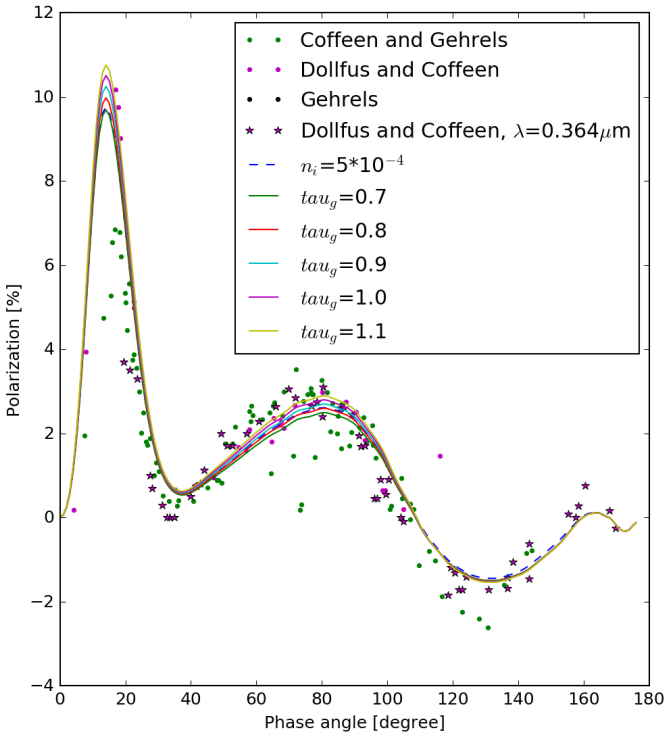

Fig. D.11: See Figure D.10 but for λ=0.365μm and 0.364μm and with n_r(cloud)=1.46 and n_r(haze)=1.46.

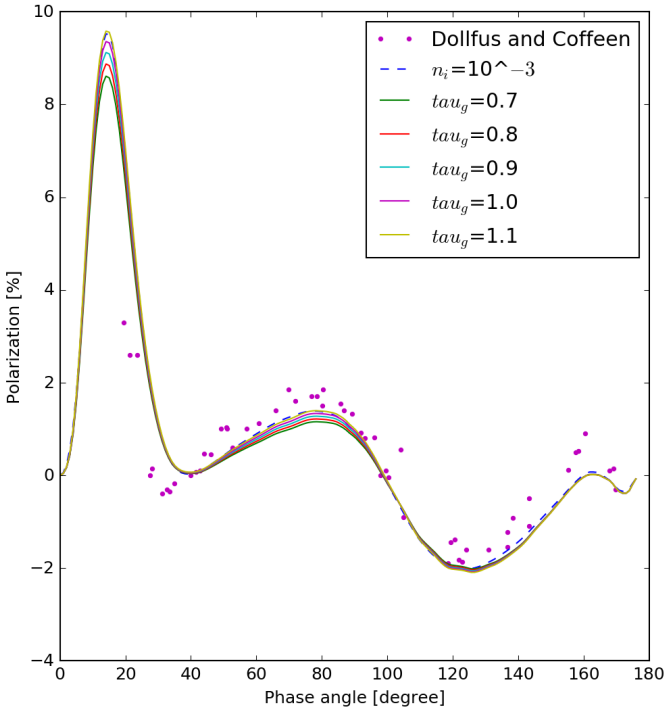

Fig. D.12: See Figure D.10 but for λ=0.400μm and with n_r(cloud)=1.46, n_r(haze)=1.46.

Appendix E: Horizontal inhomogeneity

Appendix E.1: Column number density haze

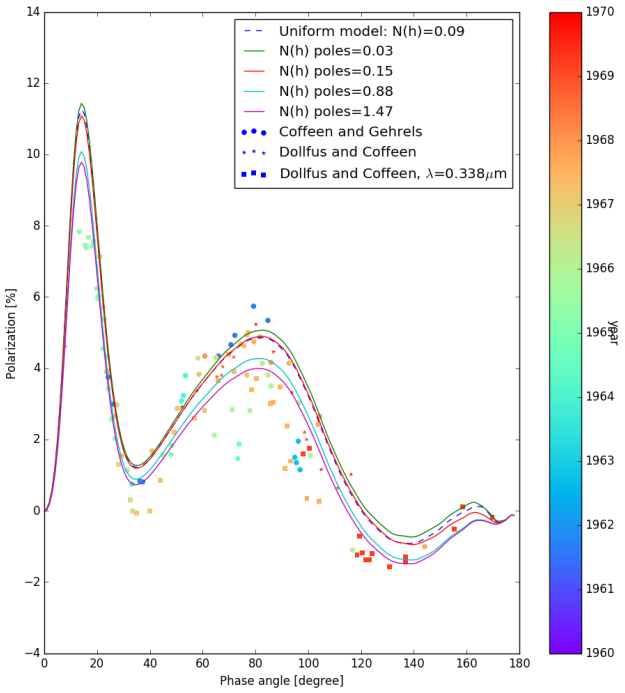

Fig. E.1: Changing the column number density [$particles\ \mu m^{-2}$] of the polar haze for $\lambda = 0.340\mu m$. Input: r_{eff}(cloud)=1.05μm, v_{eff}(cloud)=0.07, r_{eff}(haze)=0.25μm, v_{eff}(haze)=0.18, N(cloud, equatorial)=6.5 particles μm^{-2}, N(haze)=0.09 particles μm^{-2} and n_r(cloud)=1.466, n_r(haze)=1.466.

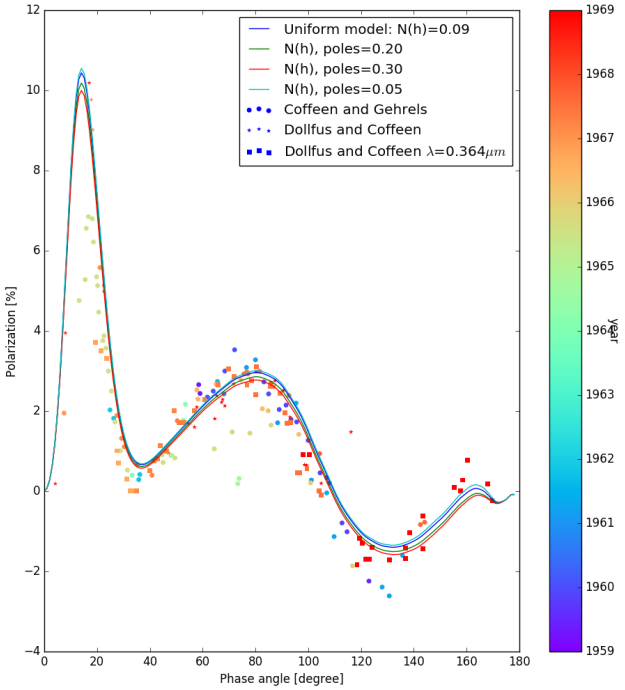

Fig. E.2: Changing the column number density [$particles\ \mu m^{-2}$] of the polar haze for $\lambda = 0.365\mu m$. Input: r_{eff}(cloud)=1.05μm, v_{eff}(cloud)=0.07, r_{eff}(haze)=0.25μm, v_{eff}(haze)=0.18, N(cloud, equatorial)=6.5 particles μm^{-2}, N(haze)=0.09 particles μm^{-2} and n_r(cloud)=1.46, n_r(haze)=1.46.

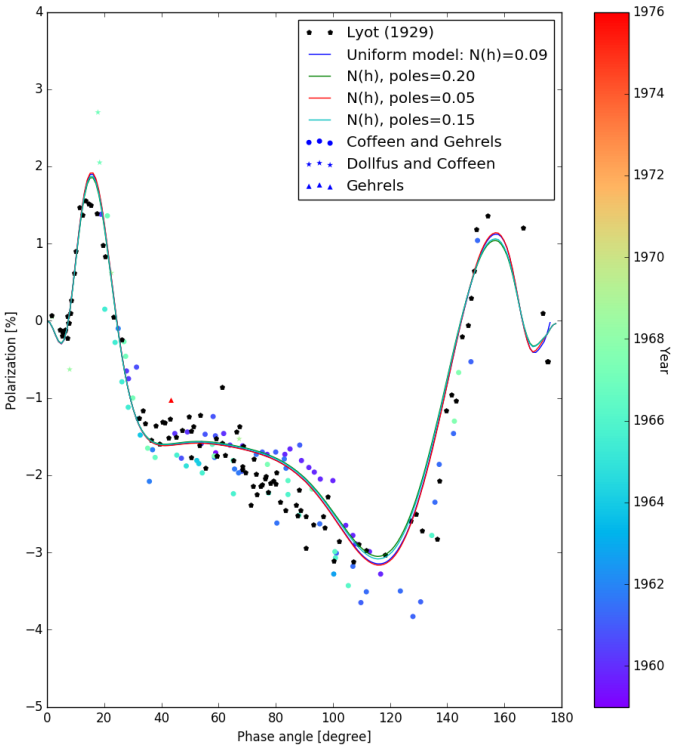

Fig. E.3: Changing the column number density [$particles\ \mu m^{-2}$] of the polar haze for $\lambda = 0.550\mu m$. Input: r_{eff}(cloud)=1.05μm, v_{eff}(cloud)=0.07, r_{eff}(haze)=0.25μm, v_{eff}(haze)=0.18, N(cloud, equatorial)=6.5 particles μm^{-2}, N(haze)=0.09 particles μm^{-2} and n_r(cloud)=1.44, n_r(haze)=1.44.

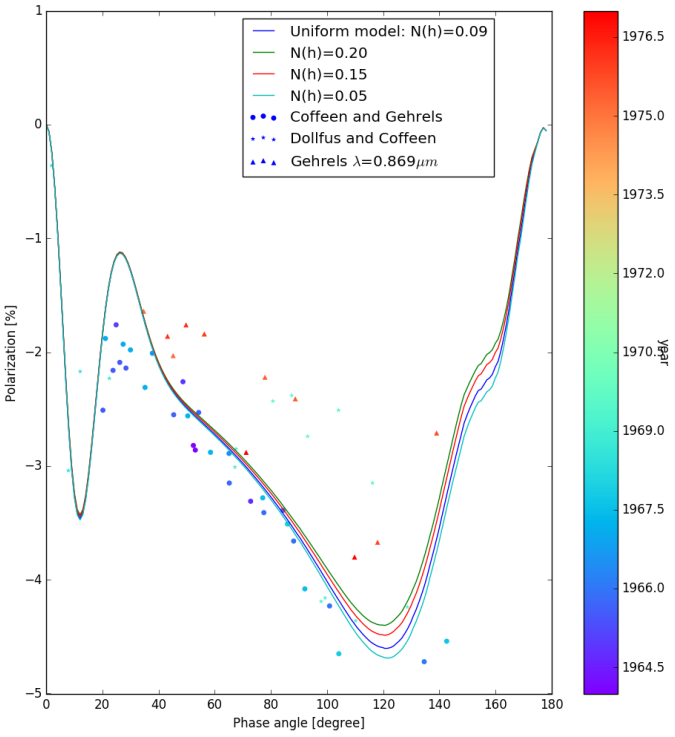

Fig. E.4: Changing the column number density [$particles\ \mu m^{-2}$] of the polar haze for $\lambda = 0.875\mu m$. Input: r_{eff}(cloud)=1.05μm, v_{eff}(cloud)=0.07, r_{eff}(haze)=0.25μm, v_{eff}(haze)=0.18, N(cloud, equatorial)=6.5 particles μm^{-2}, N(haze)=0.09 particles μm^{-2} and n_r(cloud)=1.43, n_r(haze)=1.43.

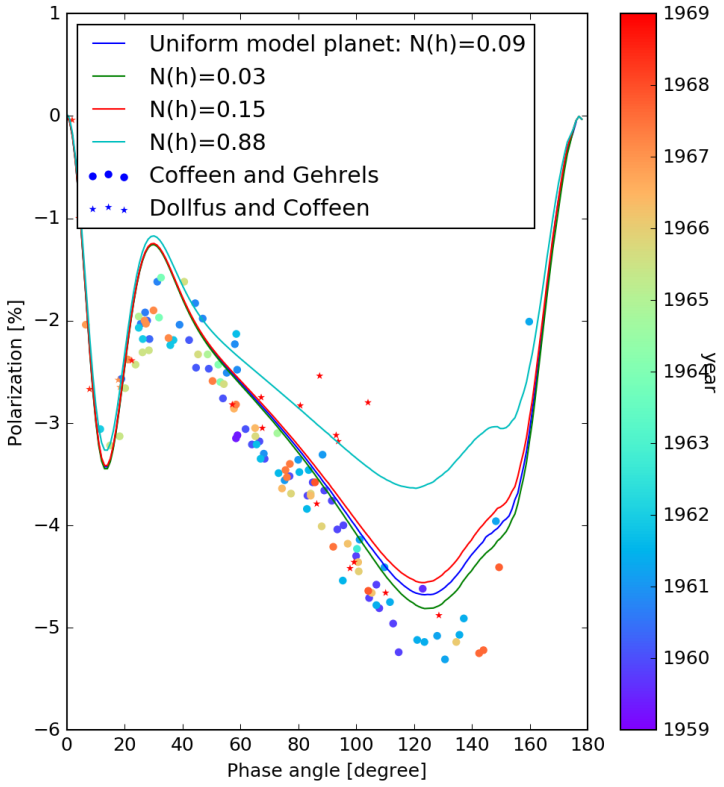

Fig. E.5: Changing the column number density [$particles\ \mu m^{-2}$] of the polar haze for $\lambda = 0.990 \mu m$. Input: r_{eff}(cloud)=1.05μm, v_{eff}(cloud)=0.07, r_{eff}(haze)=0.25μm, v_{eff}(haze)=0.18, N(cloud, equatorial)=6.5 particles μm^{-2}, N(haze)=0.09 particles μm^{-2} and n_r(cloud)=1.43, n_r(haze)=1.43.

Appendix E.2: Effective radius haze

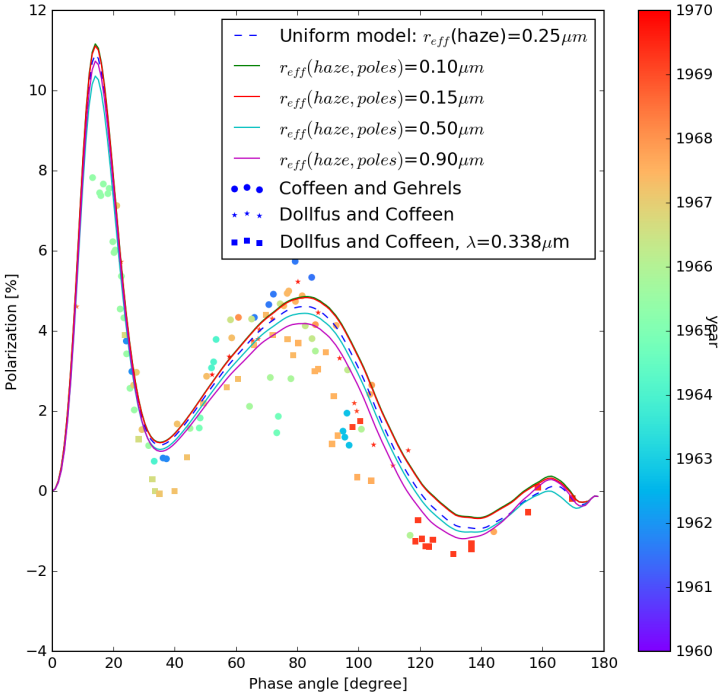

Fig. E.6: Changing the effective radius of the polar haze for $\lambda = 0.340 \mu m$.

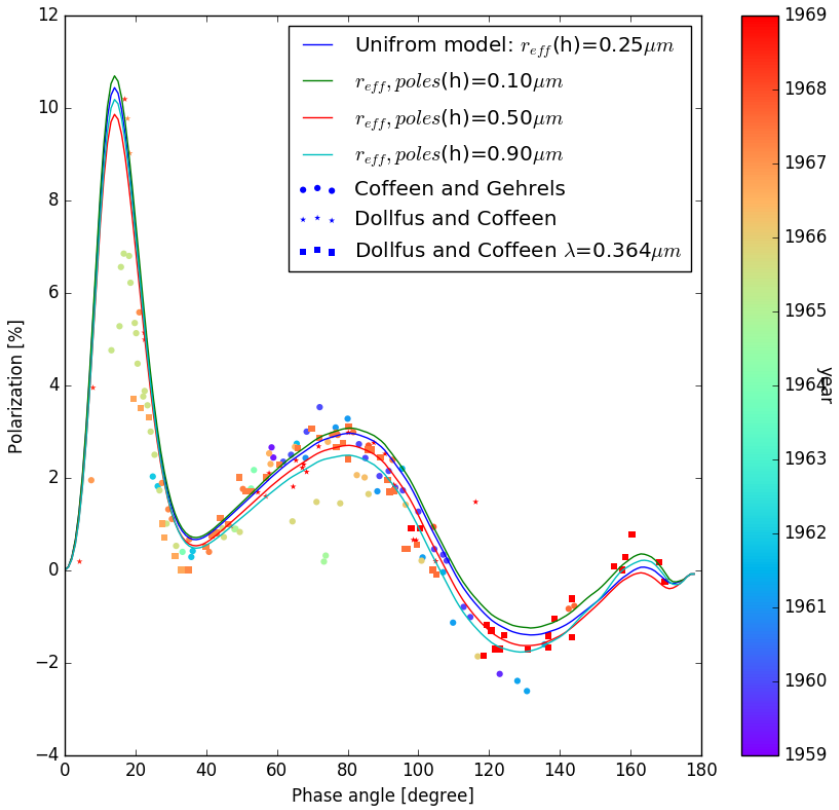

Fig. E.7: Changing the effective radius of the polar haze for $\lambda = 0.365 \mu m$.

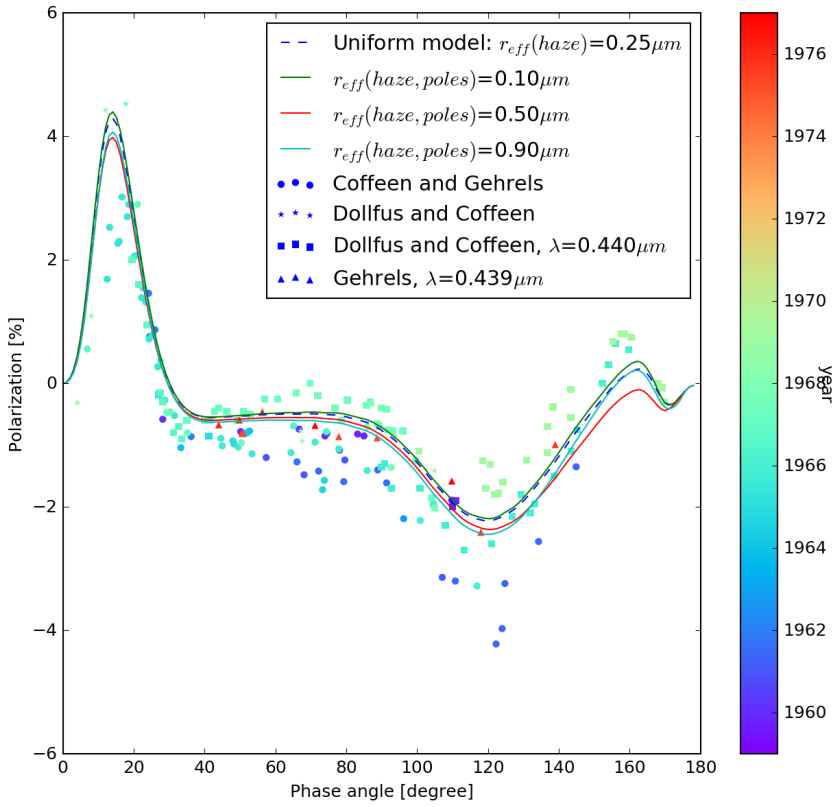

Fig. E.8: Changing the effective radius of the polar haze for $\lambda = 0.445 \mu m$.

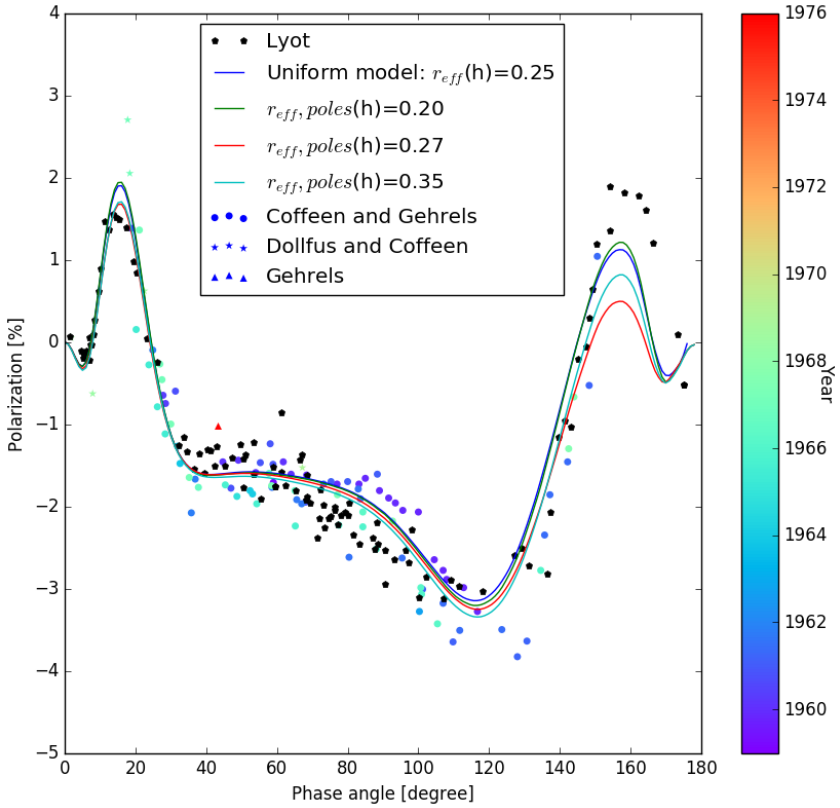

Fig. E.9: Changing the effective radius [μm] of the polar haze for $\lambda = 0.550 \mu m$.

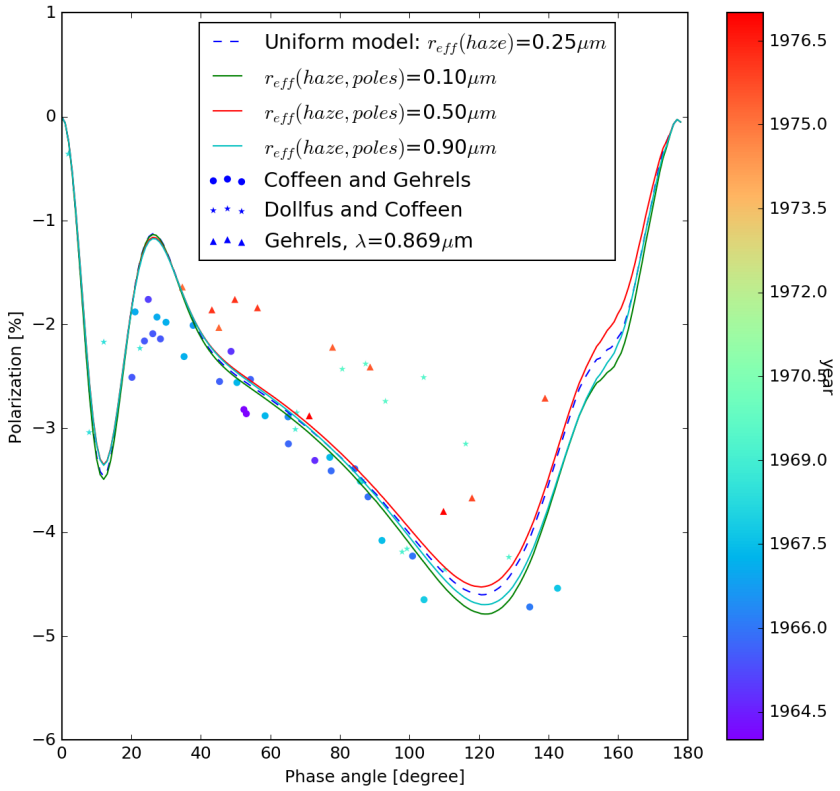

Fig. E.10: Changing the effective radius of the polar haze for $\lambda = 0.875 \mu m$.

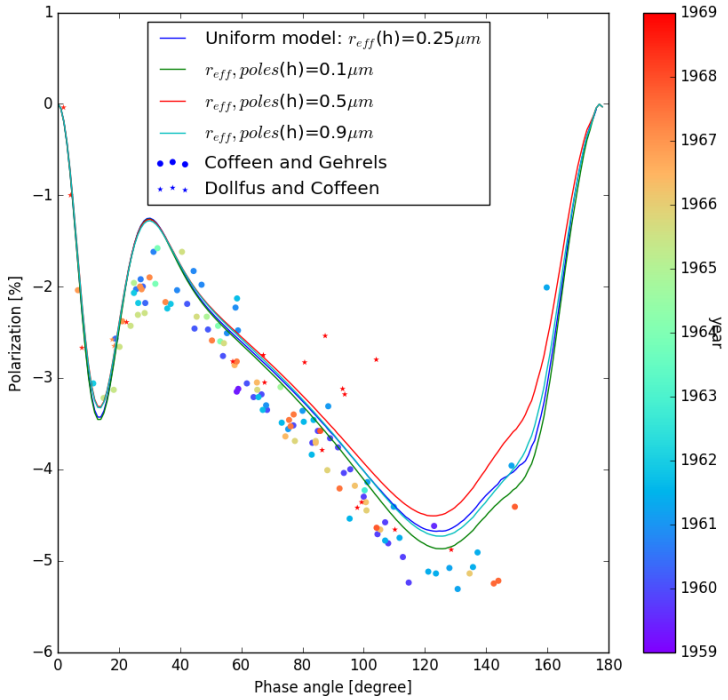

Fig. E.11: Changing the effective radius of the polar haze for $\lambda = 0.990\mu m$.

Appendix E.3: Haze top pressure

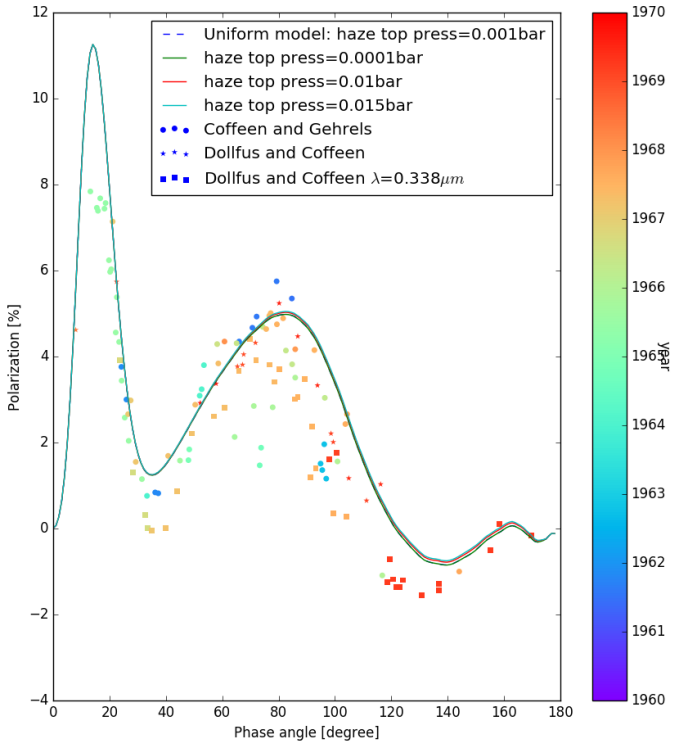

Fig. E.12: Changing the haze top pressure in the polar region for $\lambda = 0.340\mu m$.

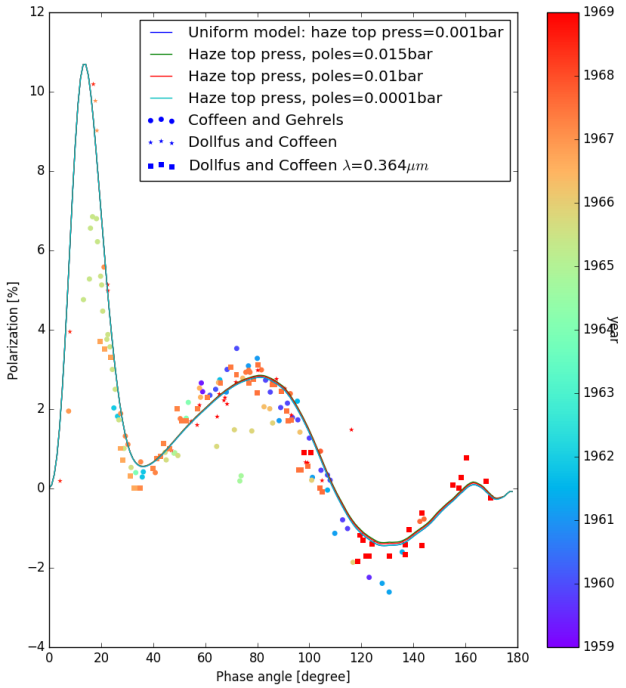

Fig. E.13: Changing the haze top pressure in the polar region for $\lambda = 0.365\mu m$.

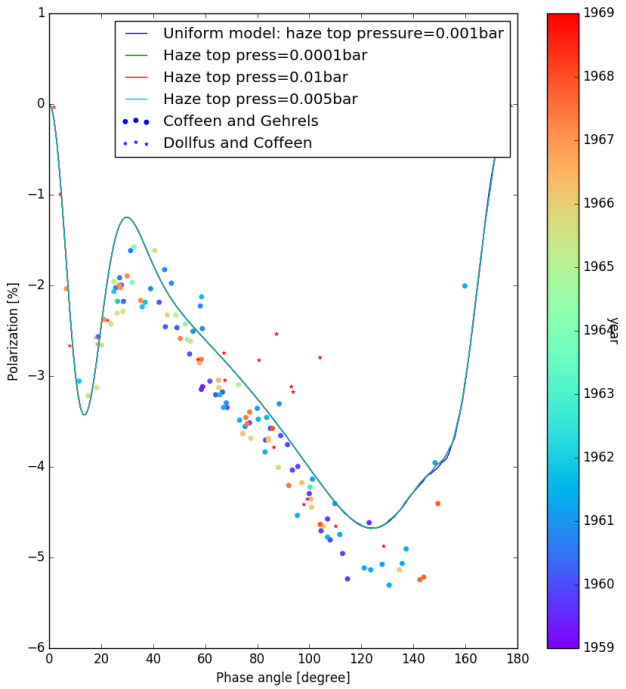

Fig. E.14: Changing the haze top pressure in the polar region for $\lambda = 0.990\mu m$.

Appendix E.4: Refractive index of the haze

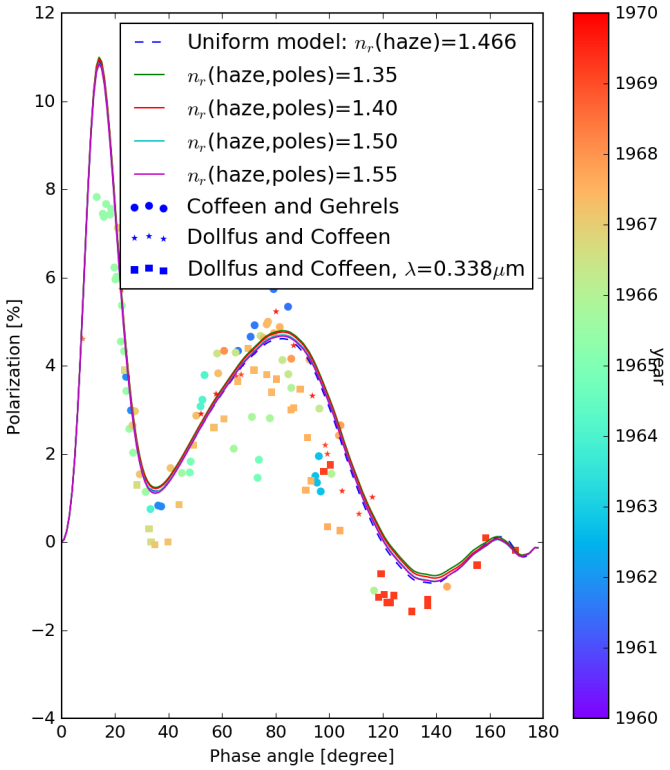

Fig. E.15: Changing the refractive index of the haze particles in the polar region for $\lambda = 0.340\mu m$.

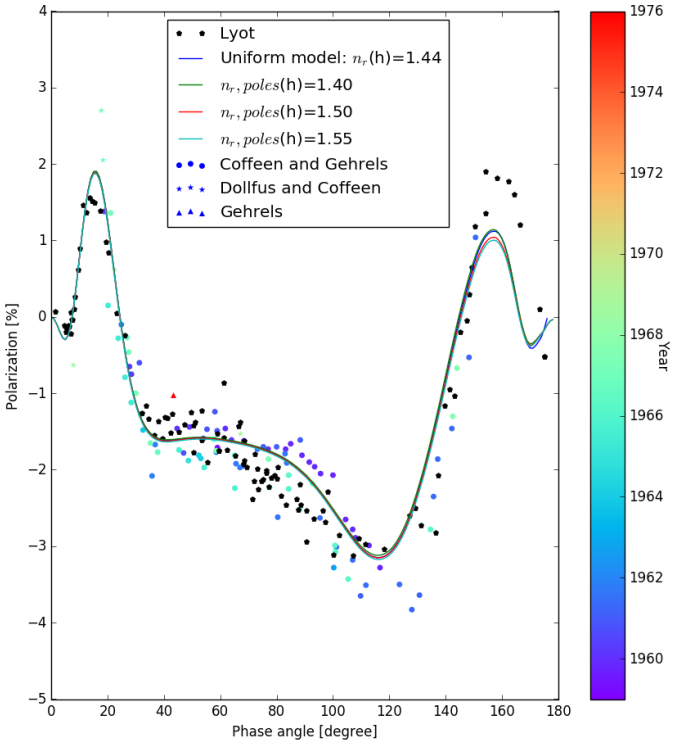

Fig. E.16: Changing the refractive index of the haze in the polar region for $\lambda = 0.550\mu m$.

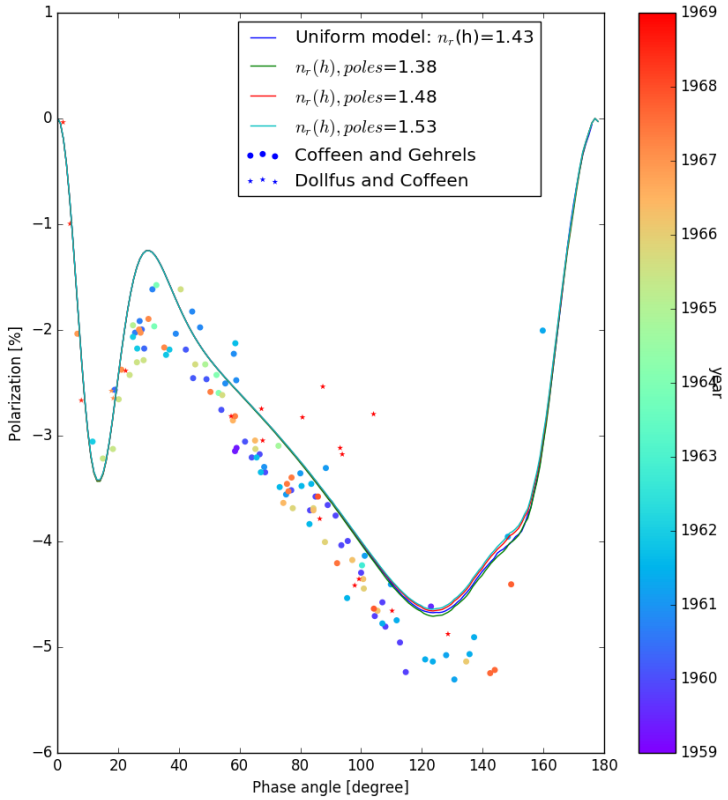

Fig. E.17: Changing the refractive index of the haze in the polar region for $\lambda = 0.990 \mu m$.

Appendix E.5: Column number density cloud

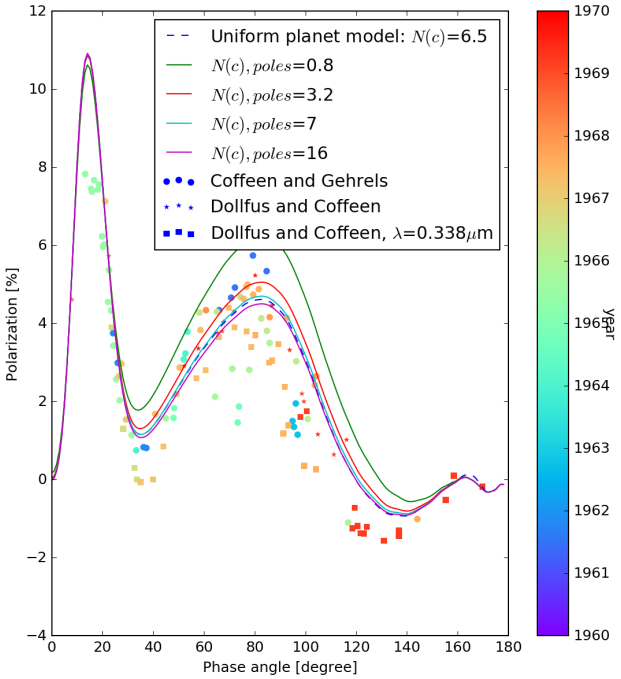

Fig. E.18: Changing the column number density [$particles\ \mu m^{-2}$] of the cloud in the polar regions for $\lambda = 0.340 \mu m$.

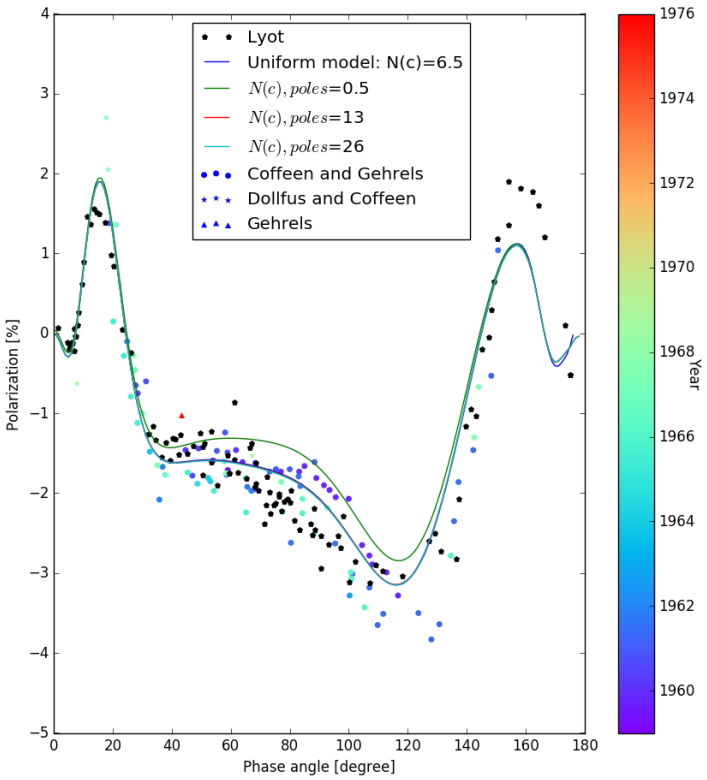

Fig. E.19: Changing the column number density [$particles\ \mu m^{-2}$] of the cloud in the polar regions for $\lambda = 0.550 \mu m$.

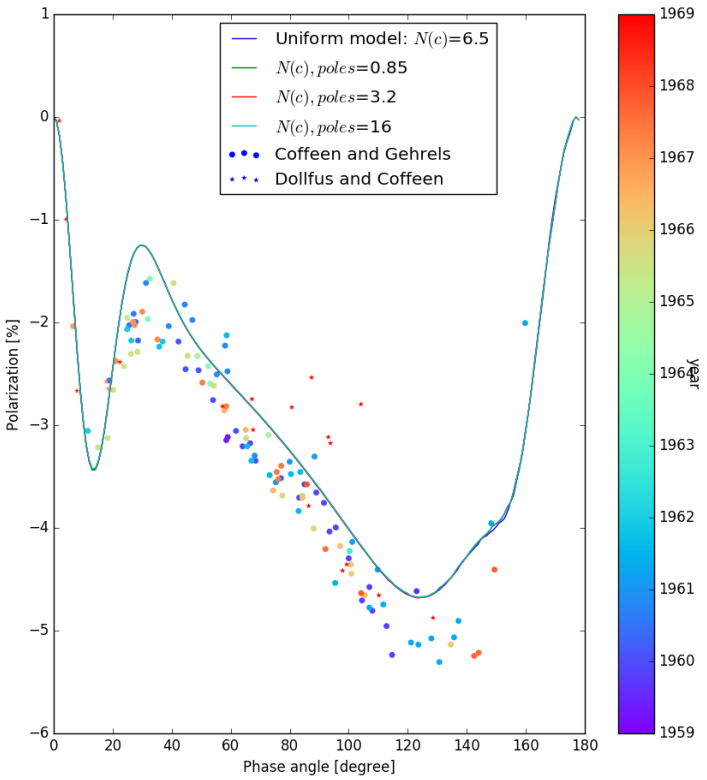

Fig. E.20: Changing the column number density [$particles\ \mu m^{-2}$] of the cloud in the polar regions for $\lambda = 0.990 \mu m$.

Appendix E.6: Effective radius cloud

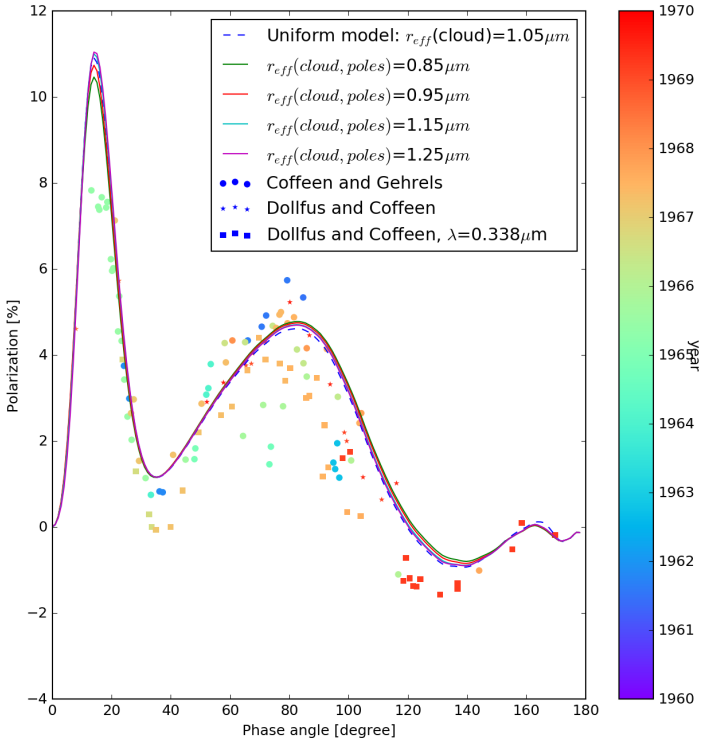

Fig. E.21: Changing the effective radius [μm] of the cloud in the polar regions for $\lambda = 0.340 \mu m$.

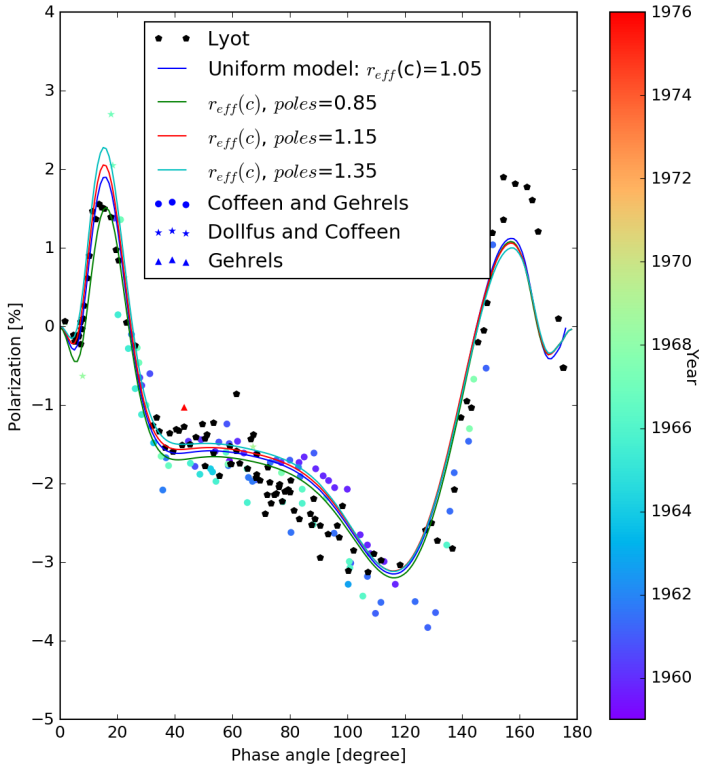

Fig. E.22: Changing the effective radius of the cloud in the polar regions for $\lambda = 0.550 \mu m$.

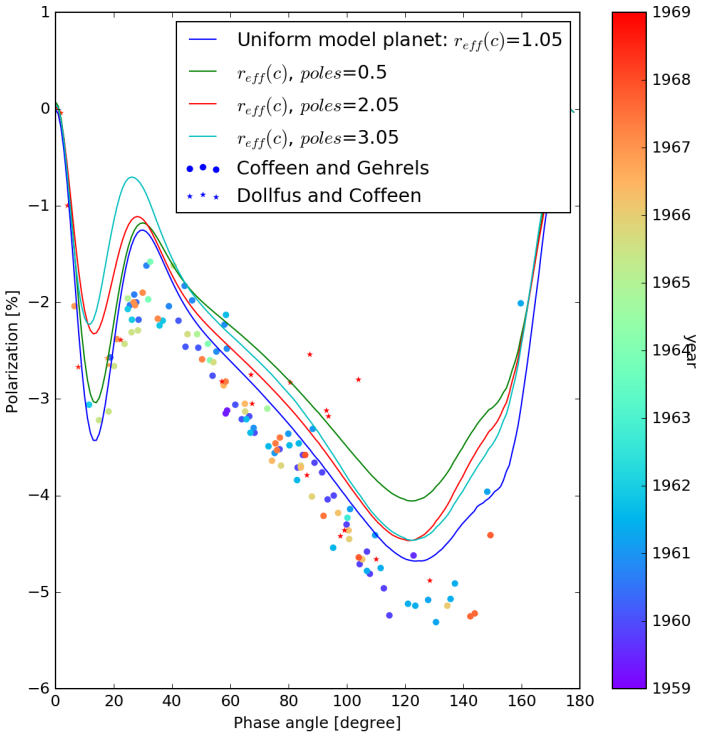

Fig. E.23: Changing the effective radius [μm] of the cloud in the polar regions for $\lambda = 0.990 \mu m$.

Appendix E.7: Cloud top pressure

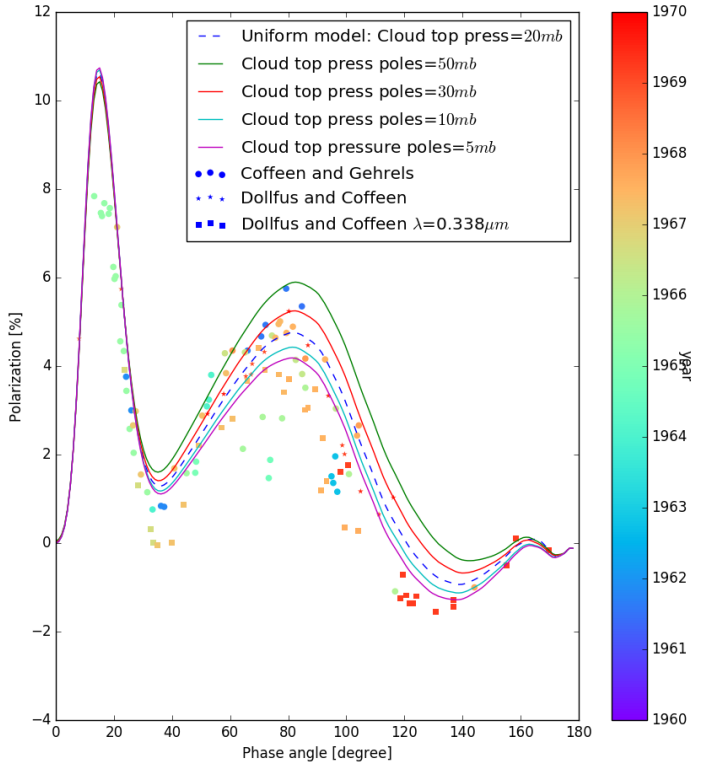

Fig. E.24: Changing the cloud top pressure in the polar regions for $\lambda = 0.340 \mu m$.

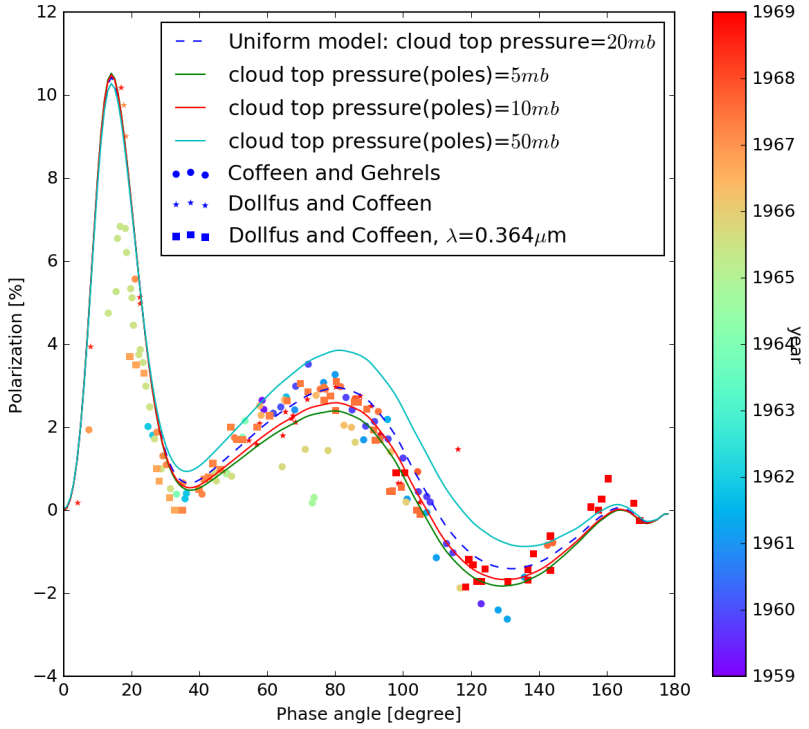

Fig. E.25: Changing the cloud top pressure in the polar regions for $\lambda = 0.365\mu m$.

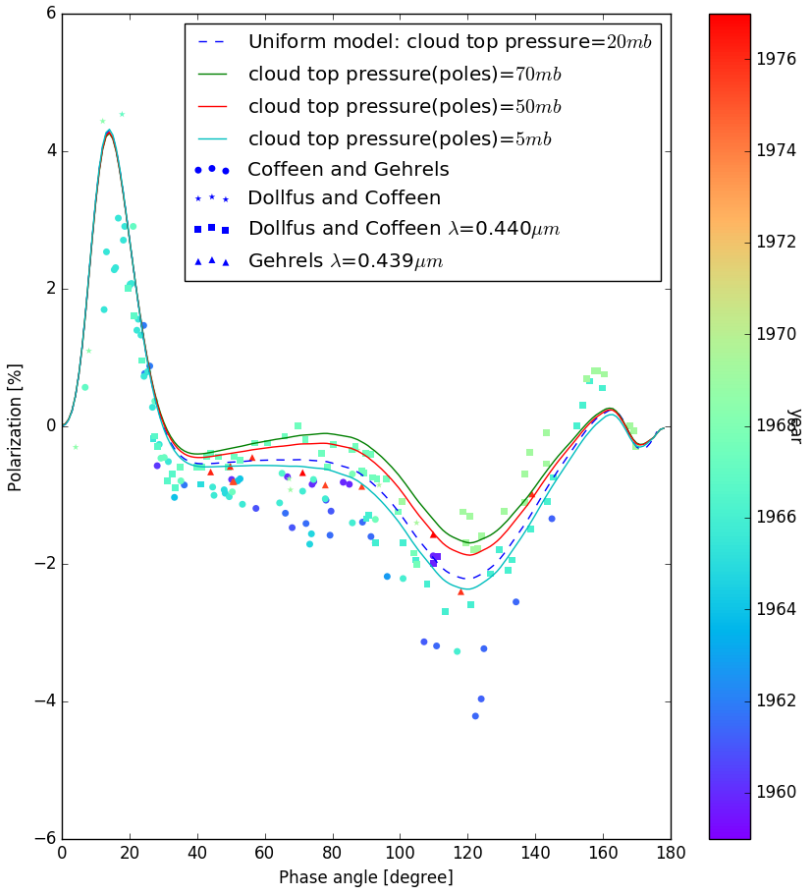

Fig. E.26: Changing the cloud top pressure in the polar regions for $\lambda = 0.445\mu m$.

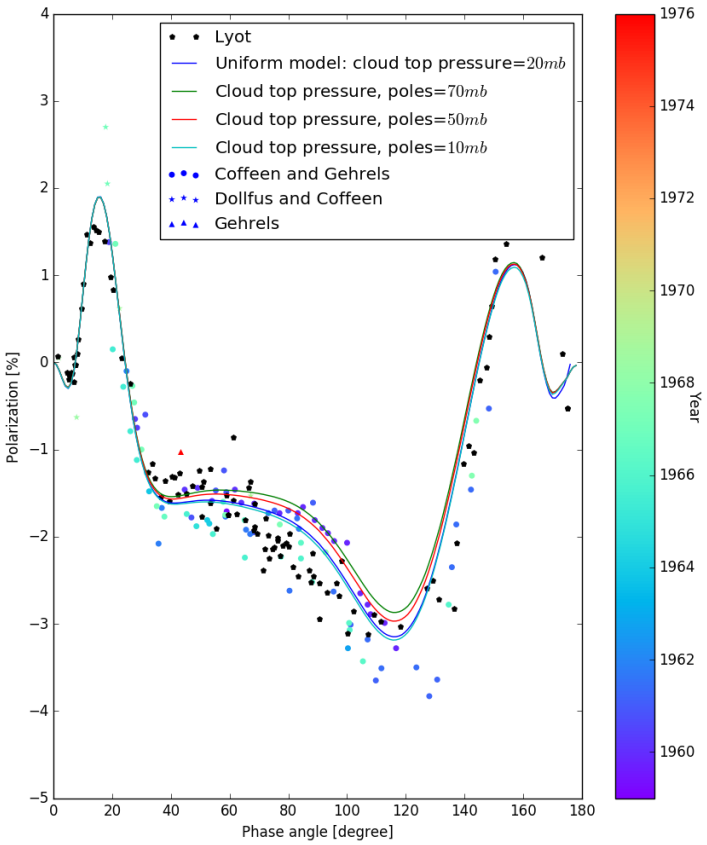

Fig. E.27: Changing the cloud top pressure in the polar regions for $\lambda = 0.550\mu m$.

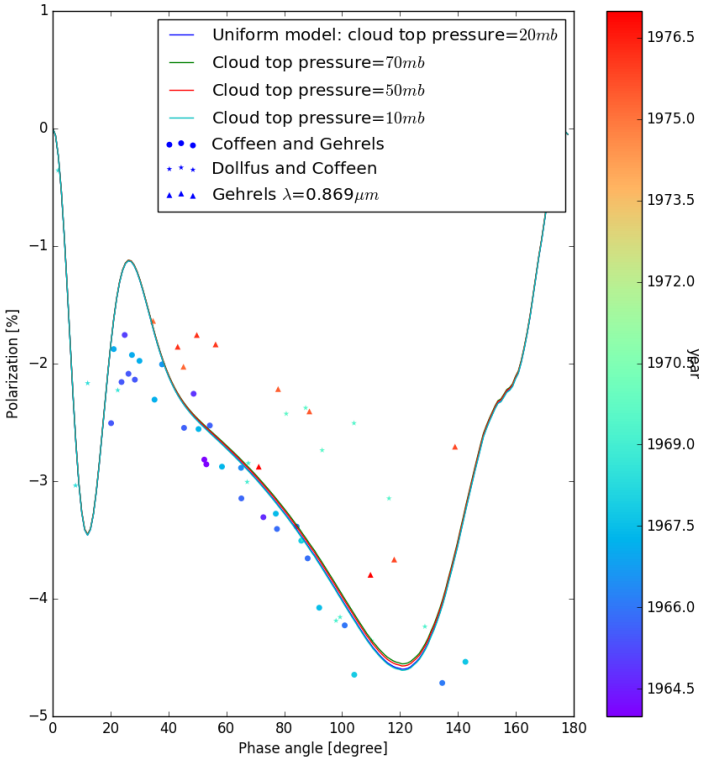

Fig. E.28: Changing the cloud top pressure in the polar regions for $\lambda = 0.875\mu m$.

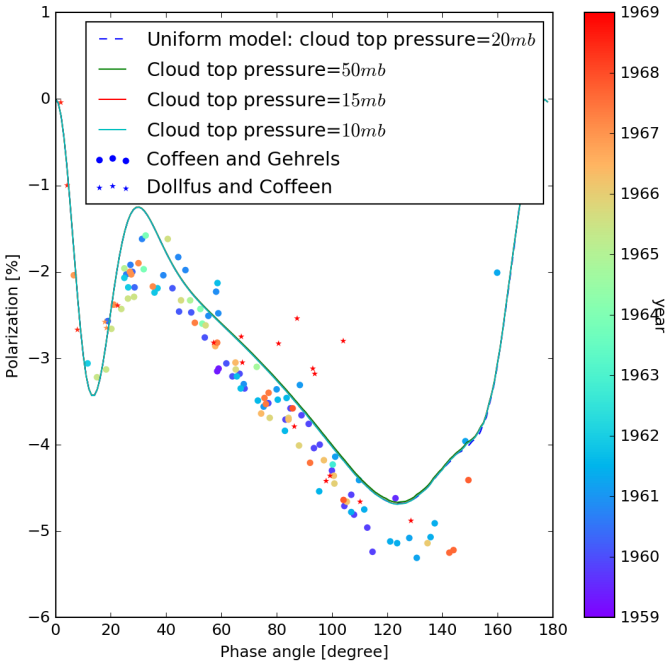

Fig. E.29: Changing the cloud top pressure in the polar regions for $\lambda = 0.990\mu m$.

Appendix E.8: Refractive index cloud

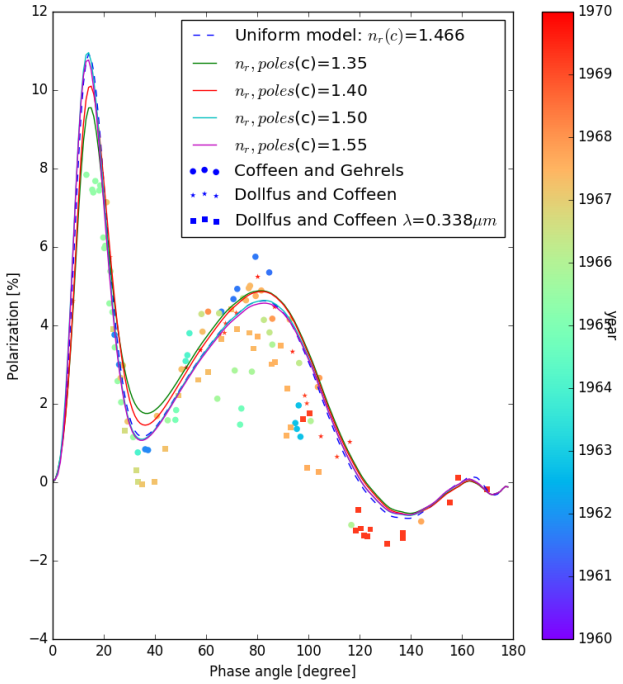

Fig. E.30: Changing refractive index of the cloud particles in the polar regions for $\lambda = 0.340\mu m$.

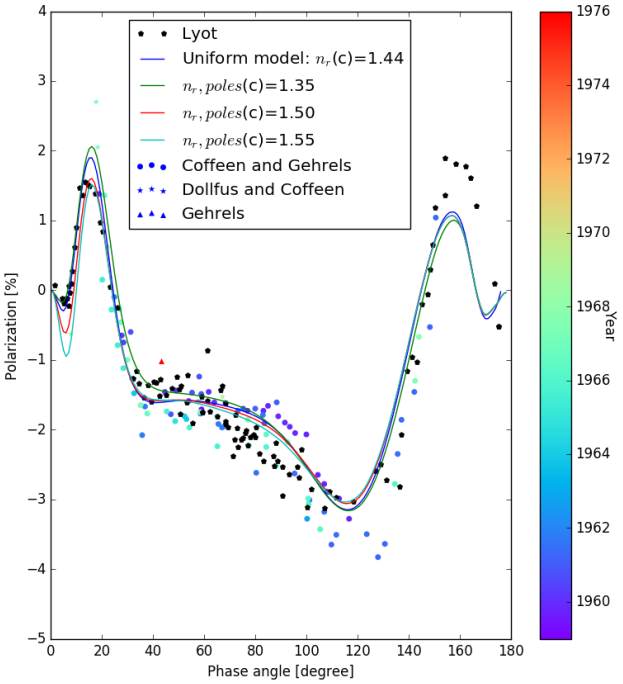

Fig. E.31: Changing refractive index of the cloud particles in the polar regions for $\lambda = 0.550 \mu m$.

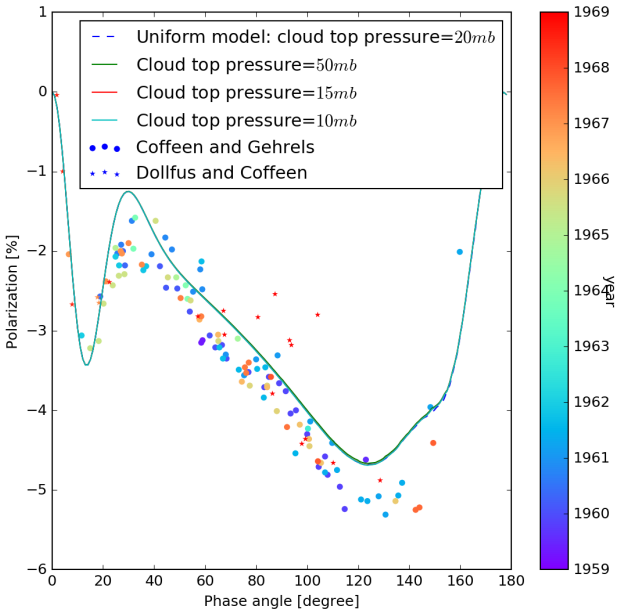

Fig. E.32: Changing refractive index of the cloud particles in the polar regions for $\lambda = 0.990 \mu m$.

Appendix F: Flux VS Polarization

This appendix will show the figures needed to compare the flux with polarization for λ=0.34 μm, λ=0.445 μm, λ=0.65 μm, λ=0.84 μm and λ=0.99 μm.

Appendix F.1: Refractive index of the clouds

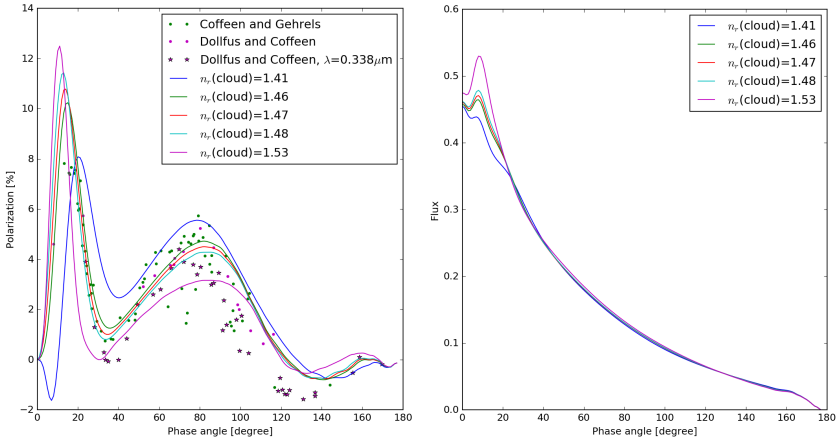

Fig. F.1: Polarization and corresponding flux curve for varying the refractive index of the cloud. *Left:* Polarization curve for λ=0.340μm. *Right:* Flux curve for λ=0.340μm. Input: r_{eff}(cloud)=1.05μm, v_{eff}(cloud)=0.07, r_{eff}(haze)=0.25μm, v_{eff}(haze)=0.18, N(cloud)=6.5 molecule μm^{-2}, N(haze)=0.09 molecule μm^{-2}, n_r(haze)= 1.47 and n_r(cloud)=variable

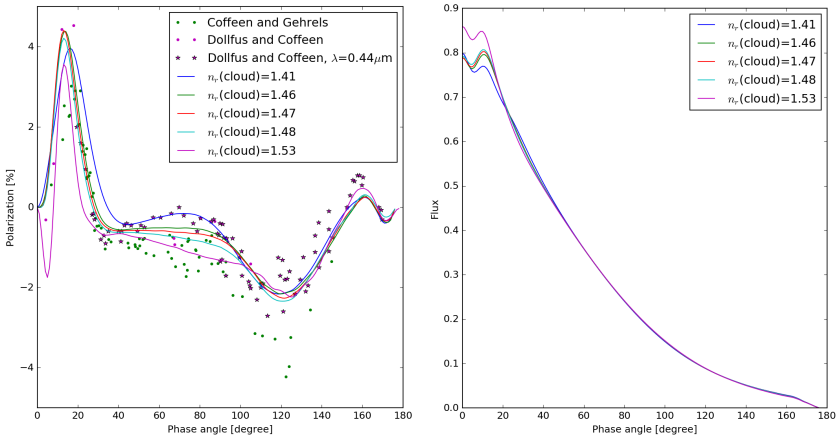

Fig. F.2: Polarization and corresponding flux curve for varying the refractive index of the cloud. *Left:* Polarization curve for λ=0.445μm. *Right:* Flux curve for λ=0.445μm. Input: r_{eff}(cloud)=1.05μm, v_{eff}(cloud)=0.07, r_{eff}(haze)=0.25μm, v_{eff}(haze)=0.18, N(cloud)=6.5 molecule μm^{-2}, N(haze)=0.09 molecule μm^{-2}, n_r(haze)= 1.45 and n_r(cloud)=variable

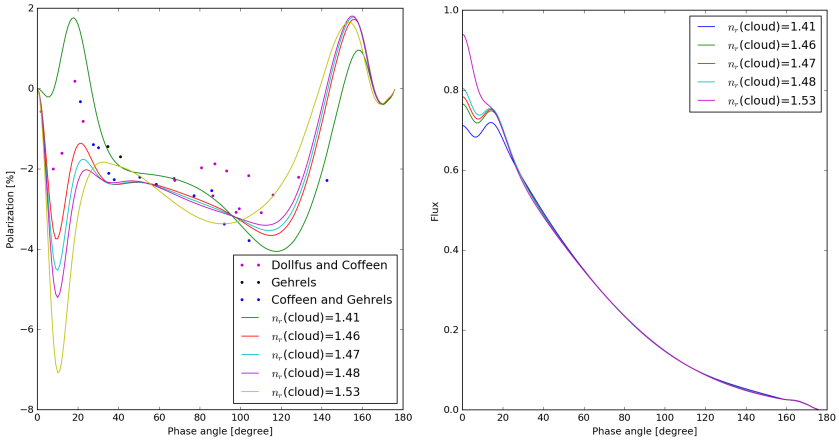

Fig. F.3: Polarization and corresponding flux curve for varying the refractive index of the cloud. *Left:* Polarization curve for λ=0.655μm. *Right:* Flux curve for λ=0.655μm. Input: r_{eff}(cloud)=1.05μm, v_{eff}(cloud)=0.07, r_{eff}(haze)=0.25μm, v_{eff}(haze)=0.18, N(cloud)=6.5 molecule μm^{-2}, N(haze)=0.09 molecule μm^{-2}, n_r(haze)= 1.44 and n_r(cloud)=variable

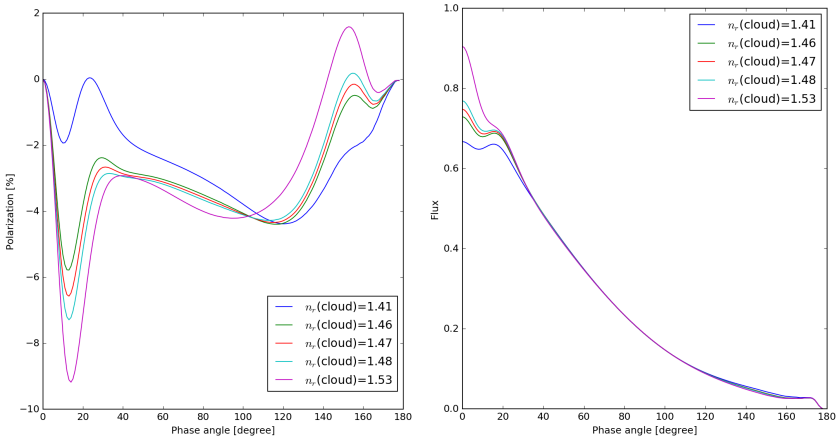

Fig. F.4: Polarization and corresponding flux curve for varying the refractive index of the cloud. *Left:* Polarization curve for λ=0.840μm. *Right:* Flux curve for λ=0.840μm. Input: r_{eff}(cloud)=1.05μm, v_{eff}(cloud)=0.07, r_{eff}(haze)=0.25μm, v_{eff}(haze)=0.18, N(cloud)=6.5 molecule μm^{-2}, N(haze)=0.09 molecule μm^{-2}, n_r(haze)= 1.43 and n_r(cloud)=variable

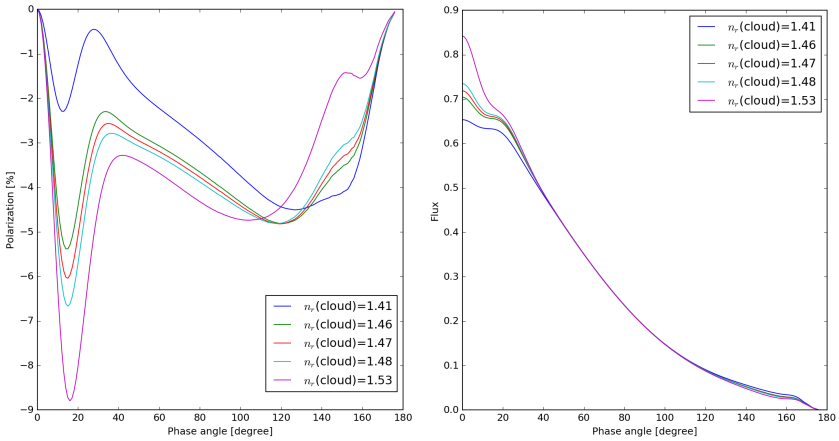

Fig. F.5: Polarization and corresponding flux curve for varying the refractive index of the cloud. *Left:* Polarization curve for λ=0.990μm. *Right:* Flux curve for λ=0.990μm. Input: r_{eff}(cloud)=1.05μm, v_{eff}(cloud)=0.07, r_{eff}(haze)=0.25μm, v_{eff}(haze)=0.18, N(cloud)=6.5 molecule μm^{-2}, N(haze)=0.09 molecule μm^{-2}, n_r(haze)= 1.43 and n_r(cloud)=variable

Appendix F.2: Optical thickness of the clouds

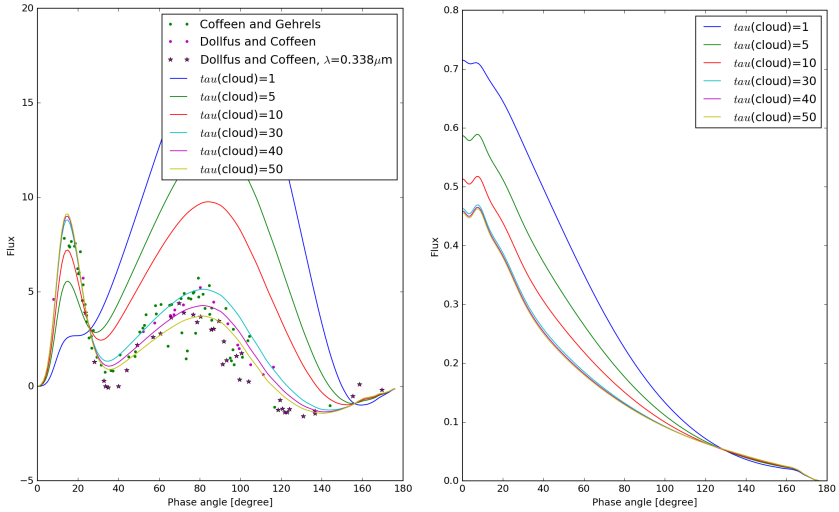

Fig. F.6: Polarization and corresponding flux curve for varying the optical thickness of the cloud. *Left:* Polarization curve for λ=0.340μm. *Right:* Flux curve for λ=0.340μm. Input Figure F.1 with n_r(cloud)=1.47.

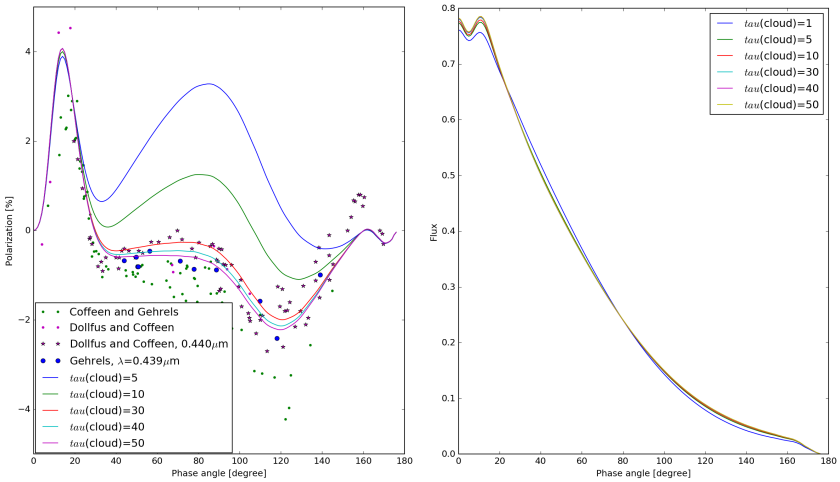

Fig. F.7: Polarization and corresponding flux curve for varying the optical thickness of the cloud. *Left:* Polarization curve for λ=0.445μm. *Right:* Flux curve for λ=0.445μm. Input: Figure F.2 but with n_r(cloud)=1.45.

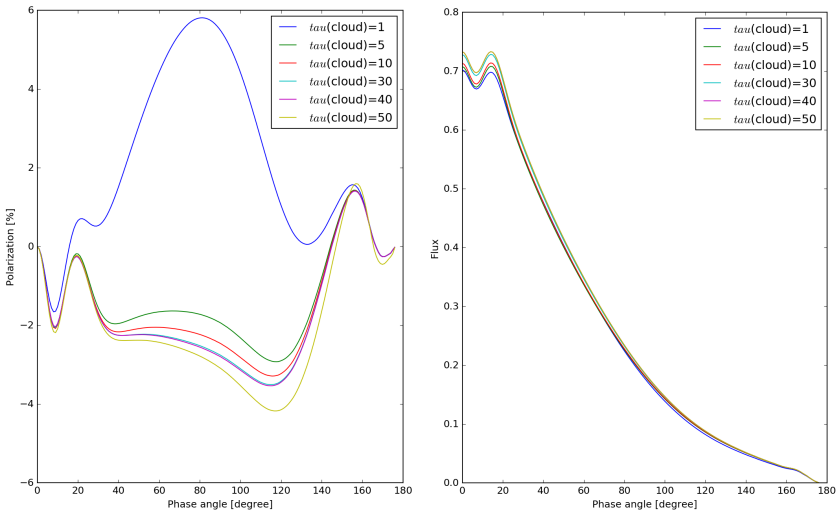

Fig. F.8: Polarization and corresponding flux curve for varying the optical thickness of the cloud. *Left:* Polarization curve for λ=0.655μm. *Right:* Flux curve for λ=0.655μm. Input Figure F.3 but with n_r(cloud)=1.45.

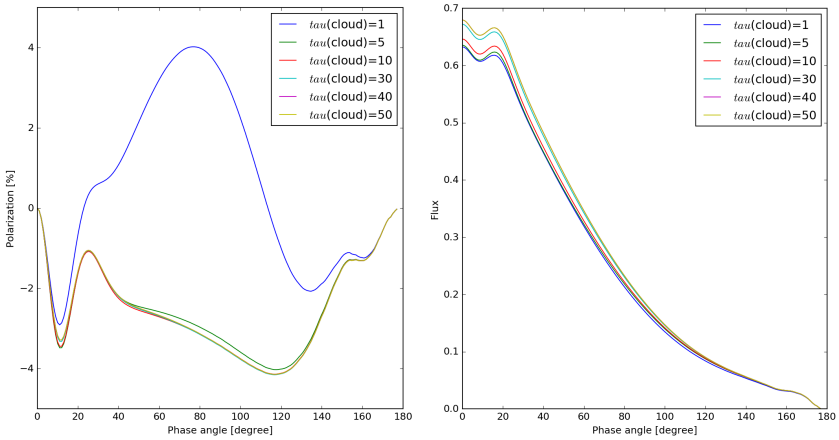

Fig. F.9: Polarization and corresponding flux curve for varying the optical thickness of the cloud. *Left:* Polarization curve for λ=0.840μm. *Right:* Flux curve for λ=0.840μm. Input: Figure F.4 but with n_r(cloud)=1.43

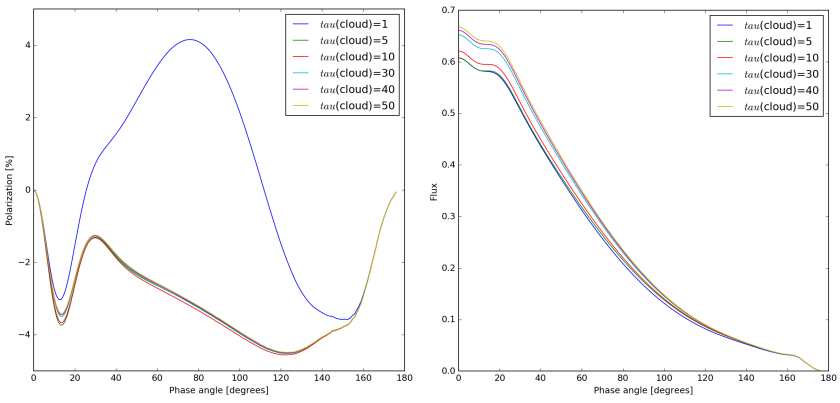

Fig. F.10: Polarization and corresponding flux curve for varying the optical thickness of the cloud. *Left:* Polarization curve for λ=0.990μm. *Right:* Flux curve for λ=0.990μm. Input: Figure F.5 but with n_r(cloud)=1.43.

Appendix F.3: Refractive index of the haze

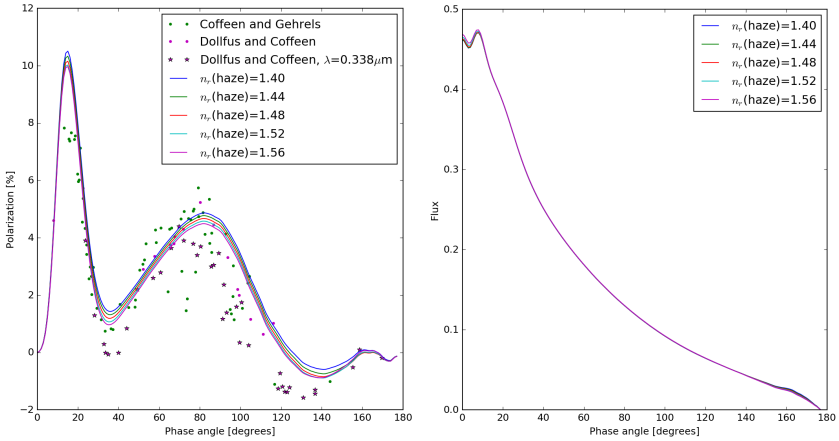

Fig. F.11: Polarization and corresponding flux curve for varying the refractive index of the haze. *Left:* Polarization curve for λ=0.340μm. *Right:* Flux curve for λ=0.340μm. Input: Figure F.1 but with n_r(haze)=variable and n_r(cloud)=1.47.

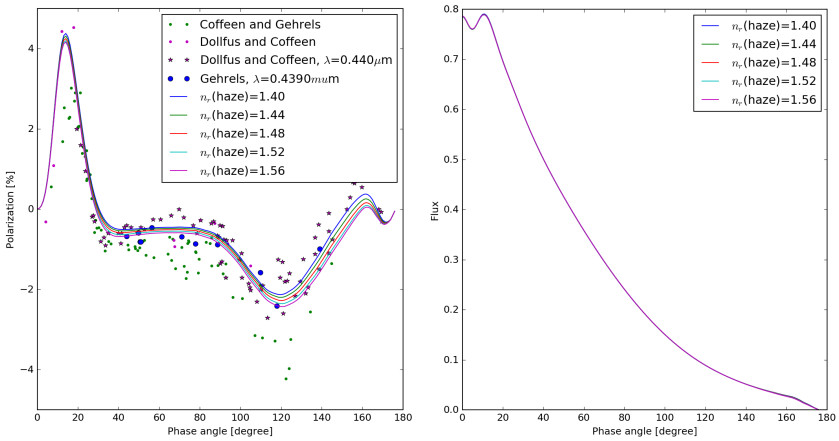

Fig. F.12: Polarization and corresponding flux curve for varying the refractive index of the haze. *Left:* Polarization curve for λ=0.445μm. *Right:* Flux curve for λ=0.445μm. Input: Figure F.2 but with n_r(haze)=variable and n_r(cloud)=1.45.

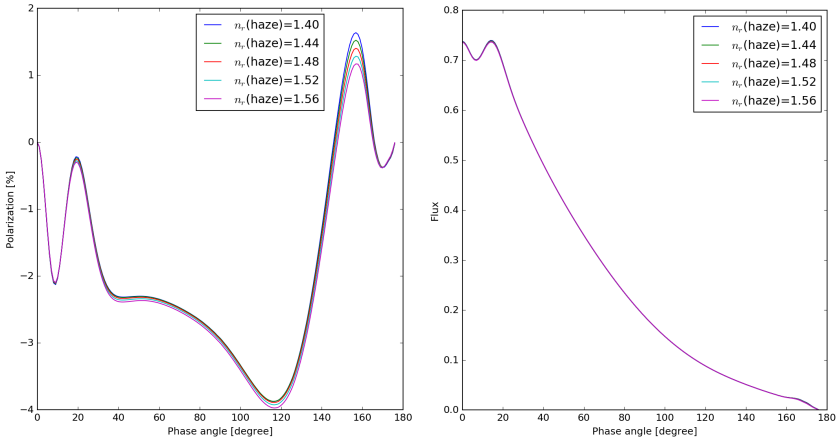

Fig. F.13: Polarization and corresponding flux curve for varying the refractive index of the haze. *Left:* Polarization curve for λ=0.655μm. *Right:* Flux curve for λ=0.655μm. Input: Figure F.3 but with n_r(haze)=variable and n_r(cloud)=1.45.

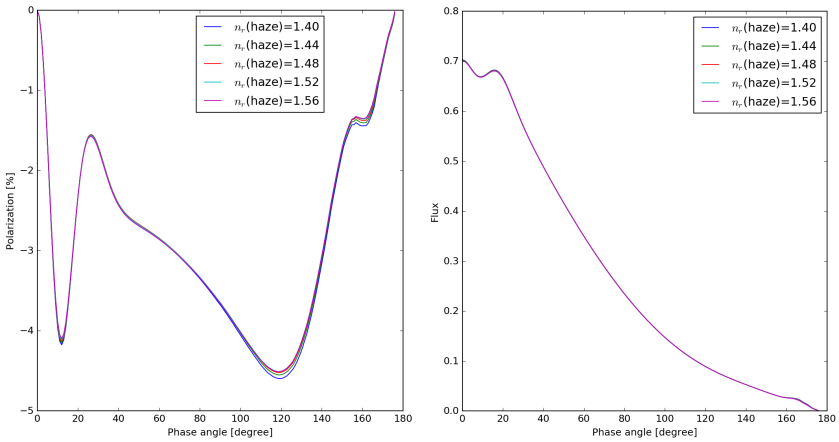

Fig. F.14: Polarization and corresponding flux curve for varying the refractive index of the haze. *Left:* Polarization curve for λ=0.840μm. *Right:* Flux curve for λ=0.840μm. Input: Figure F.4 but with n_r(haze)=variable and n_r(cloud)=1.43.

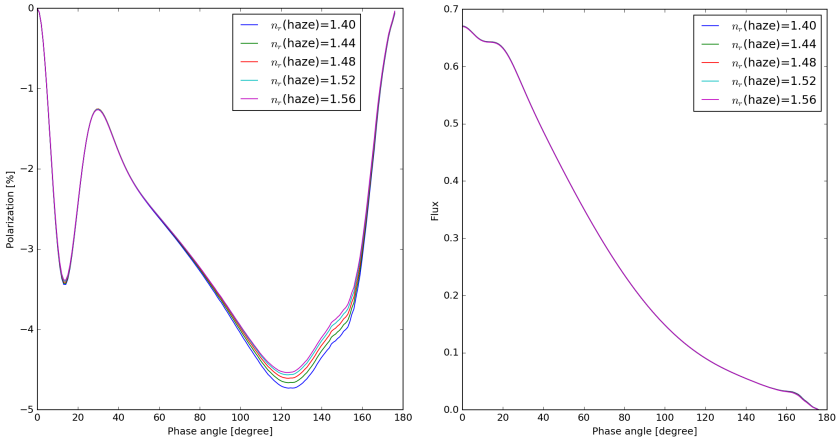

Fig. F.15: Polarization and corresponding flux curve for varying the refractive index of the haze. *Left:* Polarization curve for λ=0.990μm. *Right:* Flux curve for λ=0.990μm. Input: Figure F.5 but with n_r(haze)=variable and n_r(cloud)=1.43.

Appendix F.4: Optical thickness of the haze

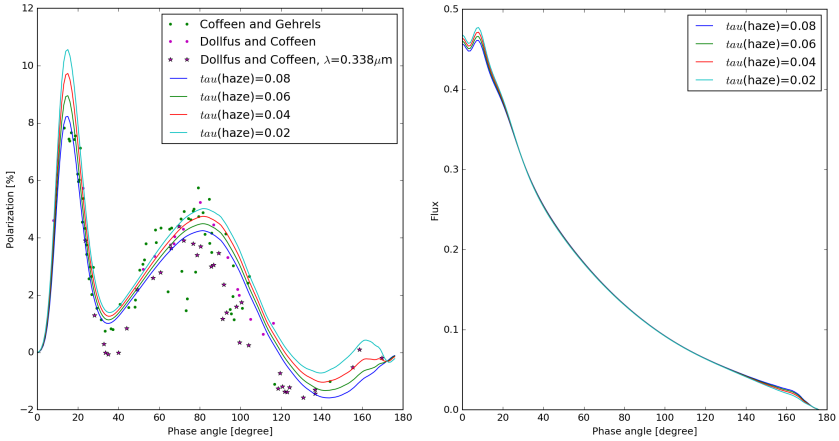

Fig. F.16: Polarization and corresponding flux curve for varying the optical thickness of the haze. *Left:* Polarization curve for λ=0.340μm. *Right:* Flux curve for λ=0.340μm. Input: Figure F.1 but with n_r(cloud)=0.47.

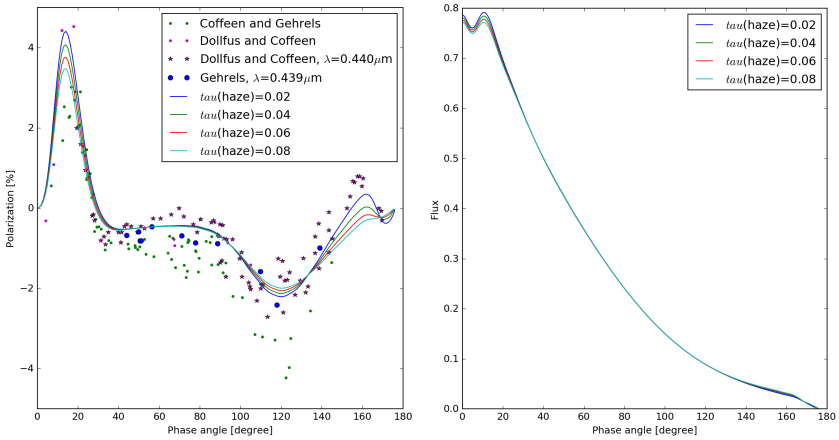

Fig. F.17: Polarization and corresponding flux curve for varying the optical thickness of the haze. *Left:* Polarization curve for λ=0.445μm. *Right:* Flux curve for λ=0.445μm. Input: Figure F.2 but with n_r(cloud)=1.45.

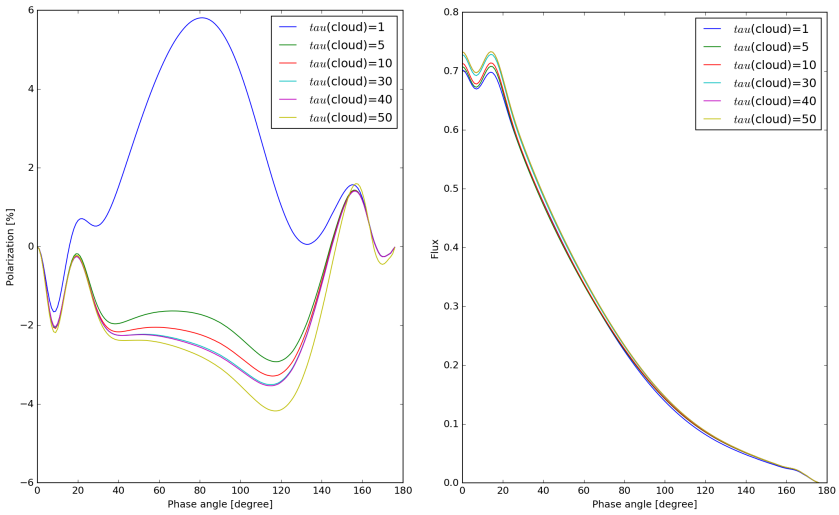

Fig. F.18: Polarization and corresponding flux curve for varying the optical thickness of the haze. *Left:* Polarization curve for λ=0.655μm. *Right:* Flux curve for λ=0.655μm. Input: Figure F.3 but with n_r(cloud)=1.45.

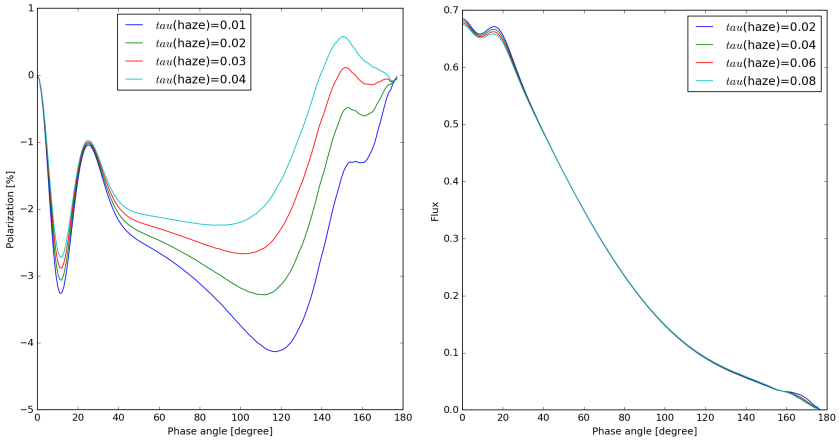

Fig. F.19: Polarization and corresponding flux curve for varying the optical thickness of the haze. *Left:* Polarization curve for λ=0.840μm. *Right:* Flux curve for λ=0.840μm. Input: Figure F.4 but with n_r(cloud)=1.43.

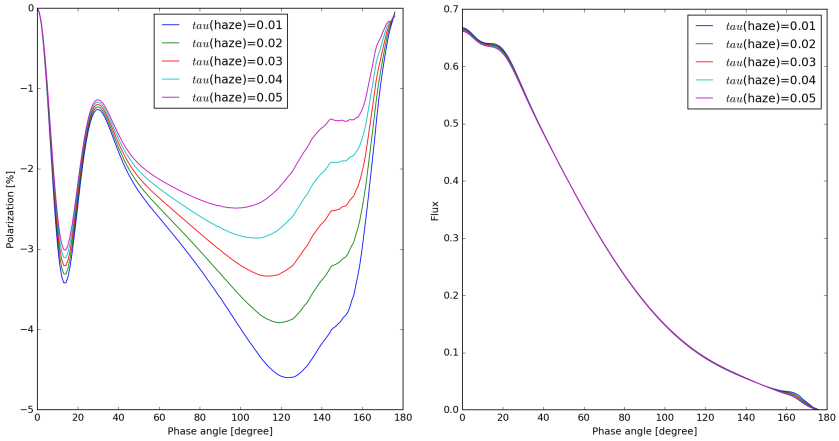

Fig. F.20: Polarization and corresponding flux curve for varying the optical thickness of the haze. *Left:* Polarization curve for λ=0.990μm. *Right:* Flux curve for λ=0.990μm. Input: Figure F.5 but with n_r(cloud)=1.43.

Appendix G: 100 % CO_2 gas compared with 96.5% CO_2 and 3.5% N_2 gas

It is known that the gas in the Venus atmosphere consists of 96.5% CO_2 and 3.5% N_2. For this paper pure CO_2 gas was assumed. In this appendix we will look at the justification of this assumption.
If the composition of the gas is changed, the following things will change: the refractive index of the gas, the depolarisation factor of the gas and the molecular mass of the gas particles.
Let's start with the refractive index, n_r, of the CO_2-gas. This formula is obtained from (Haberle et al. 2017).

$$n_r(CO_2) = 1 + 1.1427 * 10^3 * (\frac{5799.25}{16.6 * 10^9 - S^2} + \frac{120}{7.96 * 10^9 - S^2} + \frac{5.33}{5.63 * 10^9 - S^2} + \frac{4.32}{4.6 * 10^9 - S^2} + \frac{0.1218145 * 10^{-4}}{5.85 * 10^6 - S^2}) \quad \text{(G.1)}$$

with

$$S = \frac{1}{\lambda} \quad \text{(G.2)}$$

and λ in $[cm]$. Bates (1984) investigated the refractive index of air and therefore needed the refractive index of N_2. For $\lambda > 0.468 \mu m$:

$$n_r(N_2) = 1 + 6.8552 * 10^{-5} + \frac{3243157}{144 * 10^8 - S^2} \quad \text{(G.3)}$$

and for $0.254 < \lambda < 0.468 \mu m$:

$$n_r(N_2) = 1 + 5.989242 * 10^{-5} + \frac{3363266.3}{144 * 10^8 - S^2} \quad \text{(G.4)}$$

with S equal to S in Equation G.2. In the paper by Bates (1984) he composes the refractive index of air by summing up the weighted refractive indices of the substances of air. Based on this, we use:

$$n_r(CO_2 \& N_2) = 0.965 * n_r(CO_2) + 0.035 * n_r(N_2) \quad \text{(G.5)}$$

resulting in an updated value for the refractive index that is dependent on wavelength.
The depolarization factor is not dependent on wavelength and can for CO_2 and N_2 be found in Hansen & Travis (1974). For the depolarization factor it is assumed that the combined depolarisation factor can be determined by applying:

$$dpol_{combined} = 0.965 * dpol_{CO_2} + 0.035 * dpol_{N_2} \quad \text{(G.6)}$$

which results in Table G.1
For the combined molecular mass of the gas particles, the same principle is applied:

$$mma_{combined} = 0.965 * mma_{CO_2} + 0.035 * mma_{N_2} \quad \text{(G.7)}$$

$dpol_{CO_2}$	0.09
$dpol_{N_2}$	0.03
$dpol_{combined}$	0.0879

Table G.1: Depolarization factors

resulting in:

mma_{CO_2}	44
mma_{N_2}	28
$mma_{combined}$	43.44

Table G.2: Molecular mass of the gas particles

When this is updated in the PyMieDAP code, it can be seen that the effect of adding 3.5% of N_2 to the gas is negligible. Figure G.1 supports this.

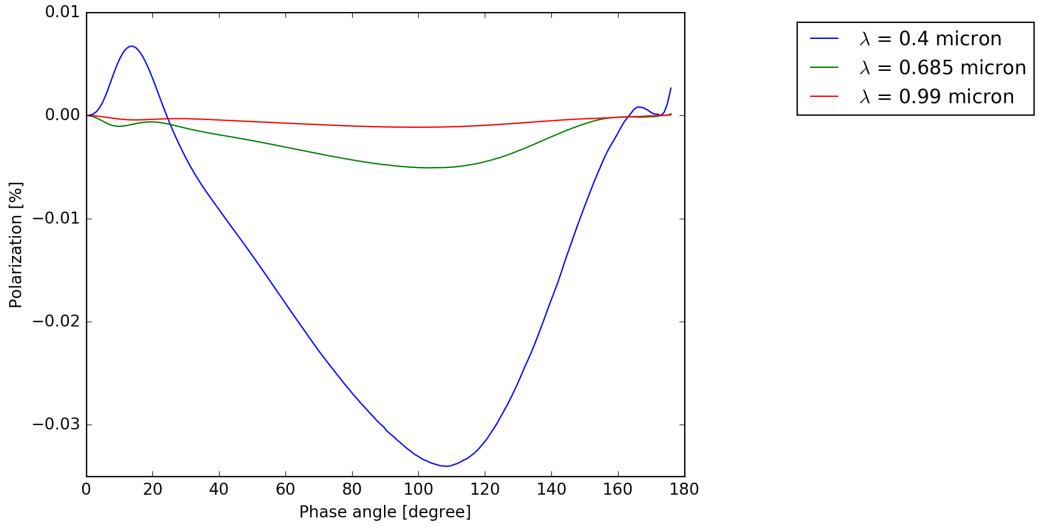

Fig. G.1: Difference in polarization between a model with CO_2 gas and a model with CO_2 and N_2 gas for different wavelengths.

During this investigation, the model is kept equal to the model described in the paper with a gas layer, cloud layer, haze layer and top gas layer. In Figure G.1 all models are exactly the same.

3

Conclusions

This chapter will shortly answer the research questions that were put forward in Chapter 1 of this report.

3.1. Historical data

What polarization measurements of Venus were done in the past and what can we learn from them?

For this research, historical data obtained by different observers was used. All observations combined cover the following years: 1922-1924, 1950, 1953, 1959-1969 and 1975-1979.

The first observations that we have used were obtained by Lyot [5] from May 1922 till July 1924. He noted that the average plane of polarization of Venus was either parallel or perpendicular to the plane of scattering. Lyot also found that the sign of the Venus polarization changed four times over the whole phase angle range, unlike the polarization of the Moon, Mercury and Mars.

Almost 40 years later Coffeen and Gehrels measured the linear polarization of sunlight reflected by Venus. Their observations were done between April 1959 and January 1968. From the observations, Coffeen and Gehrels [1] concluded that the position angle of the disk polarization is either perpendicular or parallel to the plane of scattering. Since repeatability was observed over their almost 10 years observational period, Coffeen and Gehrels [1] concluded that the light scattering mechanism on Venus must be rather stable. The polarization wavelength dependence was found to be generally monotonic: the positive polarization increases with decreasing wavelength. At the longer wavelengths, the negative polarization is dominant. This is impossible for molecular scattering but it is characteristic for scattering by transparent particles [1]. The fact that the polarization position angle was either parallel or perpendicular to the plane of scattering could be explained only with the assumptions that no particle alignment mechanisms exist in the atmosphere of Venus, and that brightness and polarization are symmetric about the illumination equator [1]. Which means that the spherical planet introduces no preferential direction, leaving only the incident and emergent rays to define the direction of polarization (this assumes unpolarized incident radiation) [1].

In the same period as Coffeen and Gehrels, Dollfus and Coffeen [2] also published a paper regarding polarization observations of Venus. The paper by Dollfus and Coffeen [2] compares two kinds of measurements: measurements made in France by Dollfus, Focas and Marin and measurements made in the US by Coffeen, Gehrels and Veverka. The US observations are the ones presented in [1], but the 1970 paper adds some new measurements from 1967 to January 1970. Dollfus and Coffeen [2] found that the agreement between the independent measurements is generally better than ±0.3% absolute polarization. Combining these observations, a period from September 1950 till January 1970 is covered in the wavelength region of $\lambda = 0.338 \mu m$ to $\lambda = 0.990 \mu m$. The observations cover the phase angle range from 1.5°to 176.5°.

Interestingly, the polarization of the Venus disk was very low from late 1964 through 1965 in the ultraviolet spectral range. No evidence was found for a systematic error, the basic instrumentation did not change during the observations. So the conclusion is that the global ultraviolet polarization was generally depressed for approximately 18 months [2].
The last observations that are used were presented in the paper by Gehrels et al. [3]. The observations were done between 1975 and 1977.

3.2. Time variability

What can we say about the long term variations in the data by combining the data?
Unfortunately, it is very hard to say something about the long term variations of the data. The historical data is not suitable for a detailed time variability analysis. This is due to the fact that the data is not nicely spread over time, the date of λ=0.340μm illustrates this: In 1965, Coffeen and Gehrels mainly observed at small phase angles, while the middle phase angle range was observed by Dollfus and Coffeen in 1968 and the range with larger phase angles in 1970. For a precise time variations analysis you would need observations of all phase angles in all periods. But, for the Venus case, it can be roughly stated that:

- the polarization was higher in 1975/1967 than it was in 1965/1968;
- the polarization was also higher in 1968/1970 than it was in 1965/1968 but not higher than it was in 1967;
- there was a decrease in the polarization of the ultraviolet region in the years 1964/1965.

3.3. Horizontal inhomogeneity

Is it possible to recognize the horizontal inhomogeneity in the historical ground based data?
This research questions is answered in two parts, first we looked at the horizontal inhomogeneity in general, so numerically investigating whether a variation in the polar region would be observable. And second, applying it to the Venus case to see if we expect other cloud or haze properties around the Venus poles.
We found with the help of the numerical simulations that it is possible to observe different optical thicknesses for the haze around the poles using disk-integrated data, especially when looking at the near-infrared wavelength region. Further, it is also possible to observe changes in:

- the effective radius of the cloud and haze particles;
- the refractive index of the cloud particles;
- the cloud top pressure;
- and in the optical thickness of the clouds.

It is not possible to observe changes in the refractive index of the haze particles at the poles. But one should note that the optical thickness of the clouds can only be distinguished using the UV-wavelengths.
For the application to Venus it was found that adding larger particles to the haze layer and decreasing the cloud top pressure, both improved the fit to the historical data. These two actually go hand in hand. Extending the cloud layer (decreasing the cloud top pressure) means more larger particles in higher altitudes which corresponds to adding larger particles to the haze layer. So it is likely that there exist more larger particles at higher altitudes at the Venus poles. If there are changes in any of the other cloud or haze properties, those can not be observed using the available historical Venus disk-integrated polarization data.

3.4. Exoplanets

How can we apply the outcomes to exoplanet research?

It is interesting to apply the outcomes of this research based on Venus to exoplanets since Venus can be observed in a wide range of phase angles, such as exoplanets, and the observations are disk-integrated. For exoplanets it will, definitely in the beginning, only be possible to do disk integrated observations. Thereby, polarization measurements are interesting for exoplanets because of their independence of planet radius, stellar flux and distance to the observed planet since those properties are likely to be unknown.

During the analysis of the historical data, we ran into some problems. These are problems that can occur during exoplanet research as well, therefore the solutions to these problems can be relevant to apply to exoplanet research. The main issues was:

- For analysing the time variability we experienced some issues, see section 3.2.

This issue can be solved by observing consequently and keeping in mind the orbit of the exoplanet.

The next thing we can learn from the Venus research is summarized in Table 3.1. We saw that not all planet properties related to clouds and hazes were visible in every wavelength or phase angle. The most important wavelength and phase angle ranges are listed in Table 3.1 together with the corresponding cloud or haze property. It should of course be kept in mind that this applies for Venus like planets and can be different when the atmospheric properties deviate too much from the researched values.

	Wavelength [μm]	Phase angle [°]
$n_r(cloud)$	All	All
τ_{cloud}	0.34 - 0.685	30 - 160
$n_r(haze)$	Mainly 0.34 - 0.650	40 and higher
τ_{haze}	All	All

Table 3.1: Most interesting wavelength and phase angles ranges to observe in.

Comparison to flux observations

When obtaining the flux curves for (exo)planets it is possible to find the optical thickness of the cloud and, if you are able to measure the small phase angles, the refractive index of the cloud assuming the geometric albedo is known. But finding the haze properties (or identifying a haze layer) will be very challenging. For polarization curves it is possible to obtain information on both cloud and hazes, if you are able to observe accurately.

A

Verification

The PyMieDAP software that was used for this research has already been validated, see [9]. First, to make sure that PyMieDAP is used in a correct way, the PyMieDAP benchmark files [1] were followed and the results were successfully reproduced. Then, in order to make sure PyMieDAP is used in a correct way, the basic figures of [4] are reproduced. This reproduction is shown in Figure A.1 . Here a basic model with only the cloud layer is assumed.

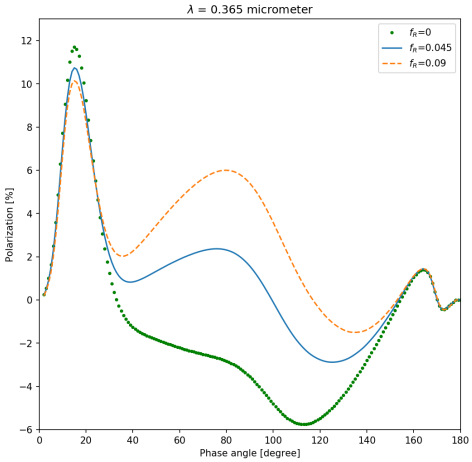

(a) Reproduction of Figure 9 from Hansen and Hovenier [4].

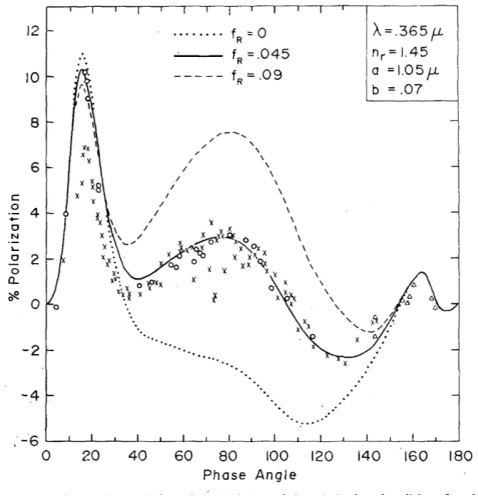

(b) Figure 9 of Hansen and Hovenier [4]. a is the refractive index of the particles and b the effective variance.

Figure A.1: f_R is the fraction of the cloud optical thickness so that the molecular scattering optical thickness equals the fraction times the total optical thickness.

[1] The benchmark files can be found here: https://gitlab.com/loic.cg.rossi/pymiedap/-/tree/master.

Bibliography

[1] D. L. Coffeen and T. Gehrels. Wavelength Dependence of Polarization. XV. Observations of Venus. *The Astronomical Journal*, 74(3):433, April 1969.

[2] A. Dollfus and D. L. Coffeen. Polarization of Venus I Disk Observations. *Astronomy & Astrophysics*, 8:251, October 1970.

[3] T. Gehrels, J. C. Gradie, M. L. Howes, and F. J. Vrba. Wavelength dependence of polarization. XXXIV - Observations of Venus. *The Astronomical Journal*, 84:671–682, May 1979. doi: 10.1086/112467.

[4] J. E. Hansen and J. W. Hovenier. Interpretation of the polarization of venus. In C. F. Bohren, editor, *Selected Papers on Scattering in the Atmosphere*, pages 288–311. SPIE optical engineering press, 1974.

[5] B. Lyot. Research on the polarization of light from planets and from some terrestrial substances, Translation. *Annales de 1'Observatoire de Paris*, 1929.

[6] NASA. Venus, 2018. `https://solarsystem.nasa.gov/planets/venus/in-depth/`.

[7] NASA. Luvoir design, 2019. `https://asd.gsfc.nasa.gov/luvoir/design/`.

[8] M. Pätzold, B. Häusler, M. K. Bird, S. Tellmann, R. Mattei, S. W. Asmar, V. Dehant, W. Eidel, T. Imamura, R. A. Simpson, and G. L. Tyler. The structure of Venus' middle atmosphere and ionosphere. *Nature*, 450:657–660, November 2007. doi: 10.1038/nature06239.

[9] L. Rossi, J. Berzosa-Molina, and D. M. Stam. PYMIEDAP: a Python-Fortran tool for computing fluxes and polarization signals of (exo)planets. *Astronomy & Astrophysics*, 616:A147, September 2018. doi: 10.1051/0004-6361/201832859.

[10] Sky & Telescope. The clouds of venus puzzle scientists, 2019. `https://skyandtelescope.org/astronomy-news/venus-clouds-puzzle-scientists/`.

[11] S.J. Wiktorowicz and D.M. Stam. Exoplanets. In Ludmilla Kolokolova, James Hough, and Anny-Chantal Levasseur-Regourd, editors, *Polarimetry of stars and planetary systems*, pages 439 – 457. Cambridge university press, 2015.